Mechanotransduction of Interstitial Fluid Stresses and Effects on Tumor Cell Migration

By

William J. Polacheck

B.S. Biological Engineering (2008), Cornell University
S.M. Mechanical Engineering (2010), M.I.T.

Submitted to the Department of Mechanical Engineering in partial
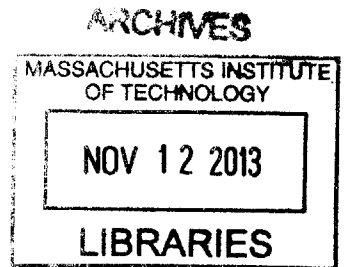fulfillment of the requirements of the degree of

Doctor of Philosophy in Mechanical Engineering

at the

MASSACHUSETTS INSTITTUE OF TECHNOLOGY

September 2013

Author..
Department of Mechanical Engineering
(Date) 9/9/2013

Certified by...
Roger D. Kamm
Professor of Mechanical Engineering
Professor of Biological Engineering
Thesis Supervisor

Accepted by...
David E. Hardt
Professor of Mechanical Engineering
Graduate Officer

Mechanotransduction of Interstitial Fluid Stresses and Effects on Tumor Cell Migration

By

William J. Polacheck

Abstract

Breast cancer incidence in the United States is 1 in 8, and over 90% of breast cancer related deaths are due to metastases, secondary tumors at a site distant from the primary tumor. Metastasis formation requires carcinoma cells to navigate through the tumor microenvironment and invade the surrounding stroma. Migration is a highly orchestrated process in which cells are guided by both internal signals and signals from the microenvironment. Hence, understanding the mechanisms that guide cell migration in response to various stimuli in the tumor and stromal microenvironments is key to developing therapies that prevent tumor cell migration and render cancer more treatable.

Osmotic and hydrostatic pressure gradients within the extracellular matrix (ECM) drive flow of interstitial fluid through the ECM. Elevated osmotic pressure, lymphatic collapse, solid stress, and increased microvascular permeability contribute to elevated interstitial fluid pressure (IFP) during carcinoma progression, and high intratumoral IFP leads to pressure gradients at the tumor margin, which drive fluid flow that emanates from the tumor core to drain in the surrounding stroma.

In this thesis, we explore the effect of interstitial flow (IF) on tumor cell migration. We developed a microfluidic platform to apply repeatable, robust IF through tissue constructs consisting of human metastatic breast cancer cells embedded within a 3D collagen type I matrix. We implemented the microfluidic device to validate CCR7-mediated autologous chemotaxis as a mechanism that guides downstream migration in response to IF. However, we identified a separate competing pathway that drives cell migration upstream (rheotaxis). Rheotaxis results from asymmetry in matrix adhesion stress that is required to balance fluid drag imparted by IF on tumor cells. Thus, autologous chemotaxis, mediated by chemical transport, and rheotaxis, mediated by fluid stresses, compete to direct cell migration downstream or upstream in response to IF. Our results provide insight into mechanotransduction in 3D porous media and into the mechanisms by which asymmetries in matrix adhesion tension guide cell migration. Furthermore, our results demonstrate that the consideration of IF is crucial for understanding and treating metastatic disease.

Key words: Interstitial flow, mechanotransduction, tumor cell migration, microfluidics

Acknowledgements

Table of Contents

List of figures

List of tables

Chapter 1: Introduction and background

1.1 Tumor microenvironment in the metastatic cascade

Invasive breast cancer incidence in the United States is approximately 1 in 8, and 39,520 women were expected to die from breast cancer in 2011 (breastcancer.org). Although detection and treatment of primary breast carcinoma has improved greatly, effective treatment for metastatic disease remains elusive, and over 90% of breast cancer related deaths are due to metastases, secondary tumors at a site distant from the primary tumor (1). In the formation of metastases, tumor cells abandon the native epithelial phenotype and migrate from the primary tumor to local vasculature as single cells or as a collective invasive front (2). Cells then enter the blood or lymphatic vasculature through a process known as intravasation, and systemic circulation carries cells to tissue distant from the primary tumor (3), where a subset of these circulating tumor cells extravasate and colonize a secondary tumor (Figure 1) (4). Although much recent work has focused on characterizing the genetic and molecular expression of genes and proteins specific to metastatic cells for diagnosis and treatment, little is known about the mechanics and dynamics of tumor cell dissemination and homing to blood or lymphatic vessels.
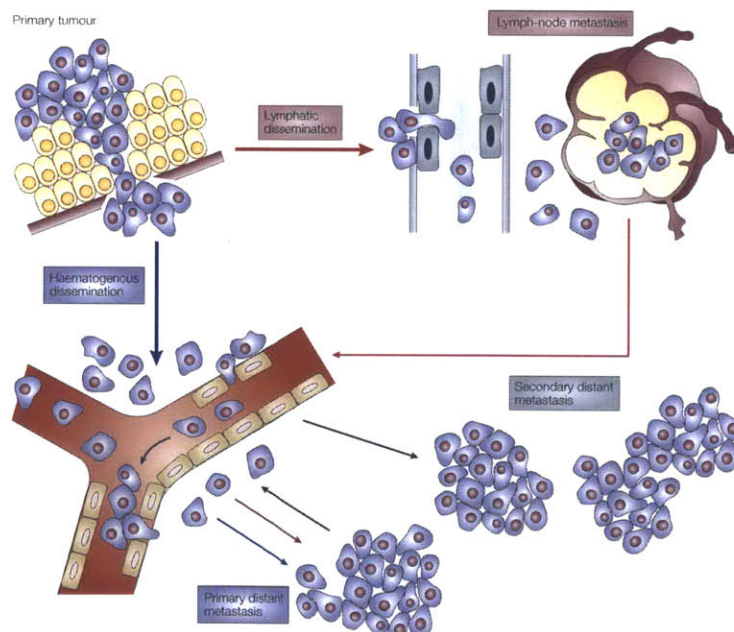
Figure 1. Overview of metastatic cascade. Tumor cells acquire a metastatic, migratory phenotype then migrate across the basement membrane into the surrounding stromal tissue toward blood or lymphatic vasculature. Once cells intravasate and enter the vasculature, they are carried to sites distant from the primary tumor, and upon arrest and extravasation, metastatic cells invade the distant tissue and colonize metastatic lesions (modified from (5)).

Metastasis formation is a complex, multistage process involving modulation of cell phenotype, cell migration, and dynamic homeotypic and heterotypic cell-cell interactions (1). There are various proposed models for carcinoma progression and the formation of metastases (reviewed by Weigelt *et al.* (6)), and tumors likely employ more than one

10

mechanism *in vivo*. Furthermore, tumors are heterogeneous and vary from host to host because of genomic instability (7) and plasticity of invasion mechanism (8), and there is debate as to the source and onset of the metastatic phenotype (9,10). Tumor cell invasion, a ubiquitous and rate-limiting step in metastatic disease progression occurs early in tumor progression and represents a viable target for cancer therapy (11).

Disseminating carcinoma cells navigate through the tumor microenvironment, across the basement membrane and into the surrounding stroma (Figure 2). Migration is a highly orchestrated process in which cells are guided both by internal signals and signals from the microenvironment. Mechanical signals, sensed by integrins (12) and other adhesion receptors (13), and chemical signals, sensed by chemokine and growth factor receptors (14), influence the migration of tumor cells. Hence, understanding the mechanisms that guide cell migration in response to various stimuli in the tumor and stromal microenvironments is key to developing therapies that prevent tumor cell migration and render cancer more treatable.

Because it is difficult to isolate the effects of an individual stimulus on cell migration *in vivo*, *in vitro* models have emerged as powerful tools for investigating tumor cell migration. These reductionist *in vitro* assays isolate a subset of stimuli on tumor cell migration, and have greatly enhanced our understanding of the important chemical and mechanical signals that guide tumor cell migration. In this thesis, we leverage the potential for mechanistic insight provided by *in vitro* assays to investigate the migration of single, metastatic breast carcinoma cells and to determine how interstitial flow, a diagnostic and prognostic marker for metastatic disease, influences the migration of these cells.
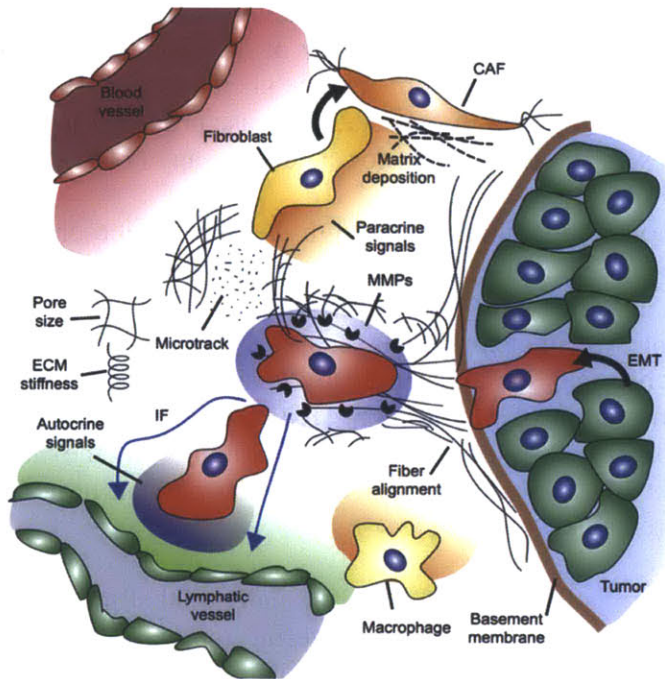
Figure 2. Biochemical and biophysical factors influence the migration of tumor cells. Mechanical signals include stiffness of the ECM, the pore size of the ECM, solid stress, fiber alignment, and fibroblast-generated matrix tension and microtracks. Chemical signals include autocrine gradients, MMPs, oxygen tension, and paracrine signals from the vasculature, lymphatics, and stromal cells (e.g., fibroblasts, from Polacheck et al. (15)).

1.2 Interstitial flow

The ECM is porous and biphasic, comprised of a solid phase bathed in interstitial fluid, which provides a transport medium for nutrients and signaling molecules (16-18). Osmotic and hydrostatic pressure gradients within the ECM drive flow of interstitial fluid through the porous solid phase of the ECM (interstitial flow – IF) (19), and IF convection enhances transport of large molecules to constitutive cells in vascularized tissue (18). Elevated osmotic pressure, lymphatic collapse, solid stress, and increased microvascular permeability contribute to elevated interstitial fluid pressure (IFP) in carcinoma (Figure 3A)(20), and high intratumoral IFP leads to pressure gradients at the tumor margin, which drive fluid flow that eminates from the tumor core to draining lymphatics or venous vasculature in the stroma (Figure 3B) (21).

Neoplastic IF induces lymphangiogenesis (19) and altered ECM architecture by stimulating tumor-associated fibroblasts (22), contributing to an altered tumor stroma. IFP has long been used as a diagnostic (23) and prognostic (24) indicator, as IFP increases with tumor mass for adenocarcinoma (25), high IFP in breast cancer correlates with invasiveness (26), and elevated IFP correlates with probability of metastasis formation (27). IFP has also been used as an indicator for treatment efficacy (28), as treatment of breast cancer with radiation (29) or paclitaxel (30) decreases IFP, increasing tumor oxygenation and rendering the tumor more treatable.

12

As tumors progress, local tumoral IFP approaches microvascular pressure (MVP), which contributes to a low transvascular pressure gradient and reduces transport from the vasculature to the tumor (31). The effects of IFP on transport have been studied in detail in the context of drug delivery (20), and reducing IFP has been shown to increase drug delivery and efficacy (32). However, fluid flow also imparts signals on tumor cells and constitutive stromal cells (Figure 3). Although transvascular transport is reduced in tumor-associated vasculature, high intratumoral IFP (up to 30 mmHg (31)) contributes to large pressure gradients at the tumor margin, resulting in high fluid efflux from the tumor core and elevated IF velocity magnitude. Chary and Jain determined typical IF speeds to be on the order of 0.1-2.0µm/s (21). The magnitude of IF velocity depends on the magnitude of the IFP gradient and the hydraulic conductivity of the tumor, and subsequent work has indicated that the velocity can reach up to 4.0µm/s (33). Computational models demonstrate that IF speed is a function of the ratio of interstitial to vascular flow resistance (34), and when the resistance to IF transport is much greater than the resistance to vascular transport, IF speed at the tumor periphery can reach as high as 10.0µm/s (35).

Recently, the effects of IFP and IF on the biology of the constitutive tumor cells have been investigated. Initial experiments found that IF alters tumor cell proliferation (36), and lowering IFP reduces tumor cell proliferation in mouse models (37), and IF induced intravasation into lymphatic vasculature in a mouse model (38). In general, the effect of flow has been divided based on the mode of stimulus generation and transduction. Chemical signals are generated by gradients in soluble morphogens and chemokines and stimulate cell growth factor receptors (GFRs) and chemokine receptors. Mechanical signals are generated by fluid stresses and stimulate cell adhesion receptors such as integrins.

The convection of soluble signals by interstitial flow provides a host of migration signals to invading tumor cells by transporting both autocrine and paracrine chemokines (Shieh *et al.* review of IF and effects on tumor cell invasion (39)). In recent work by Shields *et al.*, IF was found to increase the metastatic potential of tumor cells through binding of self-secreted chemoattractant via the CCR7 receptor (40). This autocrine signaling, termed "autologous chemotaxis," arises when IF transports secreted ligand downstream, and the balance between convection and diffusion establishes a Peclet number-dependent pericellular gradient, which provides a chemotactic signal in the downstream direction (41). IF also influences fibroblast function, promoting matrix reorganization, differentiation into myofibroblast phenotype (22), and fibroblast migration (42), and these mechanisms prime the stromal environment through MMP secretion and Rho-dependent matrix contraction to promote tumor cell invasion (43).

Computational models have aided in elucidating the effects of IF on the mechanical microenvironment, and the simulations demonstrate that IF applies stress to matrix fibers, which can be sensed by the cell through matrix adhesions (44), and IF imparts shear stress on the cell membrane, the magnitude of which is determined by the arrangement of matrix fibers (45). Interstitial flow increases the migration of vascular smooth muscle cells through increased MMP13 expression, mediated by heparan sulfate proteoglycans

13

(46). Although this work was performed with vascular smooth muscle cells, syndecan expression in breast cancer has been demonstrated (47), though it remains to be seen whether proteoglycans play a role in the tumor cell response to interstitial flow. In preliminary work, we demonstrated that when CCR7 receptors are blocked, tumor cells migrate in the upstream migration, and the data suggest that the upstream stimulus is mechanically-mediated (48).

Although the details of the mechanism guiding cells to migrate upstream has yet to be verified, recent evidence supports the hypothesis that IF imparts competing stimuli on migrating tumor cells (49). The flow-induced expression of MMPs (42), further complicates investigation of IF as a migration cue as the MMPs degrade the matrix, altering the flow field and pressure distribution around the cell. In glioma cells, fluid stress activates MMP1 (50), and secreted soluble MMPs could be convected downstream, degrading matrix on the downstream side of the cell, further activating adhesion molecules on the upstream side, though that remains to be demonstrated. In this thesis, we investigate the chemical and mechanical signals imparted by IF on cancer cells and the crosstalk between these signals. Furthermore, we investigate the details of the mechanism leading to upstream migration, and in so doing, we explore mechanotransduction of IF stresses in 3D.
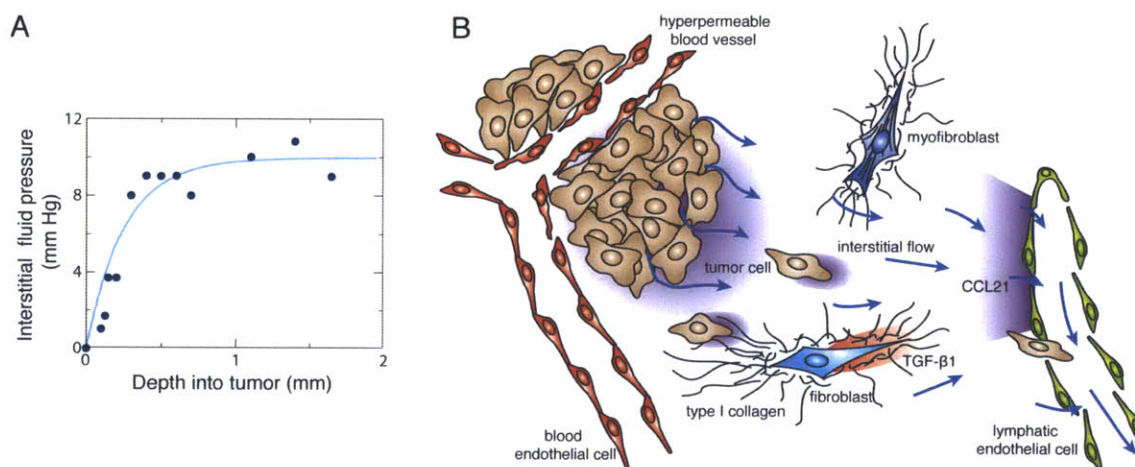
Figure 3. Interstitial pressure gradients in solid tumors drive interstitial flow from tumor associated vasculature to draining lymphatics and venous vasculature in the peritumoral stroma. A) Pressure profile for adenocarcinoma in a rat model demonstrates high pressure gradients at the tumor margin. Pressures are normalized to stromal pressure (p_{stroma}=0 mmHg, from Chauhan et al. (20)). B) Schematic demonstrating the direction of fluid flow in a solid tumor. Fluid flow influences chemical gradients (purple) and matrix architecture (black) through signaling to stromal cells (modified from (51)).

1.3 Tumor cell migration

Recently developed experimental platforms and computational methods have provided much insight into the mechanisms by which tumor cells migrate in the surrounding stroma. In epithelial tissues, cells are tightly connected to their neighbors and form polarized cell sheets with high levels of E-cadherin expression. During the formation of metastatic lesions in carcinomas, epithelial cells undergo genetic and epigenetic changes that induce a phenotypic transition, in which cells lose E-cadherin expression (52), reducing homophilic cell-cell connections, and express vimentin (53), N-cadherin (54), and other fibroblastic markers (Reviewed by Thiery (55)). This phenotypic switch is known as the epithelial to mesenchymal transition (EMT), and results in cells of epithelial origin acquiring a phenotype more amenable to migration and invasion into the surrounding tissue. The migratory phenotype is varied and dynamic, with invading cells migrating individually or collectively and modulating the mechanism of migration with changes in the stromal properties (review of migration mechanisms by Friedl & Alexander (8)).

Mesenchymal cell migration is an orchestrated process, requiring ECM remodeling, extension of protrusions through actin polymerization, formation of new adhesions, molecular motor-mediated cell contraction, and the release of adhesions at the trailing edge (Reviewed by Lauffenburger & Horowitz (56) and Ridley et al. (57)). Migration through 3D matrices is termed invasion, and tumor cell invasion is mediated by invadopodia, specialized Src-kinase-dependent protrusions that are selectively observed in metastatic cells and extend into the ECM to probe the proximal chemical and mechanical microenvironment (58). In general, cell migration is a stochastic process (59), and in the absence of an external gradient or directional cue, cells migrate randomly. However, when presented with a directional cue, such as a chemokine gradient, the internal signaling machinery becomes polarized and cells migrate with directional bias (60). Although an external directional cue will bias the migration direction of cells, the cells still migrate stochastically, oscillating between a state characterized by directionally persistent migration and a stationary state, in which the cell reorganizes the cytoskeleton and changes its direction of migration (61).

Tumor cell migration direction and speed can be modulated independently by external signals and by internal cytosolic factors. For example, shallow concentration gradients of epidermal growth factor (EGF) increased the speed and persistence of MDA-MB-231 breast cancer cells but did not bias the direction of cell migration, while steeper gradients induced cell migration toward increasing EGF concentration (62). Furthermore, the molecular machinery that regulates the extension of protrusions and direction of migration can be modulated independently from signals that govern the rate of migration. In MTLn3 adenocarcinoma cells, inhibition of PI3K decreased cell motility but did not affect directional bias of protrusion extension toward an EGF gradient, and conversely, inhibition of cofilin decreased the directional bias of protrusion extension while not affecting cell motility (63).

The stochasticity of cell migration and the fact that direction and speed can be modulated independently complicates the use of end-point migration assays. For example, migration with high speed and low persistence cannot be distinguished from low speed, highly persistent migration. This issue is compounded in transwell assays, where only the number of cells reaching and crossing the membrane is measured, and increased migration speed with random direction could be confused with directionally biased migration. Furthermore, there is often significant cell-cell heterogeneity in cell migration characteristics, and migration statistics are often averaged over a cell population. These bulk, or population-averaged metrics can obscure aspects of the migratory response that may be important for understanding the response of tumor cells to various stimuli. These disadvantages can be overcome by the use of live-cell imaging in microfluidic systems. For example Haessler et al. used population histograms and scatter plots to identify subpopulations of cells that respond uniquely to interstitial flow, with downstream migrating cells moving with high directional persistence and upstream migrating cells moving faster but with less directional persistence, supporting the hypothesis that flow imparts simultaneous and competing stimuli to tumor cells (49). With the limitations of traditional, bulk assays in mind, we developed a microfluidic system to allow imaging of full time-resolved migration dynamics for each cell in a population to allow maximum resolution in determining the effects of interstitial flow on tumor cell migration.

A key assumption in many reductionist experiments is that the stimuli, particularly chemical and mechanical signals, act in parallel. However, the migrating cell acts as a signal integrator, sensing simultaneous stimuli, activating intracellular pathways, and responding through organized processes that culminate in the extension of protrusions and subsequent migration (Figure 4). Furthermore, tumor cells invade stromal tissue through a variety of mechanisms, and the process of migration is dynamic and a function of tissue substrate (8). As we look to develop the next generation of assays for tumor cell migration, it is important to consider the crosstalk between chemical and mechanical stimuli, and the role it plays in guiding the migration of tumor cells. Interstitial flow inherently couples mechanical and chemical signals, as flow imparts stresses and alters local chemical transport. In this thesis, we explore the crosstalk between chemical and mechanical signals and investigate how this crosstalk contributes to directional regulation of tumor cell migration in response to IF.

MECHANICAL

Stimuli:
- ECM Topography
- ECM Stiffness
- Force/Pressure

MMP secretion
Matrix synthesis
GFR-modulated integrin expression

Interstitial Flow

Integrin-modulated GFR expression
MMP-released ligand

Key receptors:
- Integrins
- HSPGs

Key signaling:
- Rho/ROCK
- Myosin contraction

CHEMICAL

Stimuli:
- Autocrine Signals
- Paracrine Signals
- Oxygen Tension

Key receptors:
- GFRs
- Chemokine receptors

Key signaling:
- PLCγ
- Cofilin

Figure 4. Chemical factors influence the cellular response to mechanical factors and vice versa. MMP and matrix secretion modulates the stiffness and pore size of the surrounding matrix, while growth factor receptor (GFR) activation influences integrin expression and activation. Interstitial flow induces mechanical signals through fluid shear and pressure stresses, while simultaneously inducing chemical signals through convection of autocrine and paracrine signaling factors (from (15)).

1.4 Chemotaxis

Traditionally, chemical migratory stimuli, mediated primarily by soluble chemical signals, have been considered independently of mechanical stimuli. Gradients in soluble molecules can guide the migration of tumor and stromal cells and modulate cancer progression (64). Tumor cells and stromal cells sense the local concentration of chemokines and growth factors through surface receptors, and a recent review highlights the key factors and pathways involved in chemotaxis in cancer progression (14). Chemokine receptors are often up-regulated in cancer cells *in vivo* (64), and both tumor cells and stromal cells migrate in response to chemokine gradients. Chemokines can be secreted autologously, released from the matrix, or secreted by stromal cells, and cells respond to the magnitude of the transcellular chemokine gradient as well as the mean chemokine concentration (65). Eukaryotic cells amplify gradients intracellularly, downstream of the chemokine receptors through positive feedback signaling loops and signal inhibition, resulting in large intracellular gradients in response to external gradients as small as 2-10% between the anterior and posterior ends of the cell (66), (67).

Protrusion formation is crucial to cell polarization, and the regulation of actin polymerization is key to directional sensing and migration of tumor cells. Chan *et al.* identified two transients in actin polymerization in response to epidermal growth factor

17

(EGF) stimulation (68). Subsequent experiments have identified the first transient to be regulated by PLCγ, which activates cofilin, an actin severing protein. Cofilin activation generates free barbed ends on actin filaments, allowing Arp2/3-mediated actin polymerization and subsequent dendritic actin network extension (63), (69). This first, PLCγ-mediated transient is required for directional sensing of EGF gradients (70), but the second transient is PLCγ-independent and required for protrusion maturation. Hill *et al.* determined that the second transient in actin polymerization is mediated by PI3K (71) and likely involves Rho GTPases such as Ras, Rac, and CDC42. Inhibiting PI3K alters the dynamics of lamellipodia formation but does not prevent directional sensing or biased protrusion formation (67).

Although much recent effort has been devoted to understanding the mechanistic details of EGF signaling, and computational models have been developed to simulate signal transduction from EGFR to actin polymerization (72,73), myriad chemokines and their cognate receptor counterparts direct tumor growth and dissemination *in vivo* (14,74). The chemokine (C-C) motif ligand 21 (CCL21), also known as secondary lymphoid-tissue chemokine (SLC) and 6Ckine, is preferentially expressed in lymph nodes, bone marrow, and lung, frequent destinations of breast cancer metastasis (74). Although the ligand and its cognate receptor, C-C chemokine receptor type 7 (CCR7), were first identified as key signaling components in dendritic cell homing to lymphatic vasculature (75,76), it has been shown that CCR7 is significantly upregulated in primary breast tumor tissue compared to normal mammary gland tissue (74), and CCR7 has been indicated as a strong marker for axillary lymph node metastases in breast cancer (77). CCR7 and CCL21 are highly expressed in tumors with lymph node metastasis, and patients with high CCR7 experienced shorter survival period than those with low expression (78).

Interestingly, CCL21 induces lymphangiogensis, and tumors that express CCL21 have been shown to evade the immune system and recruit stromal leukocyte populations (79). Furthermore, a subset of cancer cell lines, including MDA-MB 231, express CCL21 (80) and CCR7 (81,82), and CCL21 induced transient polymerization of filamentous actin (74) and increased resistance of MDA-MB 231 to detatchment-induced cell death (83), and gradients of CCL21 induced directional migration of MDA-MB 231 (74). Because some tumor cells express CCL21 and migrate in response to gradients of CCL21, the CCR7-CCL21 pathway acts as an autocrine signaling loop, and gradients of self-secreted ligand can induce chemotaxis. Shields *et al.* have demonstrated that such autocrine gradients can guide chemotaxis in cells exposed to IF. In this thesis, we implement a microfluidic platform to improve upon the experimental system used previously to study CCR7-CCL21 autocrine chemotaxis, and we culture cells in a physiologically relevant matrix to investigate the effect of autocrine gradients on tumor cell migration in response to interstitial flow.

1.5 Mechanotransduction

Cell migration is a coordinated process involving protrusion extension, adhesion formation, cell contraction, and adhesion release (56). Consequently, matrix adhesion formation and turnover are key steps in regulating migration, and interfering with the molecular regulators of matrix adhesion is a potential method of halting tumor cell migration and preventing the formation of metastases (84) (85) (86). Integrins are tension-sensitive adhesion molecules that mediate cell adhesion and migration in a variety of ECM materials, including collagen (87). Integrin ligation by the ECM induces clustering of integrins and localization of various structural and signaling proteins to the ligation site, forming a reinforced plaque known as a focal adhesion (FA) (88) (Figure 5). These FA plaque proteins form a 40 nm thick mechanical linkage between the cytoplasmic integrin tails and the actin cytoskeleton (Figure 5)(89), comprising a tension sensitive, direct mechanical connection between the (ECM) and the cytoskeleton. Constitutive FA proteins such as focal adhesion kinase and paxillin serve as key components in the signaling cascade by which cells transduce mechanical signals into biological responses (mechanotransduction) (13,88).
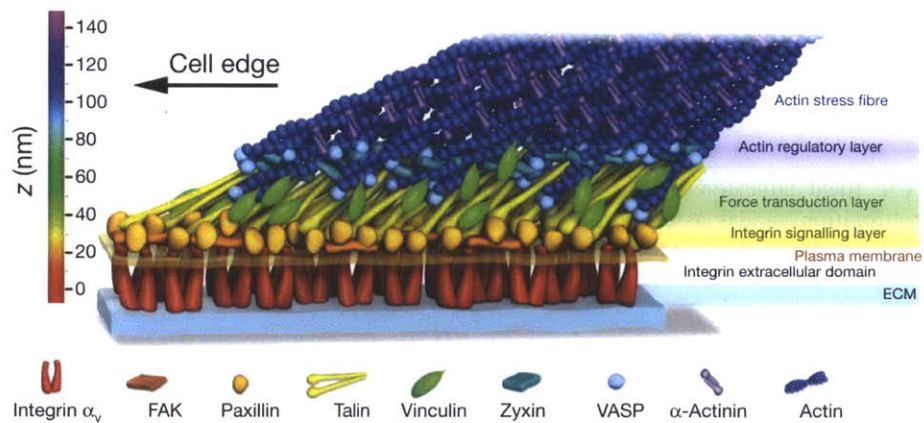
Figure 5. Nanoscale architecture of focal adhesion. The ECM is mechanically connected to the cytoskeleton through a plaque of FA proteins. The structure is mechanically sensitive, and local force causes accumulation of various FA plaque proteins (modified from (89)).

Signal transduction pathways that regulate cell survival, migration, and proliferation can be activated by mechanical force, and FAs act as cellular stress sensors, altering constitutive FA protein composition and initializing signaling cascades in response to force-induced deformation of FA structural proteins (90). The focal adhesion kinase (FAK) is a constitutive signaling element of FAs and regulates myriad cell processes including cell fate, tissue invasion, matrix assembly, cell mobility and cytoskeletal tension (91), and elevated FAK expression and kinase activity are correlated with progression to a highly malignant and metastatic phenotype in human cancer (92). Increased FAK activity increases tumor cell invasion, and blocking FAK inhibits

invasion and decreases the formation of metastases in human cancer (92). Consequently, FAK has been identified as a potential drug target for treating carcinoma (85).
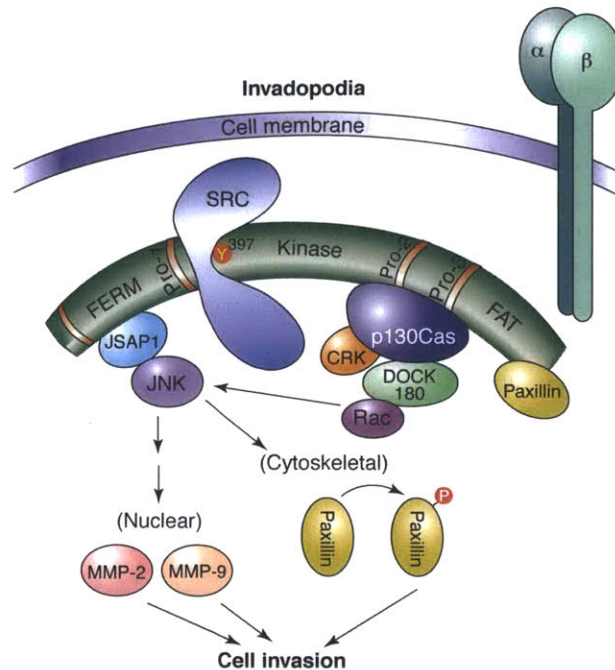
Figure 6. The focal adhesion kinase interacts with many key signaling molecules and regulates cell invasion, proliferation, matrix assembly, and cytoskeletal tension. Effects on cell invasion are mediated by paxillin phosphorylation (Modified from (92)).

FAK binds directly to $\beta 1$-integrins (93), and tensile force applied to $\beta 1$-integrins induces a conformational change in the cytoplasmic tail of integrins that promotes FAK binding. The $\beta 1$-integrin-FAK complex promotes a FAK conformation that results in autophosphorylation at tyrosine 397 (FAK^{Y397}) (92). FAK^{Y397} binds to and activates Src (94), a kinase with broad activity that is upregulated in human carcinoma (95) (Figure 6). Src further phosphorylates FAK, and the resulting FAK/Src signaling complex regulates integrin affinity to ECM (96) and integrin-mediated traction forces (95). FAK can be transphosphorylated at Y397 by growth factor receptors such as EGFR and PDGFR, leading to formation of the FAK/Src signaling complex, and thus FAK represents an early convergence of mechanically activated and growth factor activated signaling (92). Interestingly, blocking FAK reduces motility of cells on 2D substrates and invasion in 3D, and overexpression of Src recovers the losses in motility but not 3D invasion due to the role of FAK in governing MMP expression (92) (**Table 1**).
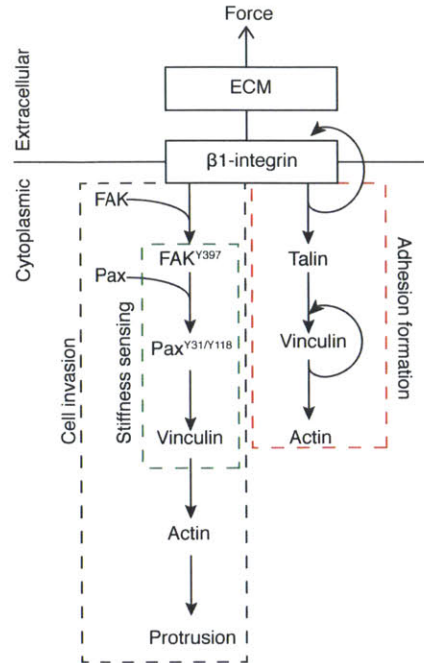
Figure 7. Vinculin is recruited to integrins via two pathways. Initial adhesion formation is mediated by talin, and tension induces unfolding of cryptic binding domains that allows vinculin binding. Further vinculin recruitment is mediated by FAK and requires paxillin phosphorylation. The FAK/Pax/Vin signaling component of this pathway is required for cell stiffness sensing and durotaxis.

FAK^{Y397} recruits and phosphorylates paxillin, a FA protein that forms early in FA assembly (97). Piconewton forces applied to β1-integrins result in local accumulation of paxillin (98), and paxillin-containing FAs elongate in the direction of applied force (99). Paxillin activity and expression is correlated with the formation of metastases in human carcinoma (100,101). Paxillin is a key regulator of actin polymerization through its recruitment of Rho and Rac (102), and this regulation of actin, in combination with its force-sensitivity, has implicated paxillin as a mediator of protrusion formation in response to applied stress at FAs (103). Because protrusion formation is required for migration, paxillin has been identified as a critical and necessary component in directing cell migration in response to mechanical stimuli (104).

Phosphorylated paxillin recruits vinculin to FAs, and vinculin colocalization with β1-integrin is associated with mechanical strengthening of the ECM-actin adhesion complex (105). Vinculin, along with α-actinin and β1-integrins, was one of the first FA proteins identified that localizes to regions of applied force (106). Vinculin is a scaffold protein with no known catalytic activity but that binds F-actin, talin, α-actinin, paxillin, tensin, zyxin, ezrin, p130Cas, Arp2/3, VASP, and itself (107), and because the globular head domain binds talin while the tail domain binds F-actin, vinculin mechanically links integrins (through talin) and actin (108). Vinculin is recruited to integrins via two pathways (Figure 7); in one pathway, tension across β1-integrins is transmitted to talin, opening cryptic binding domains in talin and allowing vinculin to bind (109,110). The second pathway involves tension-mediated FAK autophosphorylation at Y397, which

21

induces phosphorylation of paxillin at Y31/Y118 and recruits vinculin to FAs (111). Although cells can still migrate on 2D surfaces if either pathway is blocked, 3D invasion and migration in response to mechanical cues requires both pathways(112) (113) (Table 1).

As a mechanical link between integrin and actin, vinculin is critical for many cell processes, and within the last decade vinculin has become widely used as a marker for local stress magnitude. The concentration of vinculin recruited to an FA increases with the duration and magnitude of applied force (114) (115), while the residence time of vinculin at an FA is linearly related to the local traction force (116). Because vinculin concentrations increases with force, measurement of local fluorescence intensities of fluorescently tagged or stained vinculin can be used to infer the magnitude of force at a given adhesion, whether the force is applied externally (90) or is generated internally by the cell (117). Recently, a vinculin mutant has been developed that uses FRET to give a real-time measure of stress magnitude within an adhesion (110). In this thesis, we developed a breast cancer cell line that stably expresses a vinculin-GFP fusion protein, and by tracking the fluorescence intensity of this protein, we infer local cell-matrix stresses. Furthermore, we use these fusion proteins along with microfluidic devices to investigate the role of the β1-integrin/FAK/paxillin/vinculin signaling cascade in directing cell migration in response to IF.

1.6 Cell migration directed by external mechanical cues

The tension sensitivity of FAs and their role in regulating adhesion formation and dissolution during cell migration implicate a role for mechanical forces in the regulation of directional cell migration. Indeed, when cultured on a substrate with a gradient in mechanical stiffness, cells will migrate toward regions of increased stiffness (durotaxis) (118), and fluid shear stress regulates directional migration of endothelial cells (mechanotaxis) (119). Furthermore, durotaxis and mechanotaxis both require FAK signaling through autophosphorylation at Y397 (120) (121). Durotaxis is thought to result from a force balance between cell contractile force and adhesion tension: cells exert greater traction forces on stiffer substrates, and higher traction leads to FA activation, which induces local signaling pathways that result in protrusion formation and eventual migration (118). Consistent with this proposed mechanism, cells extend protrusions at regions of high substrate traction (122), and when strain is applied to a substrate, cells migrate toward regions of maximum tensile strain, where adhesions are in tension and FAs are activated(113) (Figure 8). Although these studies point to a relationship between force, FA activation, and migration, it remains unclear whether force causes migration through FA activation and signaling, or if migration is activated through other signaling pathways, and the migration causes FAs to form at the leading edge. To test this "chicken and the egg" dilemma, Xia et al. constructed anisotropic surfaces that controlled the direction of FA growth, and the authors found that cells migrated toward the direction of elongated vinculin-containing FAs (123,124). These data support the pathway where force, either applied internally (duortaxis) or externally (mechanotaxis), causes activation and elongation of FAs through FAK signaling, and FA activation leads to migration toward the region where matrix adhesions are under maximum tension.
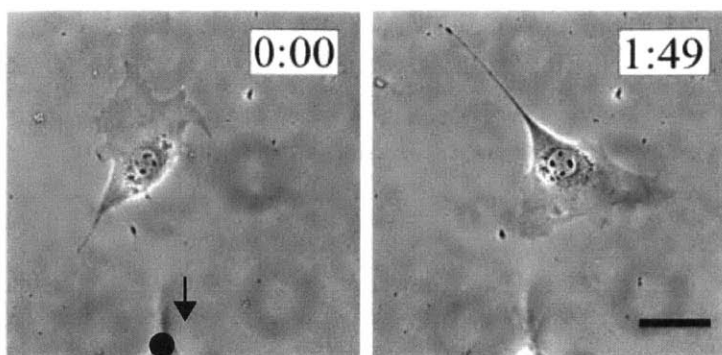
Figure 8. Substrate strain induces directional cell migration. A microneedle was inserted into the silicone substrate in close proximity to a fibroblast (black circle) and displaced in the direction indicated by the black arrow. Within 2hrs, the fibroblast reversed the direction of migration, turning to migrate toward the region of maximum substrate tension (scale bar 40 μm, modified from (118)).

Determining the force-sensing mechanism that underlies mechanotaxis and durotaxis is difficult because knocking out various FA proteins halts migration altogether (**Table 1**). Of particular interest in mechanotransduction is the FAK/paxillin/vinculin signaling axis, which is required for durotaxis (104). Each signal is downstream of β1-integrins, and knocking out each component has a different effect on cell migration (Table 1). Interfering with FAK or vinculin not only disrupts migration in response to mechanical cues, but also reduces 3D invasion (92) (125); however, knocking out paxillin attenuates durotaxis and migration in response to substrate strain (104), but does not affect the ability for cells to migrate in 3D (126). Furthermore, silencing paxillin reduces adhesion strengthening and Rac-dependent protrusion formation at regions of local stress (122) (126) and blocks durotaxis but not chemotaxis (104). These data taken together implicate paxillin as the force sensor in governing migration in response to mechanical stimuli. In this thesis, we examine the role of paxillin in mediating the mechanotransduction of IF stresses, and specifically, we investigate the FAK/pax/vin pathway required for durotaxis to determine the role of this stiffness-sensing pathway in governing migration in response to fluid stresses.

Table 1. Effect of knocking out various focal adhesion proteins on cell migration.

FA protein	Effect of knockout on...						Source
	FA formation (2D)	FA turnover (2D)	2D migration	3D invasion	Durotaxis (2D)	Chemotaxis (2D)	
FAK	+*	X	X	X	X	X	(127) (113) (92)
Paxillin	+	-	-	0	-	0	(127) (126) (104)
Vinculin	-	0	+	X	-	0	(127) (125) (128)

* = increased # of immature adhesions
0 = no change
X = blocked

1.7 Mechanotransduction in 3D

Much of the current understanding of integrin-mediated mechanotransduction and stiffness sensing is built from experiments in which cells are cultured on stiff 2D substrates (129), but high substrate stiffness (glass~69GPa, normal mammary stromal ECM stiffness ~200Pa) influences cell morphology, motility, and cell fate (130). Furthermore, high substrate stiffness (>5kPa) induces formation of β1-integrin FAs and favors the metastatic phenotype in mammary epithelial cells (131) (12). Consequently, the relevance and mechanistic details of force-induced β1-integrin signaling when cells are cultured in physiologically relevant soft, 3D ECM remain unknown. With the advent of microfabrication technology and the advancement of tissue engineering techniques and polymeric ECM mimics, new 3D assays for mechanobiology are providing insight into mechanotransduction in 3D (132).
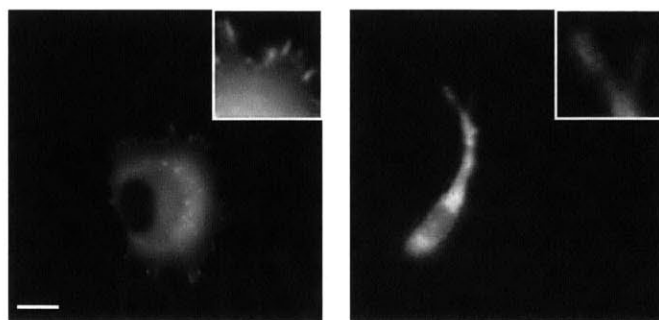
Figure 9. Focal adhesion structure varies in 2D and 3D environments. Left, a fibrosarcoma cell cultured on a 2D collagen coated glass substrate, and stained for vinculin. Punctate focal adhesions can be seen at the periphery of the cell. Right, the same cell type, also stained for vinculin, showed remarkably different FA structure when cultured in 3D collagen gel. No noticeable punctate FAs are observed (Scale bar 10µm, from (133)).

As discussed above, integrin-based adhesions between cells and stiff 2D substrates are characterized by punctate FAs; however, these punctate adhesions are absent when cells are cultured in 3D (134) (Figure 9), and FA proteins like vinculin have different effects on cell motility in 2D and in 3D (125,133) (Table 1). Experiments in which cells were cultured in tissue-derived 3D matrices demonstrate that these 3D adhesions are more physiologically relevant than 2D FAs (135), and much recent work has investigated the mechanisms underlying the differences in adhesion architecture for cells cultured in 2D and 3D (136). From the perspective of external stimuli, there are two primary differences between a 2D substrate that presents a stiff surface with uniform matrix coating and a 3D fibrillar matrix: ECM stiffness and geometric presentation of adhesion ligands. 3D matrices are softer (2mg/ml collagen type I gel modulus ~328Pa), but importantly, adhesion ligands are confined to matrix fibers, and substrate geometry is known to regulate tumor cell invasiveness (137). However, exploring 3D mechanotransduction is complicated by the mechanics of 3D fibrillar materials (136), in which stiffness is coupled to porosity and adhesion ligand density, both of which also influence cells (138). For example, increasing stiffness either requires increasing matrix crosslinking, an effect that decreases pore size and influences tumor cell invasiveness (139), or increasing matrix density, which also decreases pore size and additionally presents more matrix ligand (8).

Although the matrix properties are coupled fundamentally, new techniques are being developed to analyze cells in 3D. In particular, resolving 3D stresses at FAs for cells on 2D substrates is providing mechanistic insight into how cells apply force (140) (141), and 3D traction force microscopy has revealed that cells exert tensile stresses when cultured in 3D materials (142). Furthermore, although the technique couples pore size and stiffness, cells have been shown to durotact in 3D (143). However, mechanistic details are difficult to discern due to the lack of a proper method to apply force locally to cells analogous to optical traps used to investigate the molecular underpinnings of mechanotransduction in 2D, even as 3D techniques are giving rise to more realistic tissue constructs (144) (145). In this thesis, we implement interstitial flow as a method for applying force to cells in a 3D construct. By combining this experimental technique with high-resolution imaging, we explore the architecture of 3D adhesions and how they direct migration through 3D fibrillar matrices.

1.8 Focal adhesions in cancer

FA proteins are often overexpressed in carcinomas, and because FA-associated proteins are integral elements of mechanotransduction and cell migration, which in turn is critical in the metastatic cascade, FA proteins have been investigated as cancer therapeutic targets (Table 2). Carcinoma progression is associated with desmoplasia, pathologic deposition of ECM, and integrin expression is modulated in response to the neoplastic ECM (146), and due to these changes in integrin expression, integrins have been explored as a therapeutic target for treating various solid tumors (Table 2) (86). Cilengitide, a synthetic peptide that binds α_v integrins was developed as a glioblastoma drug much lauded in preclinical and early clinical trials (146); however, the drug failed in phase III as there was no detectable effect compared to control (Table 2). However, other drugs

have been developed to target intracellular signaling components in the mechanotransduction cascade. The Src/FAK signaling complex, the signaling nexus of cell adhesion, migration, proliferation, and apoptosis has been explored as a possible drug target. Src is overexpressed in carcinoma, and the level of expression correlates with the probablility of metastasis formation (95), and FAK is also overexpressed in carcinoma, while phosphorylation at Y397 is an indicator for prognosis (92) (85). Dasatinib (Sprycel by Bristol Myers Squibb) targets Src and has been approved for treatement of myelogenous leukemia (146) and has shown promise for treating breast cancer when used in combination with approved chemotherapeutic agents (Table 2), while multiple drugs are in development to target FAK(147).

The effect of interfering with paxillin and vinculin in treating carcinoma is similar to the effect of knocking out the respective protein on 2D and 3D migration (Table 1). Paxillin expression is correlated with the formation of metastases (100,101), and knocking out paxillin decreased lung metastases in a mouse model (148). Vinculin, on the other hand, has been identified as a tumor suppressor (107), and vinculin overexpression reduced primary tumor formation and metastatic cell dissemination (149-151). Although there are no current drugs in clinical trials for paxillin or vinculin, understanding the mechanism by which FA proteins contribute to the metastatic cascade will provide further candidates for therapeutic intervention. In this thesis, we explore the role of IF in altering FA protein distribution, and further explore the role of FA proteins in directing the migratory response of breast cancer cells in response to IF. By establishing connections between FA protein activity and cell migration, we hope to identify new therapeutic targets that would interfere with the migration of tumor cells and lower the incidence of metastasis formation.

Table 2. Current regulatory status of drugs developed to treat solid tumors by targeting FA proteins.

Drug	Target	Solid cancers	Regulatory status	FDA clinical trial identifier** & references
Cilengitide	αvβ3 αvβ5	Glioblastoma	Failed phase III	NCT00689221 (146) (86)
		Breast cancer	Phase I	NCT01276496
Volociximab	α5β1 (antibody)	Renal	Phase II	NCT00100685 (146)
ATN-161	α5β1 (peptide-based)	Renal	Phase II	NCT00131651 (146)
		Breast	Reduces growth and metastases in mice	(152)
Dasatinib	Src family kinases	Chronic myelogenous leukemia	Approved	(146)
		Breast cancer	Phase II	NCT00371345
			Phase II with paclitaxel (chemotherapeutic agent)	NCT00820170
			Phase I with crizotinib (ALK inhibitor)	NCT01744652
GSK2256098	FAK	Breast cancer*	Phase I	NCT01138033 (147)
PF-00562271	FAK	Breast cancer*	Phase I	NCT00666926 (153)
VS-6063	FAK	Ovarian cancer	Phase I with paxlitaxel (chemotherapeutic agent)	NCT01778803

* Other solid tumors, including head & neck, ovarian, and esophageal.
** from clinicaltrials.gov

1.9 Thesis aims and overview

1.9.1 Thesis aims

In this thesis, we will explore the role of interstitial flow in the progression of breast cancer toward a metastatic phenotype. In particular, we examine the chemo-mechanical crosstalk (Figure 2) that influences cell migration in response to interstitial flow, advancing current understanding of IF in the tumor microenvironment by considering fluid stresses in addition to the autocrine gradients that promote autologous chemotaxis. Investigating the effects of fluid stresses on tumor cell migration requires the development of an experimental technique that allows application of a predictable and repeatable IF flow field to tumor cells embedded within a physiologically relevant 3D matrix, and the system must allow monitoring of the transient migratory response tumor cells embedded within the matrix. To accomplish these goals, the thesis is divided into three specific aims:

1. Develop a microfluidic platform for applying interstitial flow to tumor cells embedded within a physiologically relevant extracellular matrix

2. Investigate the effects of autocrine gradients induced by IF on tumor cell migration

3. Elucidate mechanism of mechanotransduction of IF stresses and determine role of mechanotransduction in guiding tumor cell migration

1.9.2 Thesis overview

In Chapter 2, the current experimental platforms for investigating interstitial flow and 3D tumor cell migration are reviewed. Drawing from the literature and limitations in current platforms, design criteria for a new platform to investigate IF are established. We then introduce two microfluidic platforms that have been designed to meet these criteria for investigating the effects of IF on tumor cell migration.

In Chapter 3, the role of chemical transport and autocrine gradients that result from IF are discussed. In particular, we focus on the CCR7 pathway, which has been implicated in directing tumor cell migration for metastatic carcinoma cells when exposed to flow. We discuss the directional cues that autocrine gradients impart to tumor cells, and we establish parameters that govern when these autocrine signals are dominant and direct cell migration.

In Chapter 4, we focus on the role of fluid stresses imparted on tumor cells exposed to flow. In particular, we elucidate the difference in directional stimulus between the autocrine gradients and fluid stress activated focal adhesion signaling. We further highlight the consistency between this focal adhesion signaling and durotaxis. We conclude by discussing the role of paxillin in governing the migration response of cells to interstitial fluids stresses.

28

We discuss future directions and conclusions in chapter 5. In particular, we highlight the generality of IF and explore examples from the literature to demonstrate other instances in which IF directs cell morphology and migration. Finally, we wrap up with a discussion of the mechanism by which tumor cells sense and respond to fluid stresses, and we compare this mechanism to established mechanisms such as durotaxis and mechanotaxis. We emphasize that although our experiments employed interstitial flow, the underlying signaling mechanism is much more general and we hypothesize that the effect of asymmetric stress distribution in cell adhesions is an important physiologic signal *in vivo* beyond regulating cell migration in response to IF.

Chapter 2: Development of a microfluidic platform for interstitial flow[*]

2.1 Introduction and review of current devices for investigating tumor cell migration

Understanding the details and dynamics of metastasis is complicated by the myriad cell types, signaling molecules, ECM components, and cellular interactions involved in EMT, migration, and intravasation. Consequently, in vitro systems have been developed to isolate the effects of an individual stimulus on steps of the metastatic cascade (Figure 10) (For review of in vitro systems to investigate the metastatic cascade see Polacheck et al. (15)). Typically these systems involve one or multiple cell types seeded on a surface or in a gel of reconstituted ECM components (36,40,144,154-161). Microfluidics has emerged as a powerful tool for manipulating molecular concentrations, molecular gradients, and physical stimuli to cells seeded in these systems. In particular, soft lithography allows for the construction of cellular bioreactors with small length scales and sample sizes, rapid prototyping, and optical properties that allow for live-cell imaging (162,163). Although in vitro systems have been developed to isolate effects of pressure gradients and flow on cell physiology, the physiological relevance of these systems is limited by 2D or pseudo-3D culture, where cells are seeded on a surface and overlaid with a gel(40). Furthermore, many systems are not designed to allow live-cell imaging to observe cell dynamics and cellular responses in real-time.

The stochasticity of cell migration and the fact that migration direction and speed can be modulated independently complicates the use of end-point migration assays. For example, migration with high speed and low persistence cannot be distinguished from low speed, highly persistent migration. This issue is compounded in Transwell assays (Boyden chamber), where only the number of cells reaching and crossing the membrane is measured, and increased migration speed with random direction could be confused with directionally biased migration (Figure 11). Furthermore, there is often significant cell–cell heterogeneity in cell migration characteristics, and migration statistics are often averaged over a cell population. These bulk, or population-averaged, metrics can obscure aspects of the migratory response that may be important for understanding the response of tumor cells to various stimuli. These disadvantages can be overcome by the use of live-cell imaging in microfluidic systems. For example, Haessler et al. used population histograms and scatter plots to identify subpopulations of cells that respond uniquely to interstitial flow, with downstream migrating cells moving with high directional persistence and upstream migrating cells moving faster but with less directional persistence (49), an observation that could not be made with previous experiments in a transwell assay (40). The directional bias of migration is an important in understanding the effects of IF on tumor cell migration. We developed a system where directional bias of migration can be observed, and we address the validity of previously established models in the context of 3D directed cell migration.

---

[*] Sections of the introduction for this chapter have been published previously. See (15).
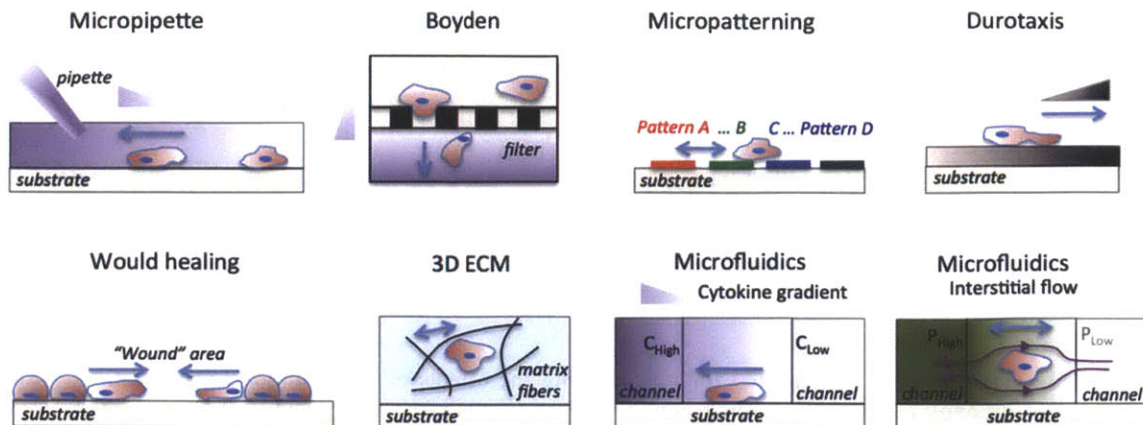
Figure 10. Assays for investigating metastatic cascade. Micropipette: a pipette is placed in the vicinity of the cell and a chemoattractant solution is injected into the culture medium establishing a growth-factor gradient (164). Boyden (165) (or Trans- well) chamber: cells are seeded in suspension in the top chamber and migrate through the porous filter (black rectangles) in response to a chemokine gradient, which is established by the different culture medium concentrations in the top and bottom chambers. Micropatterning (166): cells are seeded on patterns of different geometry, size and surface coatings and their migration characteristics are monitored. Durotaxis (118): cells are seeded on a substrate of variable stiffness and respond by changing traction forces, cell spread area, and migration direction. Wound healing (167): a ''wound'' is formed on a confluent tumor monolayer, and the wound closure dynamics are monitored. 3D ECM (168): cells are seeded inside the 3D ECM and migrate depending on the ECM architecture (stiffness, pore size, and ligand concentration); ECM fibers are outlined with black curved lines. Microfluidics (48,65,159,169,170): cytokine gradients can be established in a 3D matrix by flowing different chemokine concentration (C_{high} - C_{low}) solutions in the left and right microchannels; Interstitial flow can be established by adjusting the hydrostatic pressure (P_{high} - P_{low}) in the left and right microchannels; streamlines are indicated with dark magenta lines. Micropipette, Boyden chamber and microfluidics assays enable control of biochemical gradients. Durotaxis, 3D ECM and microfluidics assays enable control of biophysical forces (ECM stiffness and interstitial flow). Wound healing and micropatterning assay enable control of intercellular distances, whereas only micropatterning assays enable control of substrate topography. Growth-factor gradients are indicated by the purple triangles. ECM stiffness gradients are indicated by the dark brown triangle. Blue arrows indicate direction of tumor cell migration, and pressure gradients are indicated by the shades of green (Figure and caption modified from Polacheck et al. (15)).
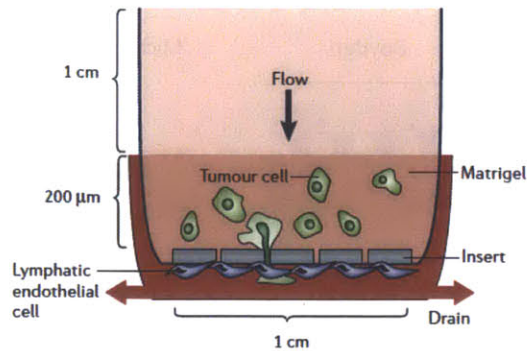
Figure 11. Transwell assay modified for investigating the effects of IF on tumor cell migration. Flow is established by applying a pressure drop across a Matrigel plug in which tumor cells are seeded. After a given amount of time, the membrane (insert) is removed, and the number of cells that migrated through the membrane are counted; therefore, the quantification of cell migration is biased by only counting cells that migrate downstream (modified from (144)).

In order to fulfill the objectives presented above, we need to design an experimental apparatus in which we can culture cells, subject cells to a repeatable and predictable flow field, and maintain high cell viability. To ensure experimental repeatability, the system must be easily fabricated and system variability must be low. The system needs to be optically transparent and biocompatible to allow imaging and to maintain high cell viability. The system must be easily transferred from the incubator to imaging stage and easily sterilized to avoid bacterial and fungal contamination.

In order to improve upon previous devices and provide greater physiological relevance, cells must be suspended in a 3D matrix of reconstituted ECM components. Consequently, the system must include a region where cell-matrix suspension can be added and polymerized. A pressure drop is needed to drive fluid flow through the 3D cell construct, so the system must be closed to the atmosphere but allow input and outlet ports for sterile cell media. The geometry of the flow chamber must be simple so the pressure drop induces a predictable flow field.

2.2 System Design

Soft lithography is an efficient, cheap, and robust technique for fabricating biocompatible microfluidic devices (171). We have developed two microfluidic systems that are fabricated using soft lithography and meet the design requirements mentioned above. The first system, termed the "microinjection device" (Figure 12A) was used for preliminary investigation into the role of IF on tumor cell migration and is discussed primarily in Chapter 3. The second system, termed the "high throuput device" (HTD, Figure 12C) is an improved system, modified from a device developed to study angiogenesis (162). The HTD was used to study mechanotransduction of fluid stresses, and is discussed primarily in Chapter 4. However, here we discuss fabrication and implementation of both systems, which is similar for each device. Consequently, we discuss fabrication and use in general and highlight differences between the two systems when appropriate.

The flow system consists of a microfluidic chip, fabricated from polydimethysiloxane (PDMS), with etched features including a cell culture region and media ports. The PDMS chip can be autoclaved and is sealed with a glass coverslip to allow for sterile cell culture. For the microinjection device, media channels are connected to the chip with polyethelyne tubing, and outlet valves allow aspiration of gas bubbles that may form in the media channels during thermal equilibration (Figure 12B). For the HTD, media reservoirs are etched glass, and medium is supplied by a syringe pump (Figure 12D). Both of the systems are designed so that all components fit on a petri dish for easy transportation to and from the incubator. These devices are easily fabricated; total fabrication, sterilization, and surface treatment time for each set of devices is less than 3 days, including all incubation periods, and the number of devices in a set is limited only by the size of a silicon wafer. Typically 4-6 devices are made at a time.
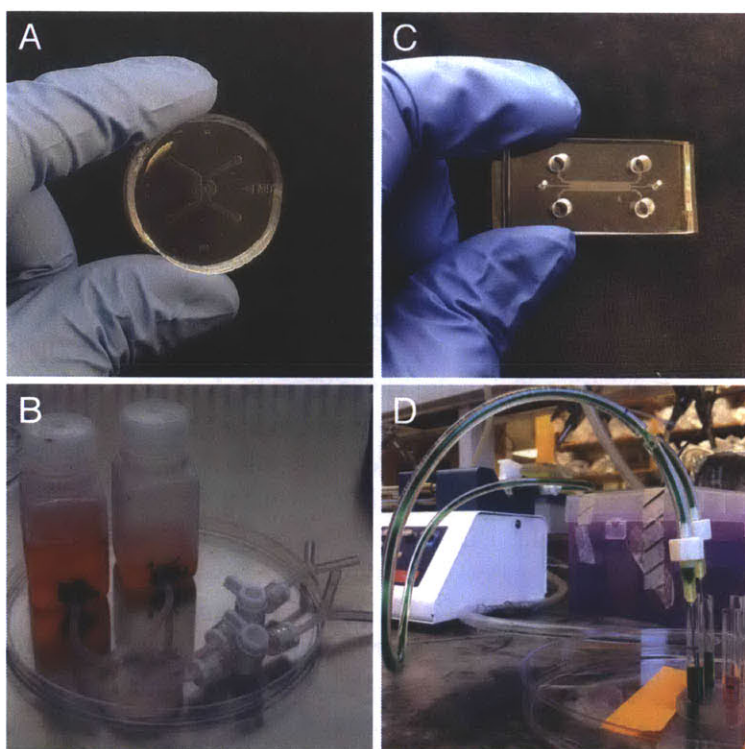
Figure 12. Microfluidic systems for applying interstitial flow. A) The microinjection device contains a small central gel region, and is small enough to fit in a standard well of a 6-well plate. B) Flow is applied by attaching external reservoirs. Reservoirs with large surface area are used to minimize pressure head loss with flow. C) The HTD contains a gel region that is >4x the size of the microinjection device gel region to allow more data collection per device. D) Flow is applied by attaching glass reservoirs to the device, and needles connected to a syringe pump (green tubing) are used to introduce flow (downstream medium indicated in pink).

2.3 Cell and device preparation

Microfluidic devices were fabricated using soft lithography in a process that has been described previously (156). Polydimethylsiloxane (PDMS, Ellsworth Adhesives, MA) was mixed at 10:1 base: curing agent, poured over a silicon master, and incubated overnight at 80°C. The PDMS was cut from the silicon master, trimmed, and autoclaved in water. The devices were then dry autoclaved and dried overnight in an oven at 80°C. The sterile microinjection devices were then surface activated by plasma treatment for 4min, (Harrick Plasma, Ithaca, NY), coated with Poly-D-lysine (PDL, Sigma-Aldrich, St. Louis, MO) incubated overnight at 37°C, washed with sterile water, and dried overnight at 80°C. HTD devices were plasma treated for 4min along with a sterile coverslip, bonded after treatment, and PDL was injected into each device. The devices were incubated overnight at 37°C, washed with sterile water, and dried overnight at 80°C.

MDA-MB-231 cells originally derived from a pleural effusion were obtained from the American Type Culture Collection (Manassas, VA) and were cultured in standard growth media of 10x DMEM (Invitrogen, Carlsbad, CA) with 10% FBS (Invitrogen). Prior to seeding devices with collagen gel and cells, microinjection devices and a sterile coverslip for each device were plasma treated for 4min in order to ensure a strong bond between the PDMS and coverslip when the device is sealed. Collagen type I (BD Biosciences, Bedford, MA) solution was buffered with 10x DMEM, titrated to a pH of 8.3-8.9 with NaOH, and brought to a final concentration of 2mg/ml collagen I in total solution. Cells were harvested with 0.05% Trypsin/EDTA and centrifuged at 12000RPM for 5min. The cells were re-suspended in media at the desired concentration, and the suspended cells were then mixed with collagen I solution to make a final cell density of 6.0×10^5, 2.5×10^5, or 0.5×10^5 cells/(ml total solution). The gel-cell solution was added to microinjection devices by hand using a micropipette, and devices were sealed with a coverslip. In order to ensure a tight seal between the PDMS and the coverslip, the gel must be added to the device and the device must be sealed with the coverslip within 30min of plasma treating the device and coverslip. For the HTDs, devices are already bound to coverslips, so the gel-cell solution is injected directly in the gel filling port. The seeded devices were placed in an incubator at 37°C for 30min to allow the collagen gel to polymerize before adding media via the surface ports, at a rate slow enough so as not to disrupt the collagen gel. In order to add media without disrupting the gel, it was important to avoid forming a seal between the pipette tip and media port in the device, as pressure used to eject media from the pipette could rupture the gel. A small radius pipette tip (or gel filling tip) was used to wet the glass coverslip at the bottom of the media port, and surface tension drove the media through the media channels on either side of the gel region.

2.4 Establishing interstitial flow

Cells were incubated overnight at 37°C and 5% CO_2. To apply a pressure gradient, external media reservoirs were connected to the microfluidic chip. Note: it is critical to avoid conical reservoirs for reliable flow rates (see appendix). For the microinjection device, the reservoirs were made from modified Nalgene (Thermo Fisher Scientific,

Waltham, MA) bottles with Tygon (Compagnie de Saint-Gobain, Paris, France) tubing to connect the reservoirs to the device. Medium was added to each reservoir at volumes that established the desired pressure gradient across the gel, and large reservoirs ($12.5cm^2$ cross sectional area) were employed so that volume changes due to interstitial flow were less than 0.5% relative to reservoir volume during the course of a 12hr experiment for $3\mu m/s$ flow. Devices were allowed to reach thermal equilibrium at 37°C before imaging. Valves were added to allow aspiration of bubbles that may form during thermal equilibration, and to prevent media leaking during flow.

For the HTD, glass reservoirs (2mm internal diameter) were cleaned and etched with HCl overnight before being washed with sterile water and autoclaved. Because of the gel filling ports that are used to inject collagen gel into the device (156) are open to the atmosphere, they must be covered with glass during an experiment to avoid local evaporation and bubble formation. Tygon tubing was connected to syringe needles inserted into the glass reservoirs. For very short-term experiments (< 4 hrs), clear polycarbonate single-barbed tube fittings (5/32" inner diameter) with cylindrical cross-section (McMaster Carr, Elmhurst, IL) were press-fitted into 4mm diameter ports punched into the microfluidic device. Flow was established, and pressure head was restored every 20min to avoid significant decays in flow velocity. For short-term experiments (< 12hrs), upstream reservoirs were connected to a syringe pump to add medium at an appropriate flow rate (see appendix). Cylindrical glass tubing (6mm outer diameter, Chemglass, Vineland, NJ) was press-fitted into 6mm diameter ports punched into microfluidic device. Tygon tubing fitted with luer lock adapters were connected to syringe needles, which were placed inside of glass tubing Figure 12D). Tubing was then connected to a 3mL syringe and added to a syringe pump for volumetric control of IF flow rate (see appendix). For long-term experiments, a second syringe pump was used to remove medium from downstream reservoirs at the same flow rate as pumped into the upstream reservoirs.

2.5 Imaging and image processing

Phase contrast images were taken every 15min for 16-24hrs in an environmental chamber held at 37°C and 5% CO_2. After imaging, 200nm diameter fluorescent microspheres (Polysciences, Warrington, PA) were added to the media, and fluorescent images were taken to ensure pressure head establishment and flow had not induced gel rupture.

An FEM model was developed in Comsol Multiphysics (COMSOL, Stockholm, Sweden) using an imported Auto-CAD file (Autodesk, CA) of the device geometry. The model determine the fluid velocity vector field by solving Brinkman's equation for flow through a porous media (Equation 1, 12):

$$\mu\nabla^2\underline{v} - \frac{1}{K}\underline{v} - \nabla P = 0$$

Equation 1: Brinkman's equation

35

Where μ is the viscosity of water, K is the permeability, and P is the pressure drop. The model solved Brinkman's equation for the full 3D geometry of the device in steady state. The permeability was determined experimentally (see Results) and assumed to be constant throughout the region of device with collagen gel. The pressure drop was determined for each experiment by measuring the hydrostatic pressure difference between the upstream and downstream reservoirs.

For cell alignment quantification, images at given time points were segmented using a previously described Matlab (The Math Works) script (172). Another in-house Matlab script fit an ellipse to each segmented cell, and the location of the centroid of each ellipse was passed to Comsol to determine the local flow velocity vector field. Subsequent vector analysis and quantification was performed using an in-house Matlab script.

For migration quantification, cells were tracked in time-lapse image sequences using the manual tracking plug-in for ImageJ (http://rsb.info.nih.gov/ij). An in-house Matlab script determined migration position and velocity vectors from the ImageJ output. The origin of the migration vectors was passed to Comsol to determine the local fluid velocity vector. Further vector analysis, including determining the angle between velocity and migration vectors, was performed in Matlab using an in-house script. Migration data for each cell in one device was averaged over the whole cell population (the number of cells in a population is subsequently denoted by m), and the average migration data for each cell population was averaged over multiple devices (indicated by n). Statistics were tabulated using a one-way analysis of variance (ANOVA).

To quantify the flow field, 200nm fluorescent microspheres were added to the cell media in the upstream reservoir. Microspheres were imaged using fluorescent time-lapse images. Images were binarized using ImageJ, and an automated tracking algorithm in IMARIS (Bitplane, St. Paul, MN) was used to track the beads in the binarized time-lapse images. An in-house Matlab script determined velocity vectors for each bead using the IMARIS output. The origin of each bead was passed to Comsol to determine the local velocity vector. Subsequent vector analysis was performed in Matlab.

2.6 System design and geometry

The geometry of each device allows time-lapse imaging to observe the dynamics of the live cell response (Figure 13). The microinjection system and the HTD consist of two channels separated by a region containing single cells suspended in collagen I gel. The device employs post structures to keep collagen gel confined to the center of the device (156). The region of interest (ROI) imaged during the experiments was the center of the gel region, and only cells located more than 20μm from the PDMS walls were imaged so edge effects could be neglected. The gel dimensions of the microinjection device ROI were approximately 1.25mm transverse to flow, 0.75mm in the direction of flow (does not include region between posts where flow rate is elevated due to reduced cross-sectional area) and 0.25mm in depth (Figure 13A). The gel dimensions for the HTD were approximately 14.5mm transverse to flow, 0.9mm in the direction of flow and 0.2mm in

depth (Figure 13B). For live cell experiments, sub-regions of 0.5mm by 0.5mm at one depth in the center of the device were imaged to observe the response of cells in 3D matrix. These regions contained approximately 10 cells at cell concentrations of 5×10^4 cells/ml, 50 cells at 25×10^4 cells/ml, and >100 cells at 60×10^4 cells/ml. By applying a hydrostatic pressure gradient across the gel region, a consistent flow field is generated.
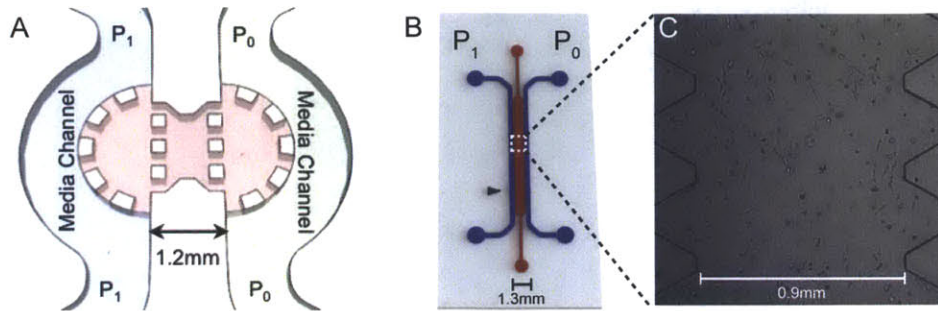
Figure 13. Microfluidic system for seeding cells and applying interstitial flow. A) For the microinjection device, cells are seeded in the central region, and the media channels are connected to external reservoirs to apply a hydrostatic pressure gradient. P1 ad P0 are pressures in the two channels with P1>P0 to generate flow through the gel. B) HTD implements gel injection ports (red) to introduce collagen gel after the device is bonded to glass coverslip. These ports must be covered with glass prior to establishing pressure gradient, which, like the microinjection device, involves hydrostatic pressure to drive fluid flow through the gel. C) Close up of region indicated in (B). Phase contrast demonstrates cells seeded at 60×10^4 cells/ml.

2.7 Interstitial flow field verification

We used FEM software (Comsol Multiphysics) to solve Brinkman's equation for flow through porous medium (173) for our system geometry (Figure 14). Pressure boundary conditions were applied at the inlet and outlet ports of the device. No slip boundary conditions were applied at all PDMS and coverslip surfaces, including central posts. We validated the flow field by adding fluorescent microspheres to the bulk fluid, and we imaged the microspheres using fluorescent time-lapse microscopy (Figure 14).
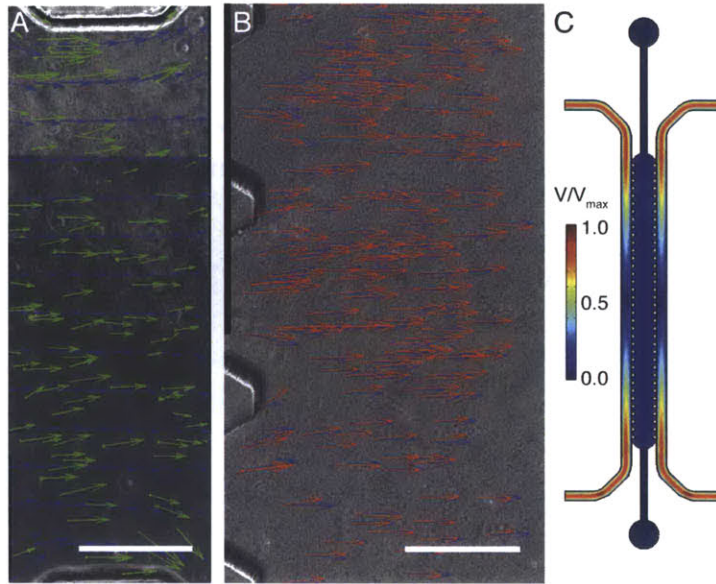
Figure 14. IF flow field verified by particle tracking technique A) Superimposed velocity vectors of 200nm diameter beads, output of FEM, and phase contrast image of the region of interest in the microinjection device. Green vectors indicate magnitude and direction of tracked beads, and blue vectors indicate local predicted magnitude and direction of the flow field from the FEM model (scale bar 0.25mm. B) Superimposed velocity vectors of 200nm beads, output of FEM, and phase contrast image of HTD. Velocity vectors of tracked beads in red, and computational vectors in red (scale bar 0.25mm). C) Output of FEM for full HTD demonstrates uniform flow velocity at center of gel region.

We found that the measured velocities were repeatable and agreed with the predicted velocities (Figure 15). In what follows, each flow field will be referred to by its respective nominal value, the rounded mean of 0.3μm/s, 3.0μm/s, 4.6μm/s respectively. Note that changes in cross sectional area due to device geometry are responsible for variations from the mean leading to an observable standard deviation in the model velocity magnitude and bead tracking magnitude. However, variation in the magnitude of the bead tracking velocity data is also due to thermal motion of the bead. The measured and predicted velocity vectors were co-directional (Figure 16). The average angle was calculated by averaging the local angle between the model and observed velocity vectors; quantifying the angle in this way allows variation in angle due to device geometry to be neglected. Furthermore, the angle was measured between 0 and 90° so that the average of a collection of randomly oriented vectors would be 45°. Consequently, the variation in angle from the mean leading to the standard error is due to a combination of thermal motion of the bead, nonunifomities in the gel, and experimental error. Cell responses at 3 different velocity magnitudes, 0.3μm/s, 3.0μm/s, and 4.6μm/s, were quantified to sample responses in the range of published *in vivo* values. From the bead tracking data, we determined the hydraulic permeability of 2mg/ml collagen I gel to be 1×10^{-13} m^2, which is similar to previously published values (15).

38
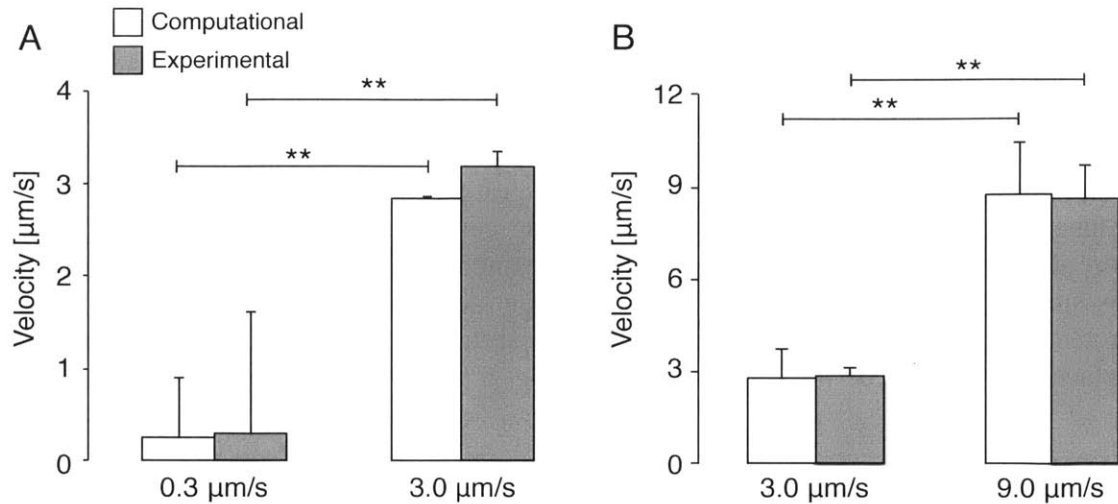
Figure 15. Magnitude of observed velocity and magnitude of velocity predicted by Brinkman's equation. A) Velocity magnitude for microinjection device. Nominal values are labeled on the x-axis. B) Velocity magnitude for HTD. Nominal values are labeled on x-axis (mean + S.D., **p<0.01 determined by ANOVA).
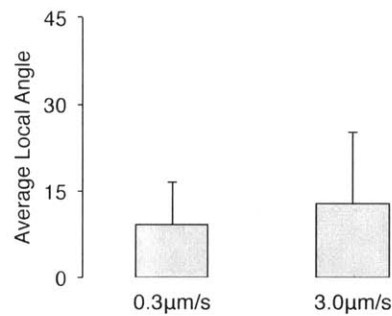
Figure 16. Average local deviation between the measured angle of the velocity vector and that predicted by the FEM (degrees). Y-axis maximum (45 deg) indicates average value for a random distribution of angles.

2.8 Measuring 3D cell migration within microfluidic devices

MDA-MB 231 human breast carcinoma cells were seeded in a collagen I gel in microfluidic devices as shown in Fig. 13. The cells were suspended in 3D, and when incubated with 10ng/ml hEGF supplemented growth medium, the cells migrated in 3D (**Figure 17**). To quantify the cell migration (Chapters 3 and 4), microfluidic devices were transferred to a microscope housed in a chamber that maintains 37°C and 5% CO_2. Images were taken every 15min for >8hrs, and cells were tracked in the resulting videos following the protocol described above. The cell migration tracks were further quantified to provide information on how various experimental conditions affect cell migration (**Figure 17**B-C). The cells degraded the collagen matrix as they migrated, leaving tracks in the gel during migration, thus suggesting a proteolytically active migration mechanism (

Over long periods of time, some cells migrate greater than 100µm (**Figure 17**), which could bring the cell into contact with the glass or PDMS substrates. Reflectance imaging allows visualization of these surfaces, and cells in contact with the stiff substrate are neglected, as we are interested in only cells migrating in 3D. When using phase contrast to take migration videos, however, determining cells in contact with glass or PDMS is more difficult. These cells tend to display a distinct morphology that is more spread and less spindle-like. Cells on 2D surfaces also migrate with much higher speed and lower directionality. Any cells that fit these criteria and are migrating along glass or PDMS surfaces are neglected.
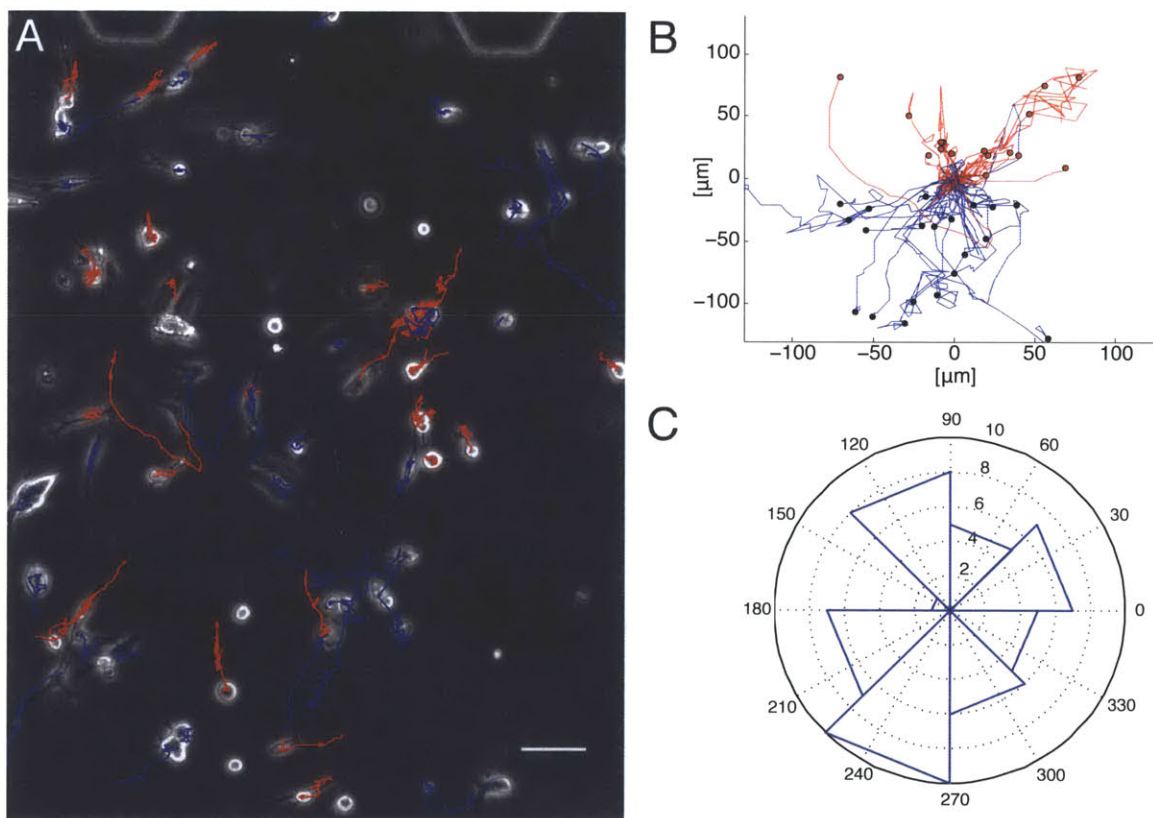
Figure 17. MDA-MB 231 cells migrated within microfluidic devices. A) Cells were tracked over 8hrs by taking phase contrast images every 15min. Migration tracks are superimposed on the image at t=0 to demonstrate a typical experiment (6×10^5 cells/ml). Tracks that resulted in net migration toward the top of the device are colored red, while tracks that migrated downward are colored blue to demonstrate the ability to discriminate between cells that migrate upstream or downstream when IF is applied (scale bar 70µm). B) Collapsing the tracks, so all trajectories start at (0,0) provides a method for visualizing patterns during cell migration. C) Polar histogram of the tracks shown in (A) and (B) demonstrates the number of cells migrating within in a given direction (radial axis is number of cells).

Figure 18. Superimposed confocal reflectance image of cells seeded in 3D collagen I matrix (blue) and confocal image of GFP expressing MDA-MB-231 cells (green). Gap behind cell (red arrow) shows cells migrate in 3D, degrading matrix during migration (scale bar 25μm).

2.9 Effect of interstitial flow on cell morphology

The microfluidic devices described above were implemented to investigate the effect of interstitial flow on tumor cell morphology. When exposed to interstitial flow, cells aligned parallel to flow streamlines (Figure 19). At longer times, cells extended protrusions and subsequently formed multi-cell strings in parallel with the flow streamlines (Figure 19B). Cell alignment was quantified by measuring the angle between the major axis of an ellipse fit to each cell and the local flow velocity vector from an FEM of the flow field. Each cell in a phase contrast image was fitted with an ellipse, and the centroid of the ellipse was passed to Comsol to determine the local fluid velocity vector at the respective location. The dot product between the velocity vector and the major axis of the ellipse was calculated as a measure of alignment. At longer times, after 48 h, cells extended protrusions and subsequently formed multicell strings in parallel with the flow streamlines; after 40 h, cells exposed to flow velocities of 3.0 μm/s aligned with the streamlines of the flow field with 86 ± 7% of cells aligned within 45° of the local streamline. Cells not exposed to flow remained randomly oriented with only 55 ± 2% of cells within 45° of the local streamline (Figure 20). The time required for alignment demonstrates that cells were actively responding to a stimulus from the flow and not simply being stretched by the pressure drop across the gel. Cell alignment with the flow streamlines is consistent with the work of Levesque and Nerem, who demonstrated that endothelial cells align in response to 2D shear flow (174).

41
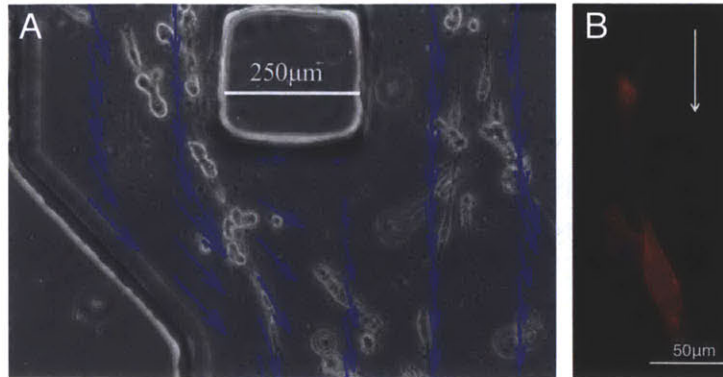
Figure 19. . Interstitial flow induces cell alignment to flow streamlines. B) Streamline vectors from FEM of flow in the device superimposed on a phase contrast image of cells exposed to flow (3μm/s for 12hrs). B) Fluorescent image of elongated cells demonstrates the formation of multicell strings after 24hrs (red – phalloidin, blue – DAPI, flow top to bottom 3μm/s for 24hrs).
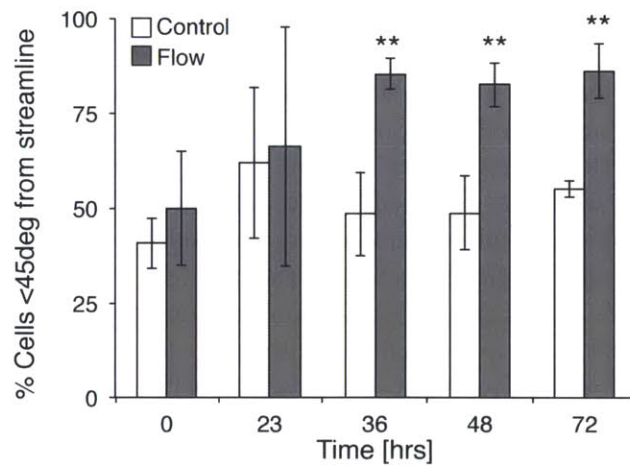
Figure 20. Angle of alignment was quantified by fitting an ellipse to each cell and plotting a vector from the centroid along the major axis of the ellipse. The dot product between the cell alignment vector and local streamline vector from an FEM was computed. Over time, a greater percentage of the cell population aligned to the streamlines (*$p < 0.05$; **$p < 0.01$ determined by ANOVA).

IF induced cell alignment to flow streamlines, and to determine whether flow influenced the elongation of cells, an elongation metric was developed. Elongation is measured as the ratio of the major axis to the minor axis of an ellipse fit to each cell. We then determined the percentage of a cell population elongated more than a threshold value of 2. Interstitial flow increased elongation of cells, but the increased elongation was not apparent until 72hrs after application of flow (Figure 21).
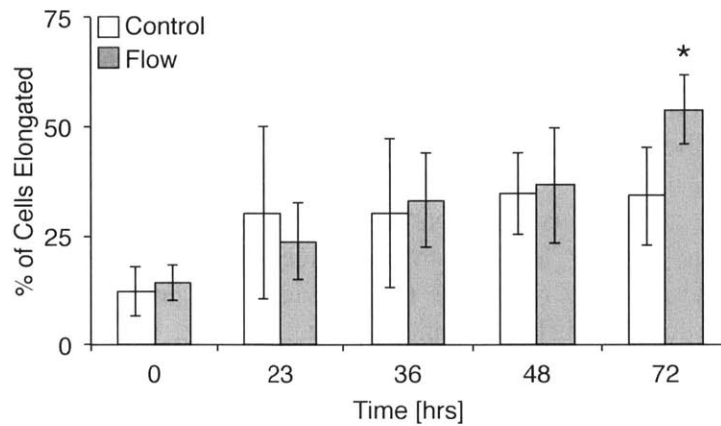
Figure 21. Effect of interstitial flow on cell morphology. Cells were considered elongated when the ratio of major axis to minor axis was greater than a threshold value of 2 (*p<0.05 determined by ANOVA).

Chapter 3: Effect of IF-induced autocrine gradients on tumor cell migration[*]

3.1 Introduction and autologous chemotaxis

Recent work has demonstrated that interstitial flow leads to CCR7 activation and can influence breast cancer cell migration even in the absence of lymphatic cells. Shields et al. developed a modified Boyden chamber assay to investigate the mechanism by which interstitial flow induces CCR7-dependent cell migration in breast cancer cell cultures. The authors observed increased metastatic potential in cell populations exposed to flow and demonstrated the increased metastatic potential was activated through binding of self-secreted CCL21 ligand to the CCR7 receptor (40). This autocrine signaling mechanism, called autologous chemotaxis, arises in a flow field where convection distributes autocrine factors leading to a pericellular concentration gradient, which provides a chemotactic signal (41). The magnitude of the pericellular autocrine gradient is governed by molecular diffusion and convection, and the non-dimensional Peclet number represents the ratio of convective to diffusive transport (Equation 2),

$$Pe = \frac{VL}{D}$$

Equation 2. Peclet number

where V is the magnitude of the fluid velocity, L is a characteristic length (for measuring Pe for pericellular transport, the cell diameter is used as the characteristic length), and D is the molecular diffusivity of the given molecule in the given medium. For Pe<<1, transport is diffusion dominated, and autocrine gradients will be insignificant as secreted ligand diffuses isotropically from the cell surface (Figure 22A). For Pe>>1, transport is convection dominated, and autocrine chemokines are washed downstream. There exists an intermediate region, for Pe ~ 1, where transport is neither diffusion dominated nor convection dominated. In this transport regime, diffusion transports the chemokine radially outward from the cell and convection transports chemokine downstream at a rate that allows for the chemokine to bind to cell surface receptors (Figure 22C). Competing convection and diffusion causes the autocrine chemokine to be highly concentrated at the downstream surface of the cell, and less concentrated at the upstream surface of the cell. This pericellular gradient in chemokine concentration results in higher receptor ligation at the downstream side of the cell, and this differential in receptor binding can lead to chemotaxis downstream (Figure 22D, 41).

---

[*] Sections of this chapter have been published previously. See (48).
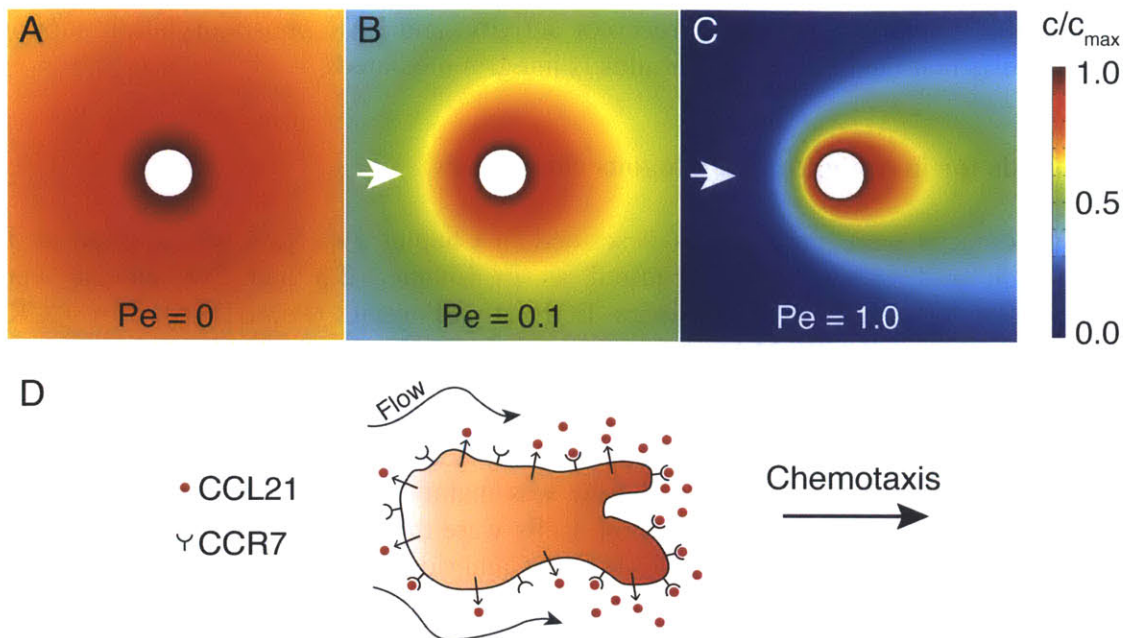
Figure 22. Peclet # dependence of autocrine gradients for cells exposed to IF. A) In the absence of IF, chemokine secreted by the cell (white) diffuse radially outward. B) With the introduction of flow, chemokine is washed downstream, but no significant gradient develops. C) At higher Pe #'s, when convection increases, more chemokine is washed downstream. D) At higher Pe #'s, IF can induce gradients in ligated CCR7 receptors even if the cell is uniformly secreting CCL21. This differential in CCR7 ligation can induce chemotaxis downstream (A-C simulation results for FEM assuming no slip and constant flux boundary condition at cell surface, with uniform flow at the inlet and neutral boundary condition at the outlet, while symmetry was assumed at the lateral boundaries. Only 1/5 of computational domain is shown).

Computational modeling confirms Pe-dependent pericellular autocrine chemokine gradients can arise with physiologically relevant IF flow velocities; however, the simulations have been limited to modeling single cells suspended in homogenous ECM (41). Presumably the magnitude and profile of autocrine gradients are a function of cell density, and as the cell density increases, the assumption that the pericellular autocrine gradient is independent of paracrine gradients becomes less valid. We employed the microfluidic system described in Chapter 2 to examine the effects of interstitial flow on cancer cell morphology and migration and to further investigate autologous chemotaxis via CCL21 and CCR7.

Consistent with this previous study, we found that cells migrated along streamlines in the presence of flow; however, we further demonstrated that the strength of the flow field as well as the cell density determined directional bias of migration along the streamline. In particular, we found that cells either at high seeding density or with the CCR-7 receptor inhibited migrate against, rather than with the flow. We provide further evidence that CCR7-dependent autologous chemotaxis is the mechanism that leads to migration with the flow, but also demonstrate a competing CCR7-independent mechanism that causes migration against the flow. Data from experiments investigating the effects of cell

concentration, interstitial flow rate, receptor activity, and FAK phosphorylation support our hypothesis that the competing stimulus is integrin mediated.

3.2 Methods for investigating autologous chemotaxis

Cells and devices were prepared as described in Chapter 2.4, flow was applied as in Chapter 2.5, and images were acquired as in Chapter 2.6 and 2.9. Media were supplemented with human recombinant EGF at 10 ng/mL (PeproTech). For CCR7 blocking, anti-human CCR7 MAb (R&D Systems) was added to the media at 5 µg/mL.

For immunofluorescent staining to measure FAK activation, cells were exposed to flow as described above for 1hr, before media was replaced with 4% PFA to fix the cells. During fixation, the pressure head and flow was maintained in experimental devices to preserve protein expression and activation. Cells were then permeabilized and incubated with mouse anti-human FAK MAb (Abcam, Cambridge, MA) and rabbit anti-human PAb FAK(Y397) (Abcam). Cells were subsequently imaged with a confocal laser-scanning microscope, and laser power and signal gains were maintain at constant level among all devices. The total intensity of FAK(Y397) was normalized to intensity of FAK for pixels co-localized to GFP for each cell. Inter-device variability for each condition was not significant.

3.3 Effect of cell density on directional migration in response to IF

Using time-lapse imaging over 16hr intervals, the center of mass of each cell was tracked 24hrs after seeding and 4hrs after applying interstitial flow (Figure 17, Figure 23). Interstitial flow did not have a significant effect on cell migration speed, defined as total migration distance over a given time (Figure 24A). Directionality, also referred to as directional persistence, is a measure of how straight a cell migrates and has been used previously to demonstrate the effect of chemokines on cell migration behavior (175). Directionality is defined as the net migration distance normalized by the total migration distance, and cells exposed to interstitial flow migrated with increased directionality (0.63±0.073 for 0.3µm/s, 0.61±0.071 for 3.0µm/s, compared to 0.39±0.071 for control, Figure 24B). Cell motility, another metric used to quantify cell response to chemokines, is defined as the percentage of cells migrating a distance greater than one cell diameter and was unaffected by flow (Figure 24C). In other words, interstitial flow does not affect the percentage of the cell population that migrates or the speed at which the cells migrate, but migrating cells exposed to interstitial flow will migrate a larger net distance in a given time.
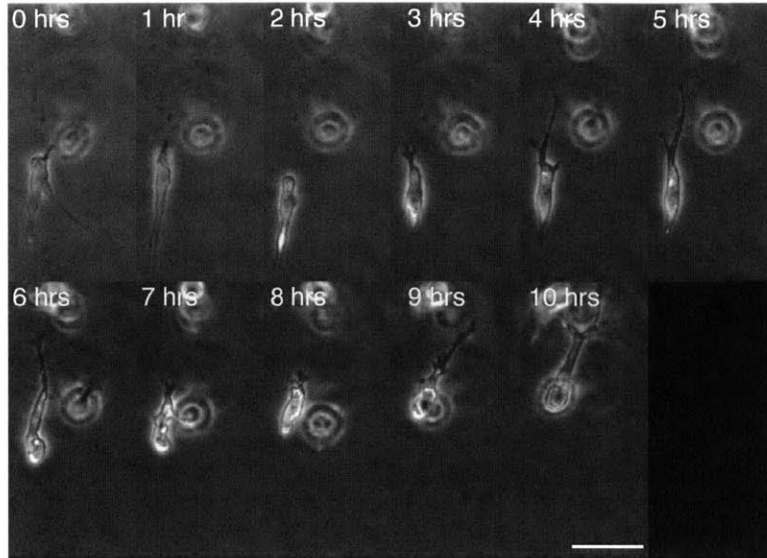
Figure 23. Interstitial flow influences direction of cell migration. Sample time-lapse images of a cell migrating in an interstitial flow field. Flow is 3.0 μm/s from top to bottom in the image.
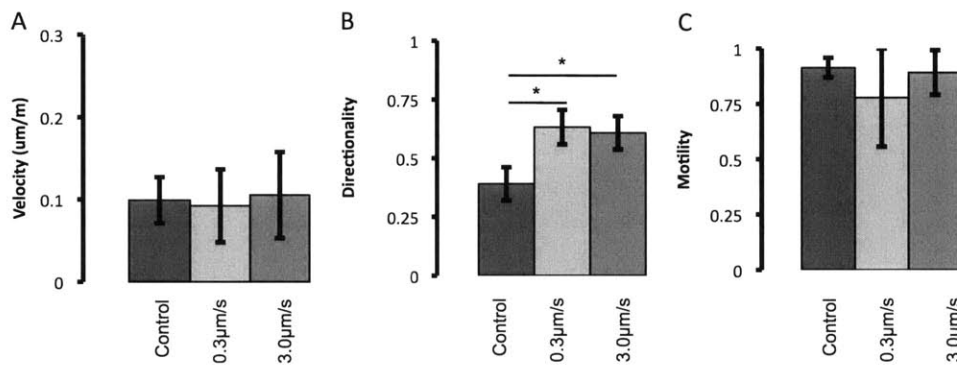
Figure 24. (A–C) Interstital flow affects cell migration. Although flow had no affect on migration velocity or cell population motility, it significantly increased the directionality of migrating cells (*p < 0.05).

Interstitial flow induced a directional bias in cellular migration. Polar histograms of migration data for a control device and a device with 3.0μm/s flow clearly demonstrate the effect of flow on the direction of migration vectors (Figure 25). In devices with flow, cells preferentially migrated along streamlines. To quantify the migration direction of cell populations, two metrics are presented. The "streamline migration metric" scores cells with a +1 if they migrate within 45° of a streamline and a −1 if they migrate outside of this zone (Figure 25C). An average score for a cell population of +1 indicates that all of the cells are migrating along a streamline, a score of 0 corresponds to purely random migration, and score of −1 indicates that all cells are migrating perpendicular to the streamline. To determine directional bias of migration along streamlines, a "directional migration metric" was computed that scored cells with a +1 if they migrated within 45° of a streamline in the downstream direction (subsequently denoted "with the flow") and a −1 if they migrated within 45° of a streamline in the upstream direction (subsequently denoted "against the flow") (Figure 25D). A population has an average score of +1 if all of the cells migrating within 45° of a streamline are migrating with the flow, a score of −1 if all of the cells are migrating against the flow, and a score of 0 if equal numbers of cells are migrating with and against the flow.
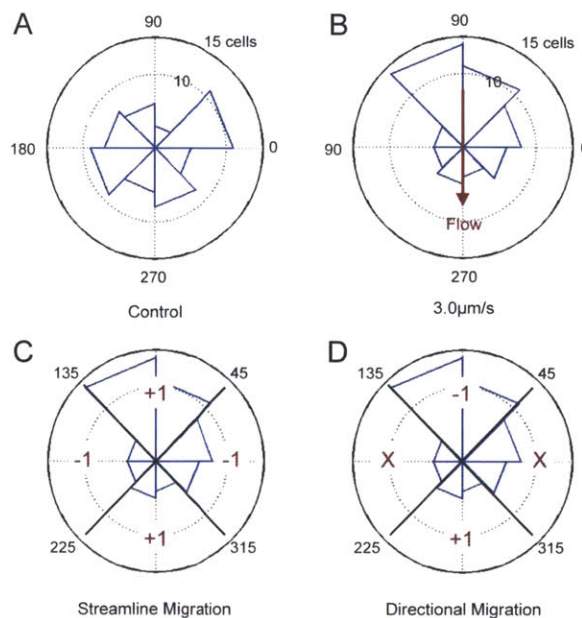
Figure 25. Interstitial flow influences direction of cell migration. A) Sample data from one control device. The polar histogram demonstrates distribution of angles of net migration vectors for cells in a population in one device. Cells in control devices without flow migrate randomly. B) Flow changes the distribution of migration vector angles. In this sample data from one device, cell migration bias, are against the flow. To quantify directional bias in cell migration, two metrics were computed: C) The streamline migration metric is a measure of migration bias along the streamlines, and D) the directional migration metric is a measure of the upstream or downstream migration bias for cells migrating along streamlines. "X" indicates that cells not migrating along streamlines are not scored for the directional migration metric.

Cells seeded at 25×10^4 cells/ml and exposed to interstitial flow preferentially migrated along the flow streamlines, with average streamline migration scores of 0.47 ± 0.06 for 0.3μm/s and 0.24 ± 0.04 for 3.0μm/s (mean ± STD, Figure 26A). Of the cells migrating along the streamline, a greater fraction of the cell population migrated upstream than downstream and the strength of this upstream bias was a function of interstitial flow rate (these results were not due to EGF gradients within the device, see Appendix). At an interstitial flow speed of 0.3μm/s, the average directional migration score was -0.18 ± 0.15, and at 3.0μm/s directional bias increased further to -0.40 ± 0.08. Cells in control devices did not preferentially migrate in either direction (Figure 26B). These results were opposite to those reported by Shields et al. (40) who had observed cells to preferentially migrate with the flow.
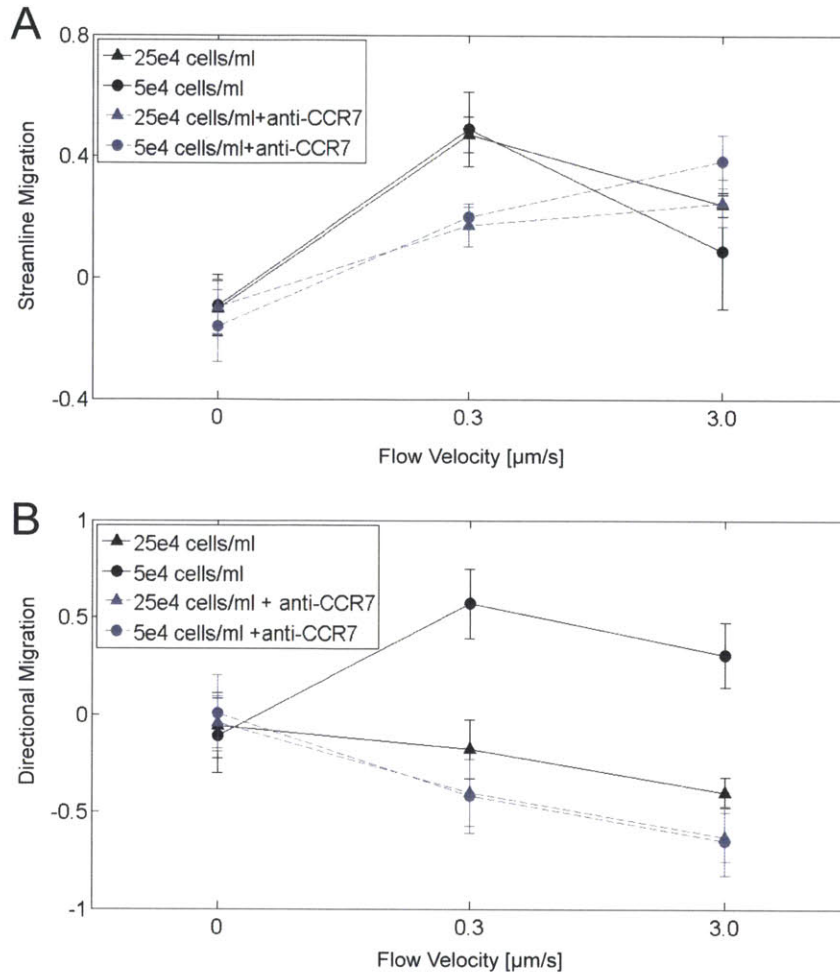
Figure 26. Interstitial flow induces a bias in direction of tumor cell migration. "High" and "low" refer to seeding densities of 25×10^4 cells/mL and 5×10^4 cells/mL, respectively. (A) Streamline migration (see Fig. 2D for definition) measures the bias in migration along streamlines of a cell population. Cells exposed to interstitial flow preferentially migrated along streamlines, and this bias is a function of flow rate, cell density, and CCR7 receptor activity. Blocking CCR7 in a 0.3-μm/s flow field causes a significant decrease in streamline migration score (P < 0.01). In a 3.0-μm/s flow field, blocking CCR7 has the opposite effect of increasing streamline migration score, but only at a low cell density (P < 0.05). (B) Directional migration (see Fig. 2E for definition) demonstrates directional bias of cells migrating along the streamline, positive directional migration indicates downstream migration, and positive streamline migration indicates cells are preferentially migrating along the streamline. Cells exposed to interstitial flow preferentially migrated upstream or downstream as a function of flow rate, cell density, and CCR7 receptor activity. Directional migration scores become more negative with increasing flow velocity. With active CCR7, increasing cell density reverses directional bias from downstream to upstream (P < 0.01 for both flow rates), but when CCR7 is blocked, directional migration scores are more negative and do not depend on cell density. (Mean ± SD was computed by averaging the score for each cell in one device (n > 15) and averaging the score for three devices at each condition.)

In order to test for the effect of cell density on directional migration under flow, experiments were conducted at two different seeding densities, 25×10^4 and 5×10^4 cells/ml. Decreasing cell concentration did not affect the bias for migration along streamlines in a 0.3µm/s interstitial flow field, although a smaller percentage of cells migrated along streamlines in a 3.0µm/s interstitial field when seeded at a lower concentration (Figure 26A), nor did decreasing cell density influence cell migration speed, motility, or directionality (Figure 27).
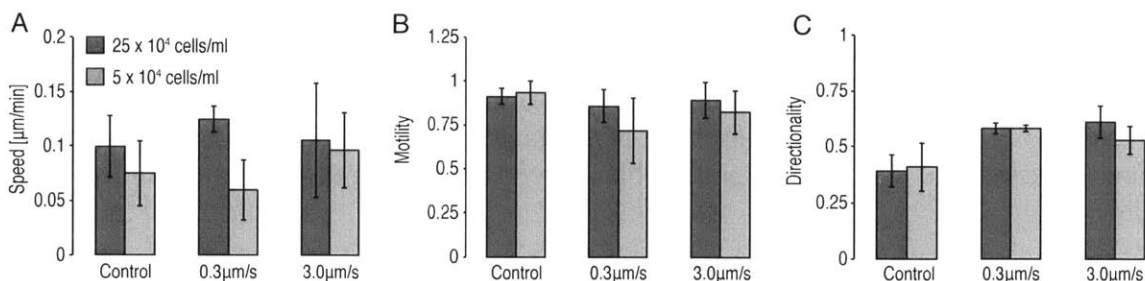
Figure 27. Cell density does not have a significant effect on cell speed, motility, or directionality.

Decreasing cell density did, however, exert a dramatic effect on the direction of migration, causing a reversal in the directional bias of migration relative to the flow as indicated by the sign change in the directional migration metric, a result consistent with Shields et al. (40). At a flow speed of 0.3µm/s, the average directional migration score was -0.177 ± 0.15 at 25×10^4 cells/ml but increased to 0.570 ± 0.18 at 5×10^4 cells/ml. For 3.0µm/s, the average directional migration score was -0.401 ± 0.08 at 25×10^4 cells/ml but increased to 0.307 ± 0.16 at 5×10^4 cells/ml (Figure 26B).

3.4 Effect of blocking CCR7 on directional cell migration in response to IF

In devices seeded at 25×10^4 cells/ml and subject to 0.3µm/s interstitial flow, addition of CCR7 blocking antibody reduced the bias of migration along streamlines, lowering the average streamline migration metric from 0.472 ± 0.060 to 0.174 ± 0.070, but had little effect on cells in a 3.0µm/s flow field (Figure 26A), and blocking had little effect on migration speed, motility, and directionality (Figure 28A-C). At both interstitial flow velocities, blocking CCR7 increased directional migration *against* the flow (Figure 26B).

Interestingly, the combined effect of decreasing cell density and blocking CCR7 resulted in a flow-rate dependent change in migration bias along streamlines. At 0.3µm/s, the streamline migration score was reduced from 0.489 ± 0.122 to 0.201 ± 0.031 with the addition of CCR7 blocking antibody at 5×10^4 cells/ml; however, at 3.0 µm/s, the streamline migration score increased from 0.088 ± 0.188 to 0.384 ± 0.06 at 5×10^4 cells/ml (Figure 26A), and there was little effect on cell migration speed, motility, or directionality (Figure 28D-F).

In devices seeded at 5×10^4 cells/ml, addition of anti-CCR7 blocking antibody completely negated preferential migration in the direction of flow and in fact, caused preferential migration against the flow. The average directional migration score dramatically decreased at both flow velocities, from 0.570 ± 0.12 to -0.420 ± 0.19 at 0.3µm/s and from 0.307 ± 0.16 to -0.649 ± 0.18 at 3.0µm/s (Figure 26B).

When comparing cell populations at 5×10^4 cells/ml with CCR7 blocking antibody and populations at 25×10^4 cells/ml with CCR7 blocking antibody, there are no significant differences in directional migration bias. These data suggest that addition of the blocking antibody negates the effect of cell concentration on directional migration bias. Furthermore, although the effects are not statistically significant, a consistent trend is observed in the effect of flow rate. At both cell concentrations, increasing the flow rate from 0.3µm/s to 3.0µm/s increases the percentage of cells migrating along the streamline and increases the upstream migration bias of cells migrating along the streamline (Figure 26).
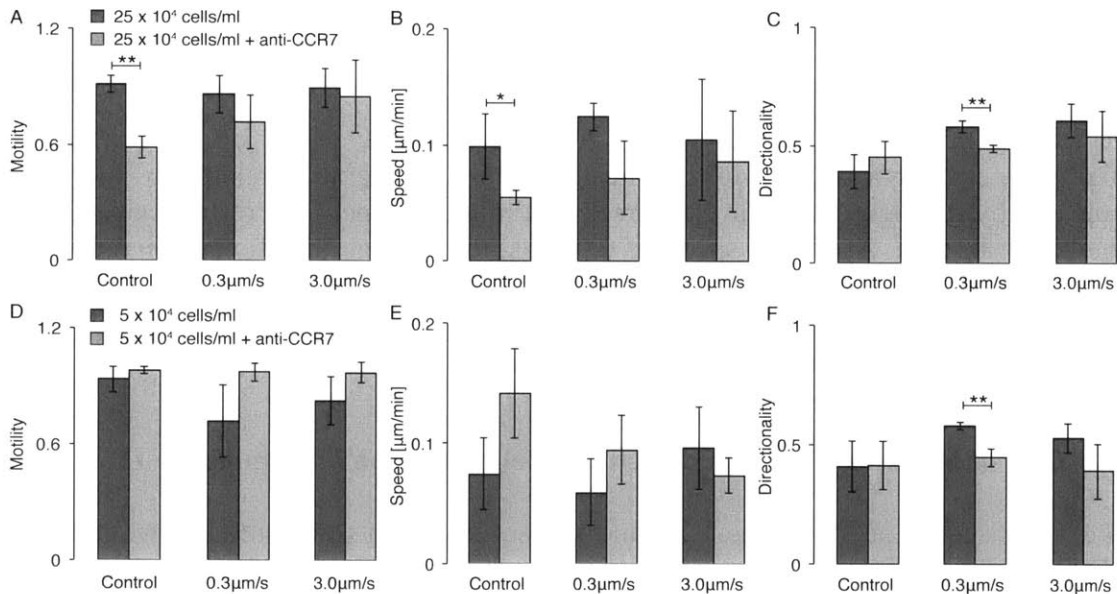
Figure 28. Blocking CCR7 has little effect on motility, speed, or directionality for both cell densities. A-B) Blocking CCR7 reduces motility and speed, though these effects are not significant when cells are exposed to flow. C) Blocking CCR7 reduces directionality at lower flow rates. D-E) Blocking CCR7 at lower cell densities does not influence motility and speed, though the trends are reversed from higher cell density. E) Effect of blocking CCR7 similar to the effect at higher cell density.

3.5 Interstitial flow increases focal adhesion kinase (FAK) activation.

In devices seeded at 25×10^4 cells/ml, cells exposed to 3.0μm/s flow demonstrated increased phosphorylation at Tyr-397 in FAK, which is associated with focal adhesion formation and Src kinase activation (120,176). The relative activation of FAK was determined by measuring the intensity of immunofluorescent staining for FAK and *p*-FAK(Y397) in control devices and in devices exposed to 3.0μm/s flow, and cells exposed to flow demonstrated a significant increase in *p*-FAK(Y397) intensity (Figure 29). High magnification confocal images demonstrate that *p*-FAK(Y397) is localized to the cell membrane (Figure 30). Furthermore, there is an upstream bias of *p*-FAK(Y397), which will be discussed further in Chapter 4. That flow results in increased FAK phosphorylation is consistent with data from experiments in which we blocked Src kinase by introducing specific inhibitor of Src kinase PP2 (177). We found that blocking Src kinase activity resulted in decreased upstream migration, and cells migrated randomly, with no biased migration upstream or downstream (Figure 31).
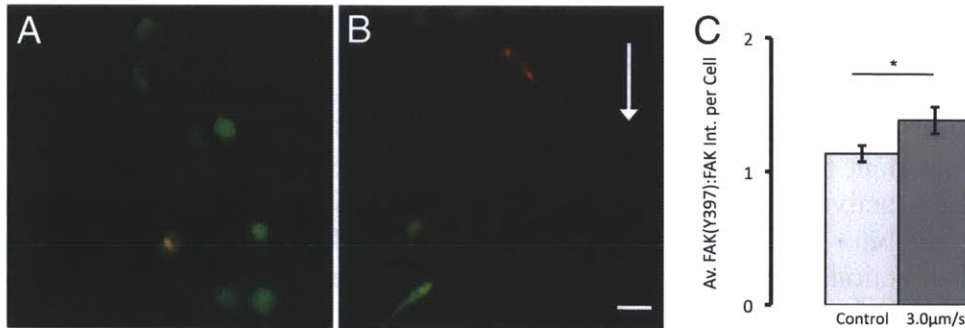
Figure 29. Interstitial flow induces FAK phosphorylation. (A and B) Overlay of GFP in green and p-FAK(Y397) in red for projected confocal z-stacks of (A) a representative control device and (B) a representative device with 3.0 μm/s flow. Flow direction is from the top to the bottom of the image. Although each cell population demonstrated heterogeneity in FAK phosphorylation, on average, cells exposed to interstitial flow demonstrated increased FAK activation. (C) Normalized intensity ratio of p-FAK(Y397) to FAK per cell demonstrates increased FAK phosphorylation in cells exposed to flow. (Scale bar, 30 μm.) Mean ± SEM was computed by averaging total intensity of p-FAK(Y397) to FAK staining for n > 50 cells in three devices for each condition (*p < 0.05 determined by ANOVA).
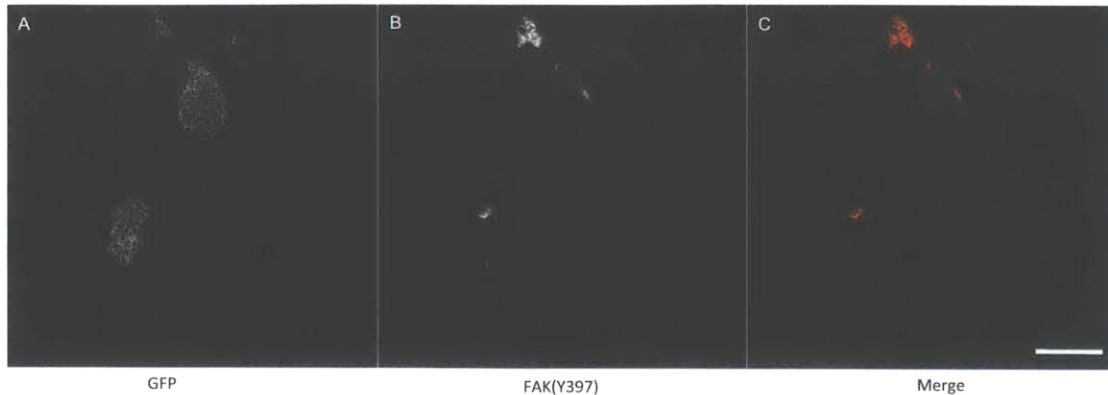
Figure 30. FAK phosphorylation is localized to the cell membrane. (A–C) GFP (A), FAK(Y397) (B), and overlay of GFP in green and FAK(Y397) in red (C) for a single z-slice of cells exposed to 3.0 μm/s flow. Flow is from top to bottom of image. (Scale bar, 10 μm.)

3.6 Effect of Src kinase inhibition on cell migration.

It has been shown that FAK activates Src kinase (178,179), which modulates traction forces important for tumor cell migration (180,181). To examine the role of shear stress induced FA activation on migration in the presence interstitial flow, we introduced the specific inhibitor of Src kinase PP2 (65). We found that inactivation of Src kinase blocked directional migration of cells exposed to interstitial flow. For cells seeded at 25×10^4 cells/ml, the streamline migration score was not significantly different from 0 for control, 0.3μm/s, and 3.0μm/s applied flow (Figure 31A). Furthermore, the directional migration scores at 0.3μm/s and 3.0μm/s applied flow did not vary significantly from control (Figure 31B). Cell migration velocity was unchanged with the addition of PP2, but cell migration was randomly directed, suggesting that Src kinase is involved with directional sensing for cells exposed to interstitial flow.

These data are consistent with the CCR7-mediated autologous chemotaxis model for downstream migration since Src has been implicated in the CCR7 pathway in lymphocytes (76,182). Since PP2 blocked upstream migration as well, Src is also apparently involved in upstream migration; furthermore, upstream migration is independent of cell density, so paracrine and autocrine signaling through chemokine receptors are unlikely stimuli for Src activation. Consequently, the PP2 data support our hypothesis that flow induced stress gradients and directed proteolysis lead to directional bias in integrin activation, FA formation, and subsequent Src activation, stimulating migration against the flow.
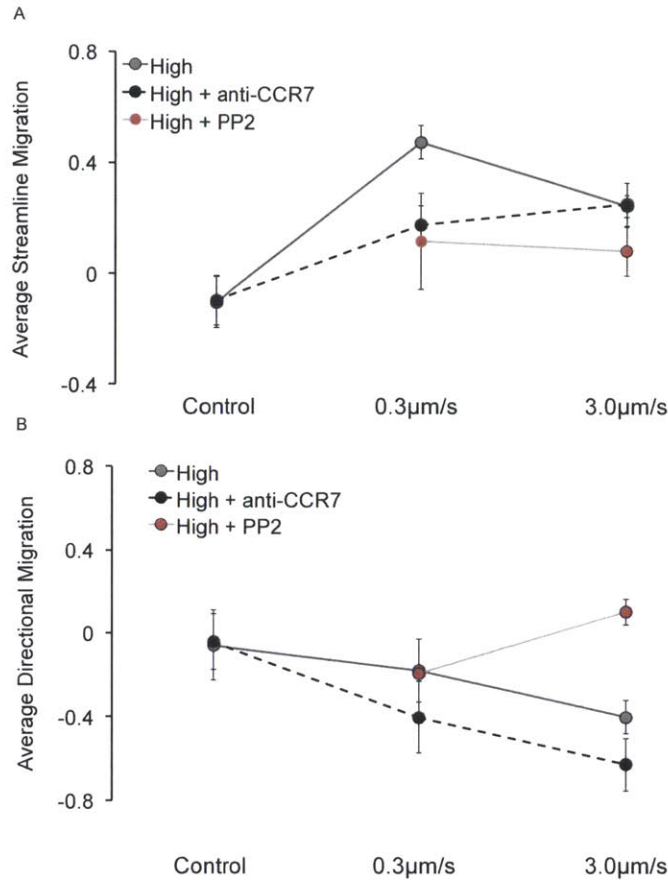
Figure 31. Addition of specific inhibitor of Src kinase. PP2 blocked directional migration of cells exposed to interstitial flow. (A) In devices at both flow rates, streamline migration scores were not different from 0. (B) The directional migration score did not vary from control for both flow rates with the addition of PP2 (Mean ± SD was computed by averaging the score for each cell in one device (n > 15) and averaging the score for three devices at each condition).

3.7 IF influences direction of fibrosarcoma cell migration

To investigate the generality of the mechanism, we repeated the flow experiments with HT1080 fibrosarcoma cells. When seeded at 25×10^4 cells/ml and exposed to 3 μm/s flow, HT1080s migrate at nearly 3x speed of the MDA-MB 231 (mean speed 0.298 μm/min compared to 0.105 μm/min), while directionality was similar between the two cell types (0.556 for HT1080, 0.608 for MDA 231). Importantly, the HT1080 cells migrated upstream in response to 3 μm/s flow (Figure 32), though the upstream migration was slightly attenuated when compared to the MDA-MB 231 data (directional migration metric 0.25 for HT1080, and 0.4 for MDA-MB 231).
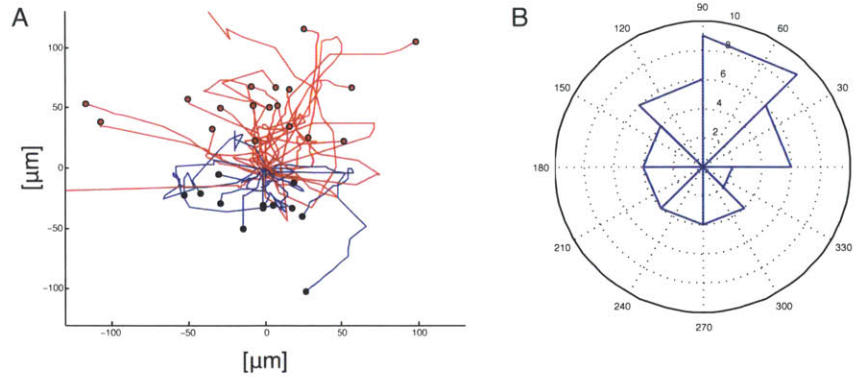
Figure 32. Migration behavior for HT1080. A) Migration tracks for HT1080 cells in response to 33 μm/s flow from top to bottom. Tracks with net upstream displacement are labeled in red, while those with net downstream displacement are in blue. Cells were tracked over 12hrs. B) Polar histogram demonstrates upstream migration behavior by HT1080s.

3.8 Model for transcellular autocrine morphogen gradient for multi-cell population.

The effect of interstitial flow on autologous morphogen gradients has been previously studied in the context of autologous chemotaxis (41), but the computational model presented considers only one cell in the presence of a flow field. Our results on the effect of interstitial flow on direction of cell migration demonstrate that migration bias in a cell population is a function of cell density, and we hypothesize that the cell density dependence was the result of the interaction between morphogen fields among neighboring cells.

To determine the effects of cell concentration on autocrine gradients in an interstitial flow field, a coupled mass and momentum transport FEM model was developed in COMSOL. The geometry used to model cells in a porous matrix consisted of 5 cells, with each cell modeled as a sphere with radius of 10μm, and the distance between each cell center was 20μm (Figure 33). Brinkman's equation (Equation 1)(173) was solved for the given geometry. No-slip boundary conditions were applied at the cell walls, and zero normal velocity was imposed between cells at the lateral boundary. The inlet velocity was fixed at 3.0μm/s to match experimental conditions, and the permeability was determined experimentally (see Chapter 2).

The velocity field determined from Brinkman's equation was then used to solve the diffusion equation:

$$\frac{dC}{dt} + \nabla \cdot N - R = 0$$
$$N = -D\nabla C + v \cdot C$$

Equation 3. Diffusion equation

Where C is the concentration of morphogen, N is the molar flux, v is the velocity determined from Brinkman's equation, D is the diffusivity of the morphogen in the given medium, and R accounts for addition or consumption of the morphogen due to reaction. The diffusivity for CCL21 in water was used (41), and a variety of reaction rates were considered. Constant flux boundary conditions were imposed at cell surfaces, no flux boundary conditions were imposed at the lateral symmetric boundary between cells, zero concentration boundary condition was imposed at the inlet, and a zero diffusive flux boundary condition was imposed at the outlet. Steady state was assumed as we intended to model the concentration field at long times. The resulting morphogen concentration fields were exported to Matlab for further analysis of pericellular concentration gradients. We varied reaction rate from 0 to $-0.2s^{-1} \times C$ (41) and observed that increased cell density decreased the relative magnitude of chemokine gradients for these reaction rates.
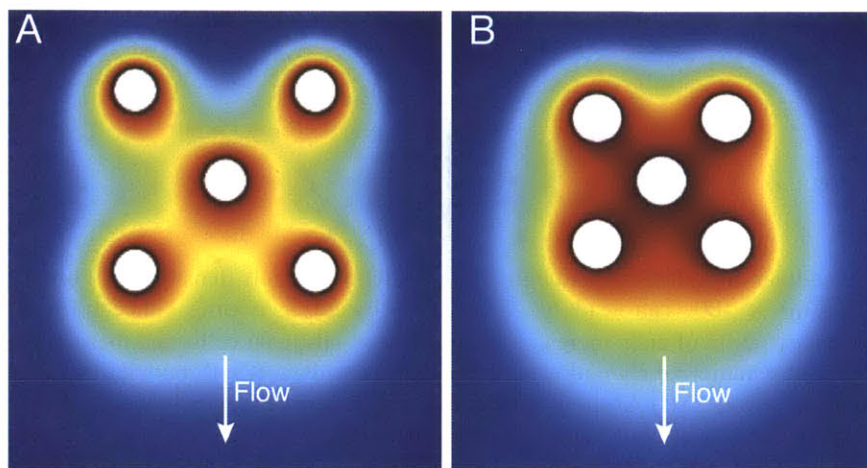
Figure 33. Transport model for demonstrating the effect of cell density on transcellular autocrine chemokine gradients. Normalized concentration, with red maximum concentration and blue minimum concentration. All parameters are the same in both figures, except cell density.

To quantify the pericellular gradient, we used a metric similar to the metric used by Fleury et al. to determine the pericellular gradient for single cells in interstitial flow (41) and similar to metrics used in chemotaxis assays (65). The pericellular gradient is defined as $(\Delta C/C_m) \times 100$, where ΔC is the difference in concentration between the downstream and upstream ends of the cell, and C_m is the concentration at the center of the cell. We found that as more cells are located upstream, the pericellular gradient decreased (Figure 34). In other words, increasing the cell density introduces more cells upstream and results in a lower magnitude pericellular autocrine gradient.
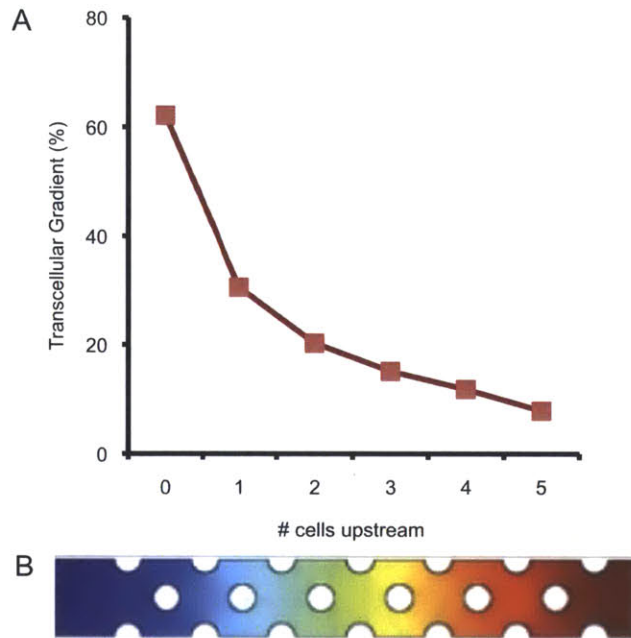
Figure 34. Pericellular morphogen gradients are a function of cell density. A) Pericellular gradients, defined as $(\Delta C/C_m) \times 100$, can lead to chemotaxis toward increasing concentration of chemokine. Increasing the concentration of cells increases the number of upstream cells, and these cells contribute to a decreased transcellular autocrine chemokine gradient. In these data, $R = 0$, but similar trends are observed for physiologic reaction rates. B) Absolute concentration of chemokine is a function of cell density. Color denotes normalized chemokine concentration (C/C_{Max}), blue indicates $C/C_{Max} = 0$, and red indicates maximum concentration $C/C_{Max} = 1$. White circles indicate cells, and cells are aligned with the x-axis of A to demonstrate the relationship between concentration field and concentration gradient.

3.9 Discussion

Interstitial flow influenced tumor cell migration and, in particular, dramatically affected the direction of migration. For all culture conditions with interstitial flow, cells preferentially migrated along streamlines. The relative fraction of the cell population that migrated along the streamlines, and the upstream and downstream bias along the streamline was a function of cell density, CCR7 activity, and interstitial flow velocity.

For cells seeded at 5×10^4 and 25×10^4 cells/ml in 3.0μm/s and 0.3μm/s flow fields, addition of CCR7 blocking antibody decreased the tendency for downstream migration. These data indicate that the CCR7 receptor is involved in downstream migration and thus support the findings of Shields et al., who identified the CCR7 chemokine receptor as critical in the signaling pathway responsible for autologous chemotaxis (40). Autologous chemotaxis is the result of a flow-induced gradient of an autocrine chemotactic signal that is detected by the CCR7 chemokine receptor and stimulates migration in the direction of flow. Our data confirm that CCR7 is involved in tumor cell migration, and

we provide validation for and the autologous chemotaxis model by demonstrating that CCR7 is directly involved in downstream migration.

Interestingly, in experiments without the CCR7 blocking antibody, migration direction was a strong function of cell seeding density. As cell concentration was increased, fewer cells migrated downstream, and a general tendency for migration in the *upstream* direction began to emerge. We expect the density dependence in the direction of cell migration is the result of the interaction between autocrine and paracrine chemokine concentration fields. Autologous chemotaxis, as the result of autocrine chemokine gradients, had previously been studied in the context of single cells (41), but when we included the effects of neighboring cells in our model, we observed that increasing cell density decreases the magnitude of the transcellular gradient for cells downstream of other cells (Figure 34). This is due to the fact that the local effects of a single cell become overwhelmed by the effects of ligand release from a population of cells. Consequently, increasing the cell density decreases the autocrine transcellular gradient, attenuating the signal for autologous chemotaxis, and reducing the tendency for CCR7-mediated migration downstream. As further validation that high cell concentration results in a weaker autologous chemotaxis stimulus, the directional migration trends are similar between cell populations seeded at high cell concentration and cell populations with blocked CCR7.

When CCR7 is blocked, directional migration scores decrease for all conditions tested. The decrease in streamline migration scores is pronounced for cells at 5×10^4 cells/ml; the average directional migration score changes sign from positive to negative, reflecting a shift in migration bias from downstream to upstream. Motivated by the negative directional migration scores for both cell densities and flow rates when CCR7 is blocked, we hypothesize that a CCR7-*independent* stimulus competes with CCR7-dependent autologous chemotaxis and when CCR7 is inhibited, stimulates cells to migrate upstream. The relative strength of these two stimuli governs the directional bias in migration for a cell population and is a function of cell density, interstitial flow rate, and CCR7 receptor availability.

The streamline and directional migration scores provide insight into the nature of the CCR7 independent stimulus. Directional migration scores monotonically decrease (become more negative) with increasing interstitial flow velocity, and this effect is independent of CCR7 activity and seeding density. In contrast, downstream migration of cells at low density peaks at a flow rate of 0.3um/s, then decreases at 3.0um/s. These data suggest that the CCR7 independent stimulus increases in strength with increasing interstitial flow velocity. Furthermore, when CCR7 is blocked, the directional migration score is independent of cell seeding density, suggesting that the strength of the CCR7 independent stimulus is cell density independent. Interestingly, the upstream migration stimulus persists even at low cell density and flow rate suggesting that the stimulus is independent of cell-cell interactions.

Cells at a density and flow rate that induce upstream migration demonstrate increased FAK activation (Figure 29). Because the upstream migration stimulus is independent of

cell density and a function of flow rate, and the force due to fluid flow is large enough to induce integrin activation, we hypothesize that the increased FAK activation is due to flow-induced stress gradients and resulting integrin activation. These stress gradients presumably lead to a difference in integrin and FA activation, with more activation upstream, where cell-matrix connections are in tension. We expect that this mechanism driving upstream migration is similar to that examined by Lo *et al.*, who demonstrated that a transcellular strain gradient, which presumably results in biased integrin activation due to the gradient in tension on the integrin receptors, guides cell migration toward increasing strain (118). Consistent with the hypothesis that flow-induced FAK activation drives upstream migration, we found that blocking Src kinase with PP2 reduced upstream migration (Figure 31).

We provide evidence that stress gradients and integrin-mediated FAK activation drive upstream migration, and these stimuli are a strong function of the dimensionality of cell culture conditions. We expect that the difference in integrin distribution for cells on a 2D substrate and in a 3D matrix is primarily responsible for the differences between our data and previous reports, which have demonstrated polarized activation of FAK downstream during lamellipodia formation and subsequent downstream migration in endothelial monolayers (183). Lin & Helmke demonstrated that migration direction is a function of geometry and confluency and that non-confluent endothelial cells undergo triphasic mechanotaxis, in which the cells migrate upstream over short time scales before migrating randomly and eventually migrating downstream, as opposed to endothelial cells in a confluent monolayer, which migrate downstream immediately upon application of shear flow (184). In addition to forces on the cell being pressure dominated rather than shear dominated for cells in 3D, recent work has demonstrated that migration in 3D is much different than 2D migration, and Fraley et al. have demonstrated that migration in 3D is predominantly governed by pseudopod activity and matrix deformation (133). Consistent with these data, confocal reflectance data support that cells in our devices are migrating in 3D, extending pseudopodia and leaving gaps in the matrix at the trailing edge as they migrate (Figure 18). Further understanding of the mechanism that drives upstream migration requires rigorous analysis of the fluid stresses imparted by IF on tumor cells and the effect of these stresses on focal adhesion related signaling.

Chapter 4: Mechanotransduction of interstitial fluid stresses and effect on tumor cell migration

4.1 Introduction

In Chapter 3, we investigated how elevated intratumor fluid pressure drives interstitial fluid flow and alters chemical transport within the tumor, and the altered transport environment influences tumor cell migration through the generation of autocrine chemokine gradients(40,48). Equally important, though not as well understood, is the drag imparted on the ECM and constitutive cells (44) by interstitial fluid, a similar stimulus to the FA-activating shear stresses generated on endothelial cells (185). With endothelial cells, shear stress is the dominant mechanical stimulus and induces FAK activation and cytoskeletal remodeling; however, for cells embedded within porous media, the ratio of the force due to the pressure drop across the cell length to the total shear force is inversely proportional to the hydrogel permeability (Equation 8), and the permeability of the collagen I hydrogel used in this study is small ($1\times10^{-13}\,m^2$), resulting in an integrated pressure force that is >30x the integrated shear force for a $20\mu m$ diameter cell (Equation 8). To maintain static equilibrium, all fluid stresses imparted on the cell must be balanced by tension in matrix adhesions. In 2D, the adhesions balancing the fluid drag on the cell are confined to the basal cell surface, while in porous media, such as breast stromal ECM, matrix adhesions are distributed across the full 3D cell surface. Consequently, maintaining static equilibrium requires greater adhesion tension on the upstream side of the cell to balance fluid stresses. From the reference frame of the cell, the effect of IF is mechanically equivalent to applying a net outward force at matrix adhesions on the upstream side of the cell, similar to the net tensile stresses applied by optical or magnetic trap to study the molecular mechanisms underlying mechanotransduction (106,186).

In this chapter, we explore the fluid stresses imparted on cells by IF. We demonstrate that the forces required to balance drag imparted on the cell by IF induce a transcellular gradient in matrix adhesion tension, and the tensile stresses at the upstream side of the cell induce FA reorganization and polarization of FA-plaque proteins including vinculin, paxillin, FAK, FAK^{Y397}, and α-actinin. FA polarization leads to paxillin-dependent actin localization, the formation of protrusions upstream, and rheotaxis. Consistent with the governing mechanism of durotaxis on 2D substrates, this 3D mechanotransduction occurs through FAK and requires paxillin. Silencing paxillin does not affect cell migration speed but does attenuate rheotaxis. IF is present in many tissues *in vivo* (187), and because FA polarization and rheotaxis result from a mechanical force balance, this 3D mechanotransduction mechanism is fundamental to cells embedded within porous ECM.

4.2 Profile of stresses imparted on cell by IF

The stresses imparted on a cell embedded within a collagen gel can be estimated from Ganapathy's solution for flow past a sphere embedded within a Brinkman medium(188). The dimensionless permeability (Equation 4) is defined as:

$$\sigma = \sqrt{\frac{K}{a^2}\left(1 + \frac{5}{2}\varphi_s\right)}$$

Equation 4. Dimensionless permeability in Ganapathy's notation

where K is the permeability, a is the sphere radius, and ϕ_s is the solid fraction of the medium. From CRM images (Figure 1, we determine $\phi_s < 1$ ($\phi_s \sim 0.11$ for Figure 35), and the dimensionless permeability reduces:

$$\sigma \sim \sqrt{\frac{K}{a^2}}$$

Equation 5. Dimensionless permeability in the low mass fraction limit

The total drag on a sphere in a Brinkman medium is given by:

$$D = U_0 a \mu \left[2\pi\left(1 + \frac{1}{\sigma} + \frac{1}{\sigma^2}\right) + 4\pi\left(1 + \frac{1}{\sigma}\right) \right]$$

Equation 6. Drag on a sphere in a Brinkman's medium as determined by Ganapathy

Where D is the total drag force, U_0 is the free stream velocity, μ is the viscosity of the fluid medium. The first term in Eq. S3 is the drag force due to the pressure drop across the sphere, and the second term is due to the viscous shear stress on the sphere surface. In our system (K=10^{-13}m^2, a=10^{-5}m, U_0=4.6μm/s), the total integrated drag force due to pressure is 235pN and the integrated shear force is 16.8pN. Because $\sigma<1$ (K=10^{-13}m^2, a=10^{-5} gives σ=0.0316), the force due to the pressure drop and the force due to the shear stress scales as:

$$D_{shear} \sim \frac{1}{\sigma}, \quad D_{pressure} \sim \frac{1}{\sigma^2}$$

Equation 7. Scaling of drag on a sphere in low permeability limit

By taking the ratio of the force due to pressure stress to the force due to shear stress, we find that the force due to the pressure drop across the cell dominates the integrated shear force:

$$\frac{D_{pressure}}{D_{shear}} \sim \frac{\left(\dfrac{1}{\sigma^2}\right)}{\left(\dfrac{1}{\sigma}\right)} \sim \frac{1}{\sigma} \sim \frac{a}{\sqrt{K}}$$

Equation 8. Ratio of the force due to pressure drop to the force due to shear

For a sphere with a 10μm radius, and a collagen gel with the permeability of $10^{-13}\, m^2$, $D_{pressure}/D_{shear}=31.6$.
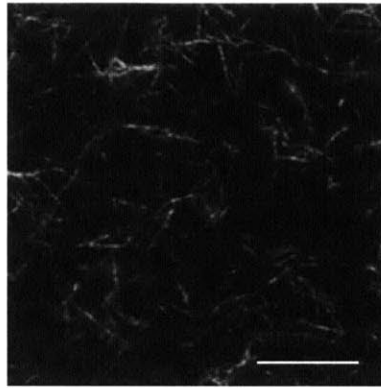
Figure 35. Confocal reflectance image of collagen gel. Scale bar 30μm.

4.3 Methods for investigating mechanotransduction of fluid stresses

Device preparation - HTD microfluidic devices were fabricated via soft lithography as described above, and seeded with MDA-MB-231 cells. Flow was applied as described in Chapter 2 (60Pa pressure drop for 4.6μm/s flow). For migration experiments, culture medium was supplemented with 20ng/ml hEGF (Peprotech) to stimulate cell migration. Phase contrast images were taken every 15 min for 8 h in an environmental chamber held at 37 °C and 5% CO2.

Drugs and inhibitors - For β1-integrin blocking, cells were re-suspended in growth medium supplemented with 50μg/ml mouse monoclonal anti-β1 integrin blocking antibody (P5D2 Abcam), and 20μL of cells in blocking medium was mixed with 200μL of 2mg/mL collagen type I for a final concentration of 5μg/mL anti-β1 integrin antibody in gel solution. After gelation, growth medium with 5μg/mL anti-β1 integrin antibody was added to hydrate the gel. For MMP blocking experiments, collagen gel was synthesized as described above with 2 U/mL aprotinin (Sigma) added to gel solution, and after gelation, growth medium with 10 Units/mL aprotinin was added to hydrate the gel. To degrade the glycocalyx, growth medium supplemented with 15 U/L heparinase (Sigma) was added to hydrate the gel after polymerization, and for tyrosine kinase inhibition, genistein (Sigma) was added to growth medium at a 100μM.

Transfection and selection - MDA-MB-231 cells stably expressing vinculin-GFP fusion protein were generated by lipid transfection and neomyocin selection. The vinculin-GFP plasmid has been described and characterized previously(189) and was a gracious gift of Prof. Benjamin Geiger (Weizmann Institute of Science), and the plasmid contains a gene coding for neomyocin, conferring resistance to geneticin (Invitrogen). Cells were grown to 70% confluence in 24-well plates and a solution of 0.5mL growth medium, 1.7μL Lipofectamine-LTX (Invitrogen), 0.5μg plasmid DNA, 025μL PLUS (Invitrogen), and 100μL OPTI-MEM (Invitrogen) was added to each well. Control cells were exposed to the same transfection medium without plasmid DNA. After 12hrs of incubation, the transfection medium was replaced with 1mL growth medium per well and cells were incubated overnight. Cells were then transferred to a 6-well plate and incubated in growth medium until confluent, and growth medium was replaced with selection medium containing 3mg/ml geneticin (Invitrogen) in growth medium. Cells were incubated for 48hrs in selection medium, passaged, and further incubated for 72hrs in selection medium. Resistant cells were moved to a T25 culture flask and incubated in growth medium for 1-2weeks. GFP-expressing cells were selected via FACS and subsequently cultured in growth medium. siRNA against human paxillin (gtg tgg agc ctt ctt tgg t) was generously provided as a gift from the Ingber lab (126). Cells were grown to 70% confluence in 6-well plates and transfected using SiLentFect (Bio-Rad) following manufacturers protocol. 24hrs after transfection, cells were seeded in microfluidic devices.

Fixation and imaging - The pressure gradient was monitored and maintained for 4hrs before the medium was replaced with 4% paraformaldehyde (Electron Microscopy Sciences) for fixation. The pressure head was maintained with PFA to fix cells in the flow condition. After fixation, cells were solubilized with 0.1% Triton-X 100 (Invitrogen) and stained for actin with AlexaFluor-568 phalloidin (Invitrogen), paxillin, FAK, FAK^{Y397}, α-actinin, cortactin, and/or DAPI. Cells were imaged with a laser-scanning confocal microscope (FV-1000, Olympus).

Image processing – Full z-stacks of single cells were imaged at 60x magnification with a confocal laser-scanning microscope. Median slices were used for subsequent analysis to decouple membrane geometry and signal intensity. For actin and vinculin imaging, images were binarized and the contour of the cell was determined via the Matlab image processing toolbox. The contour was diluted inward by 2μm to create an annular mask of the cell periphery. The mask was then applied to the original image, and the resulting image was an intensity map of fluorophore emission at the cell membrane. The centroid of the resulting image was determined, and the image was divided into two images each containing only pixels upstream or downstream of the centroid.

Collagen fibers were imaged via confocal reflectance microscopy by collecting 405nm wavelength light reflected by matrix fibers. Matrix intensity images were processed by a similar method to actin and vinculin processing. In brief, contours of vinculin images were diluted outward to create a mask that was applied to confocal reflectance images. After the mask was applied to the reflectance image, intensity values are indicative of

light reflected by collagen fibers at the cell periphery. The centroid, upstream pixels, and downstream pixels were determined with a Matlab script.

Paxillin siRNA characterization - RNA was purified using RNeasy mini kit (Qiagen). qRT-PCR was performed with iScript cDNA synthesis kit (Bio-Rad) and iTaq Sybr Green Supermix (Bio-Rad) using CFX96 real-time PCR machine (Bio-Rad). β2-microglobulin controlled for complementary DNA content. Primers for paxillin are:

Table 3. Paxillin primer sequence

	Forward	Reverse
Human paxillin	5'-CTGGCGGACTTGGAGTCTAC-3'	5'-CTCCTCCGACAAGAACACAGG-3'
Human β2-microglobulin	5'-GAATGGAGAGAGAATTGAAAAAGTGGAGCA-3'	5'-CAATCCAAATGCGGCATCTTCAAAC-3'

Image processing for FA protien distribution – 3D images of vinculin and actin were acquired by a laser point-scanning confocal microscope (Olympus FV1000) and processed to measure the distribution of actin and vinculin at the cell boundary (Figure 36). Raw images were taken of cells within microfluidic devices at 60x magnification. The median image in z (half way between the top and bottom of the cell) was extracted in ImageJ and processed in Matlab. Images were filtered by a 3-pixel mean filter to reduce noise, and an image intensity threshold was calculated by Otsu's method(190). Pixels with intensity greater than this threshold were assigned a value of 1, while pixels below the threshold were assigned a value of 0. Holes in the binary image were defined as pixels with a value of 0 that cannot be accessed from an image corner without crossing a pixel of value 1. The pixels within holes in the image were assigned a value of 1 to create a filled black and white image of the cell. Pixels are identified as perimeter pixels if they have a value of 1 and share at least one edge with another 1-valued pixel and at least one edge with a 0-valued pixel.

The contour of the image was dilated inward, toward the cell centroid, by an empirically determined thickness (Figure 37). The resulting mask (Figure 36) was multiplied pixel by pixel with the original, filtered image. In the resulting image, only pixels at the cell periphery have nonzero intensity. The centroid of the cell was determine from the un-dilated, perimeter image, and all pixels on the upstream side of the centroid are labeled "upstream," while those to the downstream side of the centroid are labeled "downstream."
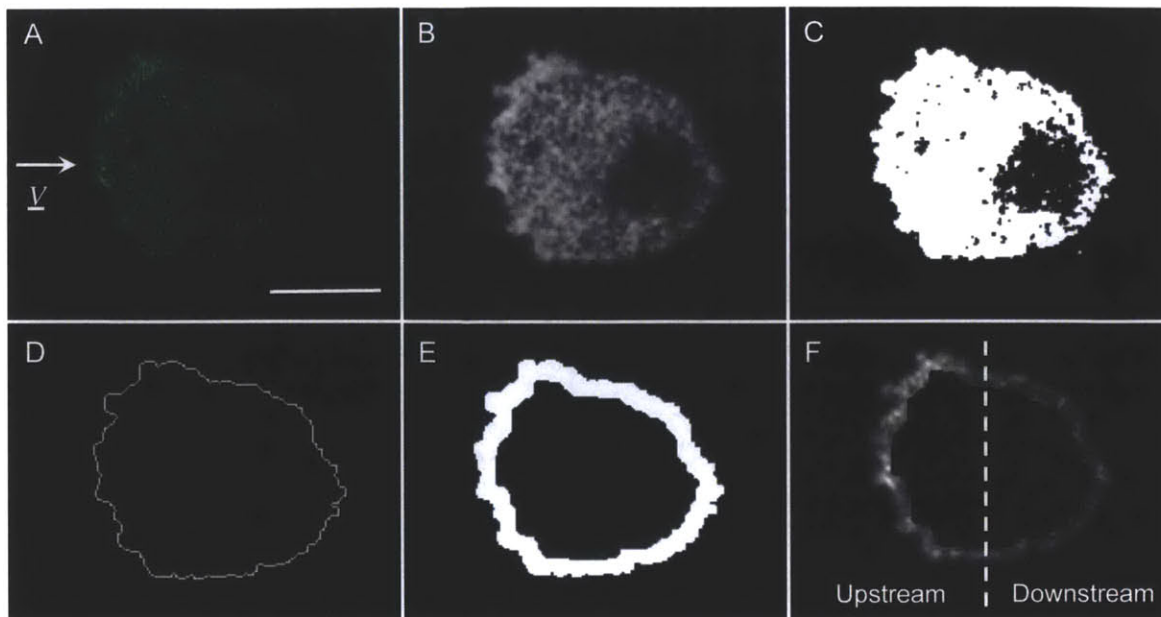
Figure 36. Method for processing and segmenting vinculin and actin images. A) Raw image of MDA-231-VinGFP exposed to 3 μm/s flow (from left to right as indicated by arrow). Confocal point-scanning microscope is used to take 3D image of cell at 60x magnification, the median in z is used to quantify actin and vinculin distribution. B) The image is filtered by averaging with a 3-pixel averaging filter. C) The image is converted to black and white based on a threshold determined by Otsu's method. D) All holes (pixels of background intensity that cannot be reached by filling from any corner of the image) are filled in the binary image and the contour of the filled image is determined by identifying non-zero pixels that share at least one edge connected to another non-zero pixel and at least one edge connected to a background pixel. E) The image contour is dilated inward (toward cell centroid) by a thickness determined experimentally (see SI Results). F) The dilated binary boundary image is multiplied pixel by pixel with filtered image (B) so pixels not on the cell periphery are assigned intensity values of 0. The centroid of the cell is determined and upstream pixels are defined as those on the upstream side of the centroid while downstream pixels are defined as those on the downstream side of the centroid. Scale bar is 10 μm.

Determining the appropriate mask thickness for analyzing vinculin distribution at cell periphery. In order to attenuate the effects of vinculin that is not associated with the membrane, we created a filter to block all fluorescence intensity that is not at the cell membrane. We can determine the cell periphery as described in Figure 36, but we need to determine the thickness of the mask (Figure 36E). Consequently, we diluted the mask from the cell membrane incrementally, and quantified the results (Figure 37). Ultimately, we wanted a mask thick enough to capture all of the information at the cell boundary, but not thick enough to include the nucleus, which would alter our measurement of fluorescence intensity.

We calculated the effect of mask thickness on a normalized measure of polarization for a single cell, and for the whole cell population exposed to flow. The polarization metric is computed by measuring the average intensity at the upstream and downstream edges of the cell (I_{up} and I_{down}, respectively) for the median slice of a confocal image stack acquired for each cell:

$$Polarization = \frac{\langle I_{Up} \rangle - \langle I_{Down} \rangle}{(\langle I_{Up} \rangle + \langle I_{Down} \rangle)/2}$$

Equation 9. Polarization metric for measuring distribution of FA proteins

For the single cell, we observed some variation in polarization with mask thickness for thicknesses less than 20 pixels, but for masks thicker than 20 pixels, the value of polarization reached a stable value around 0.46 (at 0.11 μm/pixel for these images Figure 37). We repeated this process of incrementally diluting the mask and calculating polarization for a large subset of the cells exposed to flow (n=95, Figure 37D). A similar pattern of variation was found for the cell population, and the value of polarization reached a constant value around 0.23 at a thickness of 12 pixels. The median thickness of this range over which polarization is constant is 20 pixels, so 20 pixels was chosen as the thickness of the mask for quantifying vinculin distribution.
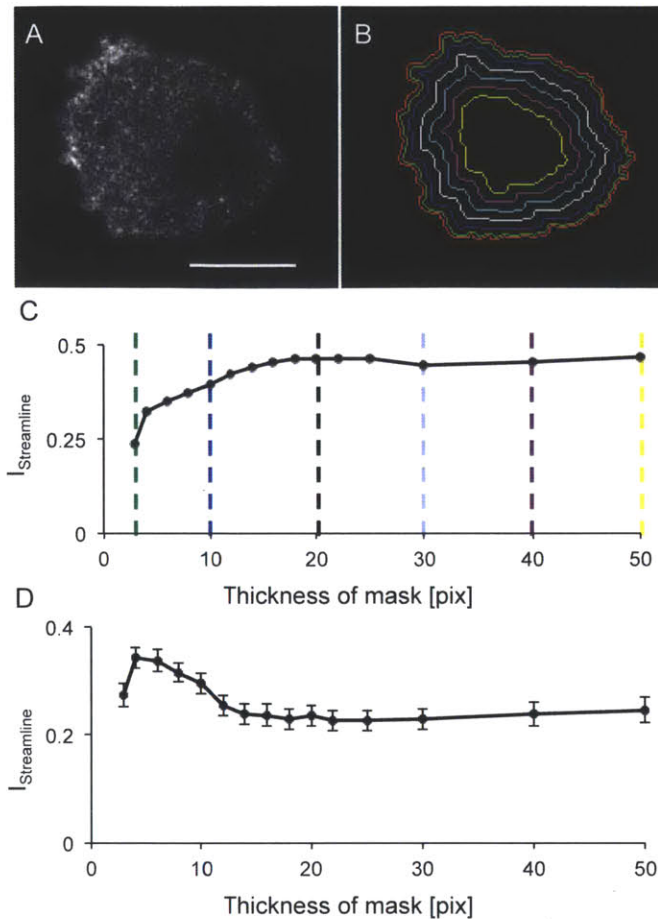
Figure 37. Thickness of mask for measuring vinculin distribution at cell periphery. (A) Raw image of vinculin distribution in a median slice of a confocal stack of images. Scale bar is 10μm (B) Contours of various dilations of the cell periphery. Cell boundary indicated in red, and lines toward the cell centroid indicate periphery dilations of 4, 10, 20, 30, 40, and 50 pixels respectively. C) Polarization for each of the dilations shown in (B). Dashed lines of a given color reflect the contour of the same color in (B). Although there is some variation in polarization for small membrane dilations, the value stabilizes after about 20 pixels. D) Population mean polarization ± SEM values for vinculin images of cells under flow conditions (n=95, m=7). Smaller thicknesses do not capture the intense staining patterns at the cell periphery, while large thicknesses tend to include intensity variations from the nucleus. Therefore, a thickness of 20 pixels was chosen as an optimal thickness, as this value reflects the minimum thickness at which the polarization measurement is stable.

Image processing for collagen fibers – Collagen reflects 408nm light, and collecting reflected light via confocal reflectance microscopy (CRM) has emerged as a convenient method for imaging collagen microstructure without the use of fluorescent labels (191,192). In a similar method to processing the vinculin and actin images, CRM 3D images of the collagen matrix were acquired and processed in Matlab. The boundary of a binary image created from the median slice of the vinculin images was created as described above (Figure 36). However, instead of diluting the perimeter inward to look at fluorescence intensity within the cell, the perimeter of the vinculin image was diluted

outward by an empirically determined amount to create a mask for the pericellular matrix (Figure 38). This mask was applied to the median slice of the CRM images, and upstream and downstream pixels were defined by the pixels upstream and downstream of the centroid of the vinculin perimeter image.
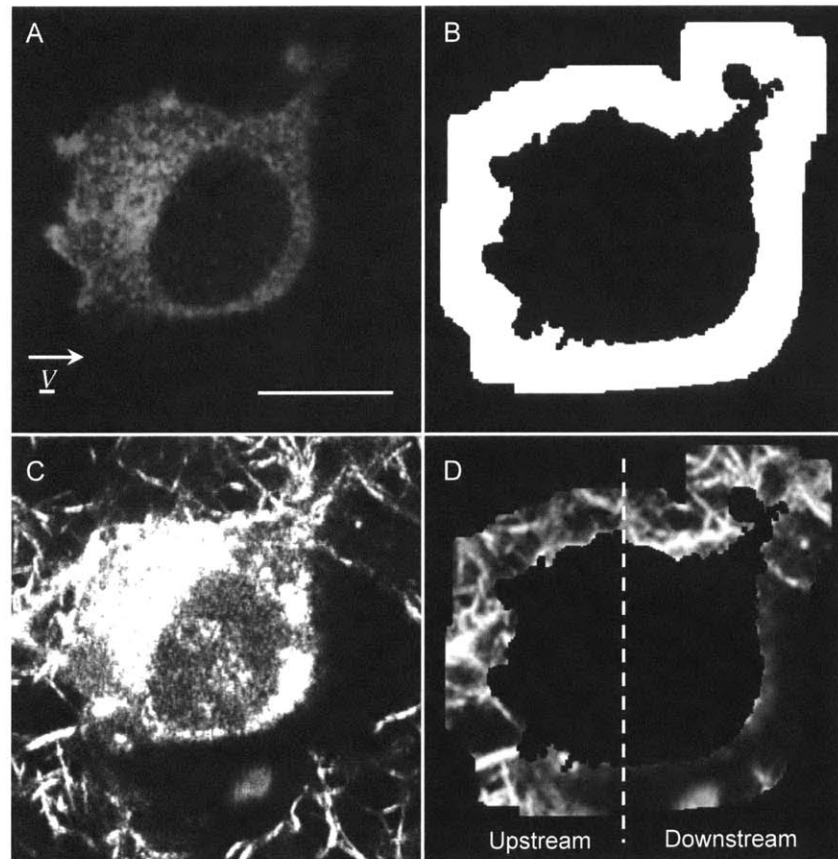
Figure 38. Method for quantifying matrix structure from CRM images. (A) Image of vinculin distribution for the CRM image in (C) used to create a mask for the CRM image. (B) The vinculin image was binarized to deterimine the cell boundary as demonstrated in Fig. S2A-D, and the cell boundary was diluted outward from the cell (SI Results) to create a mask for the CRM image in (C). C) Median slice of a CRM stack of images. The fibrous structures around the cell are the collagen fiber, and a gap between the cell and the matrix can be seen clearly on the downstream side of the cell. D) The mask from (B) is applied to the CRM image in (C) to generate an image of the CRM intensity of the local pericellular matrix. The centroid of the vinculin image is used to determine upstream and downstream pixels. Scale bar is 10μm.

Determining the appropriate mask thickness for quantifying pericellular matrix architecture. CRM images provide detailed information about collagen architecture, and we employed CRM to determine the effect of interstitial flow on the collagen structure. To restrict our analysis to the pericellular collagen matrix, we developed a filter to attenuate reflectance signal within the cell cytoplasm and far from the cell periphery **Figure 38**). To ensure our results were not dependent on the mask thickness, we varied the thickness of the mask and measured polarization for the CRM images (

Figure 47).

We determined the effect of mask thickness on a single cell, and for the cell population exposed to flow (Figure 39). For the single cell, we found that polarization reaches a minimum of -0.27 at 25 pixels. At larger mask thickness, polarization approaches 0 as the matrix is of similar architecture upstream and downstream far from the cell. We next quantified the effect of mask stiffness on the mean value of polarization for the cell population (n=85, Figure 39D), and we found that the polarization varied for thin masks, reflecting highly variable matrix structure at the cell membrane. For larger thicknesses, polarization approaches 0, but the value is stable around -0.13 between 4-30 pixels. Therefore, a thickness of 17 pixels was chosen as an optimal thickness, as this value reflects the median thickness for which the polarization measurement is stable.
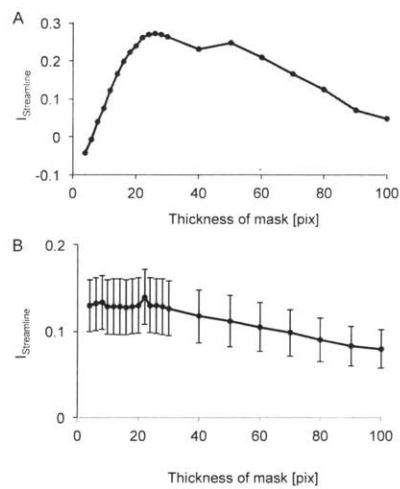
Figure 39. Method for quantifying pericellular matrix architecture. A) Polarization for contour dilations of increasing thickness. Polarization reaches a maximum at 25 pixels. At larger value, polarization approaches 0 as the matrix is of similar architecture upstream and downstream far from the cell. D) Population mean polarization ± SEM values for CRM images of cells under flow conditions. Larger thicknesses approach 0, but the value is stable between 4-30 pixels. Therefore, a thickness of 17 pixels was chosen as an optimal thickness, as this value reflects the median thickness for which the polarization measurement is stable.

4.4 FA protein distribution in 3D

For all data presented in Chapter, 4, the HTD was used to increase experimental throughput by allowing more cells/device than in the microinjection device (

Figure 40A). We introduced a 60 Pa pressure gradient across a 2mg/ml collagen gel to drive flow with a mean velocity of 4.6µm/s, measured along the centerline of the device. The total fluid drag force imparted on a spherical cell can be calculated from the solution for drag on a sphere within a Brinkman medium(188), and for our experimental setup, a 16.8pN integrated shear force and 235pN integrated pressure force is imparted on each 20µm-diameter cell (**Equation 6**).
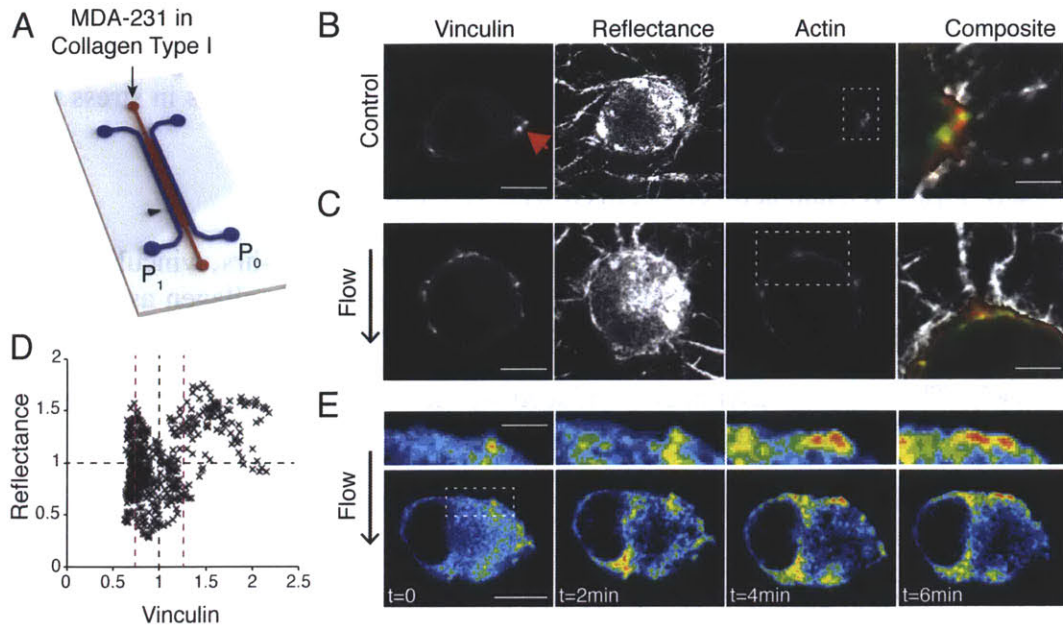
Figure 40. Interstitial flow induces reorganization of matrix adhesions. A) Microfluidic platform for applying interstitial flow (IF) with collagen/cell suspension indicated in pink and cell culture medium indicated in blue. The gel region is 200μm deep, and a pressure gradient ($P_1 > P_0$) is established across the gel region to drive IF (scale bar 2.5mm). B) MDA-MB 231 cells embedded within 2mg/ml collagen gel are characterized by diffuse distribution of vinculin with regions of high vinculin concentration at the cell periphery (red arrow, scale bar 8μm), where large collagen fibers are in contact with the cell, as seen in the reflectance channel. Actin is confined to the periphery of the cell and colocalizes with vinculin. Composite images, demonstrate that regions of intense vinculin and actin staining correspond to regions where collagen fibers extend radially outward from the cell surface (red actin, green vinculin, grey reflectance, scale bar 3μm). C) 4.6 μm/s flow induces vinculin and actin localization at the upstream edge of the cell (scale bar 9μm). Composite images demonstrate upstream localization of actin and vinculin where the cell is in contact with collagen (actin red, vinculin green, reflectance grey, scale bar 3μm). D) Colocalization of vinculin and collagen at the cell membrane, where each data point represents a location on the cell membrane, Regions where vinculin intensity is greater than the mean (vertical black dashed line) + 1SD (red dashed line) correspond to regions with high reflectance intensity. E) Vinculin accumulates rapidly at the upstream side of the cell. 16-color intensity histograms (Red=max, blue=min) demonstrate intense vinculin localization within 4min of 4.6 μm/s flow (scale bar 8μm, inset scale bar 3 μm).

71

MDA-MB 231 mammary adenocarcinoma cells embedded within 2mg/ml 3D collagen type I gels displayed diffuse distribution of vinculin and less prominent punctate vinculin aggregates than when cultured on 2D glass substrates coated with collagen type I, and F-actin was localized to the cell periphery rather than traversing the cells in stress fibers as in 2D (

Figure 40B, **Figure 41**), and actin colocalized with vinculin (

Figure 42A). When cells were exposed to 4.6μm/s flow for 4hrs, vinculin and actin localized at the upstream edge of the cell, while the density of collagen as measured by confocal reflectance microscopy was reduced at the downstream edge of the cell (

Figure 40C). The vinculin asymmetry induced by flow is due to an increase in FA-like vinculin clusters on the upstream side of the cell (

Figure 42B), and these FA-like clusters occur at regions where collagen is bound to the cell surface (

Figure 40D). Vinculin accumulation at regions of stress occurs rapidly (115), within 4 min of applying flow vinculin localizes upstream (

Figure 40E).
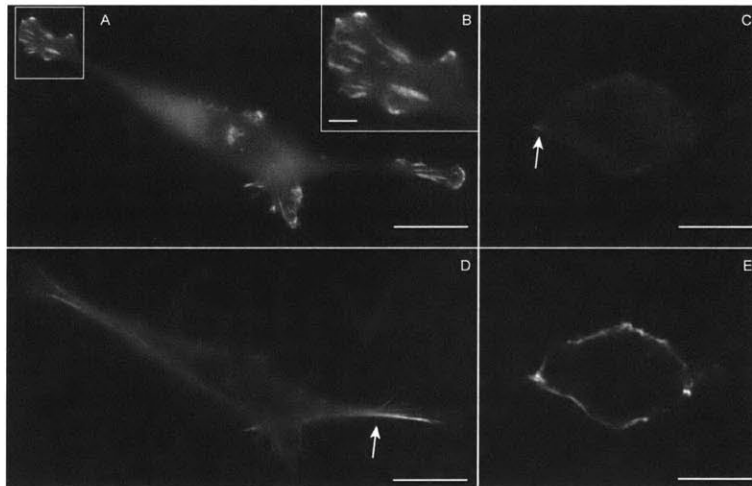
Figure 41. MDA-MB-231 expressing vinculin-GFP fusion protein. A) Fluorescent image of GFP-vinculin fusion protein demonstrates punctate staining at focal adhesions, consistent with previous reports[8,9]. B) Magnified image of focal adhesions. C) Median slice of GFP-vinculin expressing MDA-231 cell in 3D collagen gel. Staining is more diffuse than 2D, consistent with previous reports[10], but regions of vinculin accumulation can be seen. D) Actin stained for cell in (A) demonstrates typical stress fiber formation. E) Actin stain for cell in (C). Actin is distributed at the cell boundary in 3D.
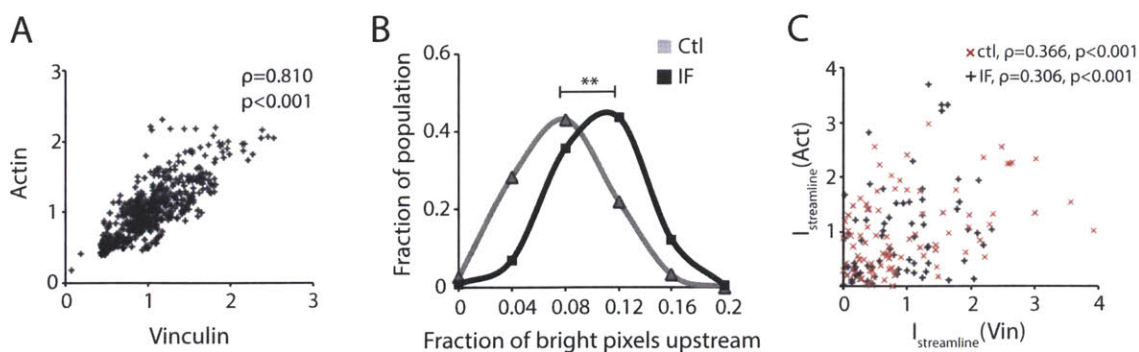
Figure 42. Flow induces FA reorganization. A) Vinculin and actin colocalize at cell membrane. For each pixel in the cell shown in Figure 1B, the intensity of vinculin was taken as the x-coordinate and actin intensity the y-coordinate. Each intensity value was normalized by the mean intensity of the respective channel across the whole cell (ϱ=Spearman correlation coefficient, p computed using exact permutation distribution). B) Increase in polarization for vinculin with flow is due to accumulation of brighter pixels at upstream side of the cell. The x-axis is the fraction of pixels at the upstream side of the cell greater than the mean + S.D. intensity for the entire cell. The y-axis is the fraction of the cell population with corresponding bright pixels upstream (histogram, **p<0.01). C) For both flow and control, higher polarization values for vinculin correspond to higher polarization values for actin. For each cell, the polarization value for vinculin was taken as the x-coordinate, and the polarization value for actin as the y-coordinate (ϱ=Spearman correlation coefficient, p computed using exact permutation distribution).

4.5 IF induces FA reorganization and upstream polarization of FA proteins

Integrin-based mechanotransduction involves a cohort of FA plaque proteins that accumulate at regions of locally applied stress and localize with vinculin and actin. In particular, adhesions containing paxillin elongate under applied traction (99), and FAK becomes autophosphorylated at Y397 through binding with β1 integrins in endothelial cells in response to shear stress (120) and in breast adenocarcinoma cells when exposed to 3 μm/s IF (48). Furthermore, phosphorylation of FAK at Y397 is required for invadopodia formation for breast cancer cells (193), and FAK^{Y397} is differentially expressed in metastatic cervical carcinoma relative to noncancerous epithelium (194). FAK is required for mechanical stress-induced cell polarization(113), and the FAK-paxillin-vinculin signaling complex is required for rigidity sensing and durotaxis (104). To quantify the localization of FA proteins, we defined a metric to measure the distribution of fluorescently tagged proteins at the cell membrane. The polarization metric is computed by measuring the average intensity at the upstream and downstream edges of the cell (I_{up} and I_{down}, respectively) for the median slice of a confocal image stack acquired for each cell (Figure 43):

$$Polarization = \frac{\langle I_{Up} \rangle - \langle I_{Down} \rangle}{(\langle I_{Up} \rangle + \langle I_{Down} \rangle)/2}$$

Equation 10. Metric for quantifying polarizaiton of FA proteins

73

IF (4.6μm/s flow for 4hrs) caused a statistically significant increase in polarization for vinculin (from 0.034±0.013 to 0.209±0.013, mean ± S.E.M.), actin (from -0.033±0.023 to 0.177±0.020), and collagen (from -0.040±0.030 to 0.105±0.025, **Figure 43**), and for both control and flow, cells with higher magnitude polarization for vinculin correlated with high polarization for actin (

Figure 42C). The fraction of the cell population with upstream polarization increased with flow; 81% of cells exposed to 4hrs of flow displayed polarization values greater than the mean of the control cells (no flow), and 50.2% displayed values greater than the mean + 1 S.D. of control cells (compared to 48% and 14%, respectively for control). A similar trend was observed for actin, with polarization of 77% of cells with flow greater than the mean of the control cells and 33% of cells exposed to flow greater than the mean + 1 S.D. of control cells (compared to 47.7% and 14%, respectively for control).

Furthermore, flow induced a statistically significant increase in polarization for paxillin (from 0.027±0.029 to 0.117±0.022), FAK (0.032±0.041 to 0.180±0.036), and FAK^{Y397} (0.030±0.033 to 0.228±0.034), indicating that these FA plaque proteins localize to the upstream cell periphery under flow (Figure 43). IF also induced upstream localization of α-actinin (**Figure 44**), an actin crosslinking protein critical for the extension of lamellipodia in 2D (195) that localizes to regions of traction applied by magnetic trap (106).
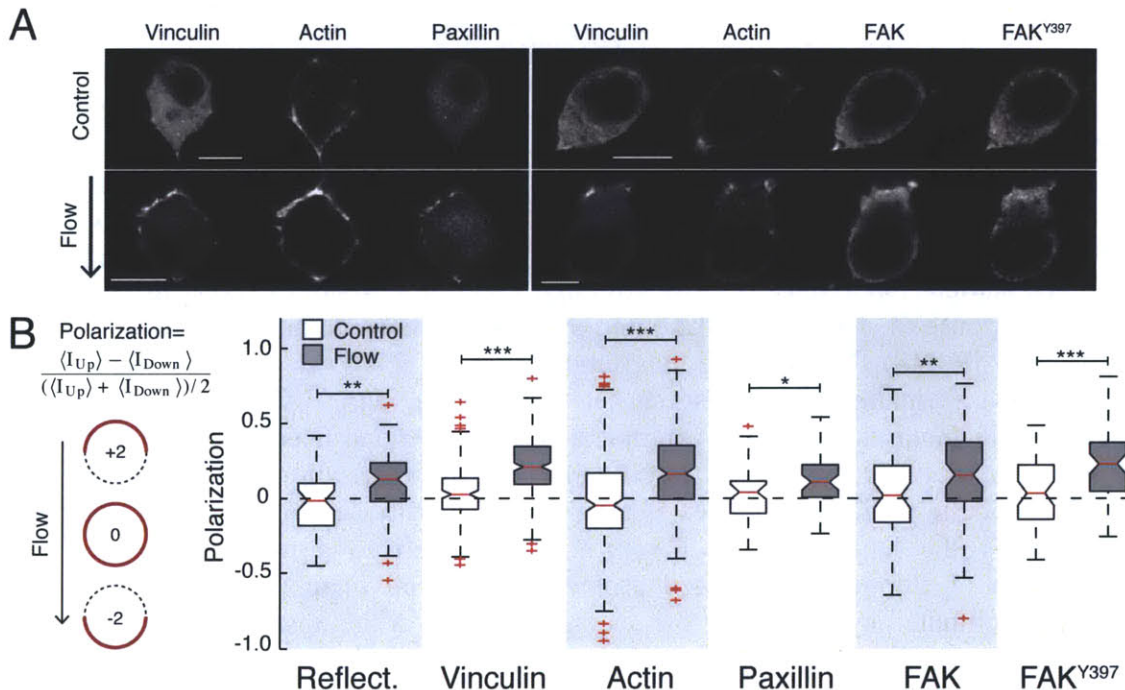
Figure 43. Focal adhesion proteins localize to the upstream side of cells exposed to IF. A) Paxillin, FAK, and FAK^{Y397} are distributed diffusely throughout the cell cytoplasm but weakly colocalize with actin and vinculin at the cell periphery. Flow induces upstream polarization of each protein (scale bar 10μm). B) Polarization is measured by the relative upstream fluorescence intensity of each signal at the cell membrane; +2 is maximum upstream polarization, while -2 is maximum downstream polarization. Upstream polarization increases for collagen ECM, vinculin, actin, paxillin, FAK, and FAK^{Y397} in cells

exposed to 4.5μm/s flow. (***p<0.001, **p<0.01, *p<0.05 calculated from Wilcoxon rank-sum test with >45 cells from >3 devices for each condition).
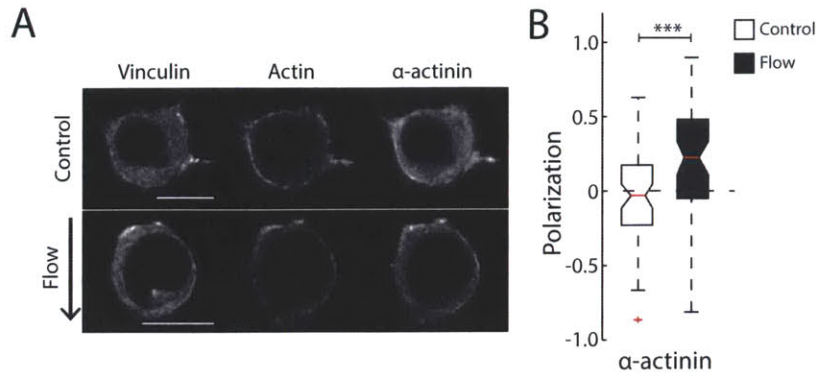
Figure 44. α-actinin localizes upstream with flow. A) α-actinin is diffusely distributed throughout the cytoplasm but colocalizes with actin and vinculin at the cell membrane and polarizes to the upstream membrane under flow (scale bar 10μm). B) Polarization of α-actinin increases with flow (***p<0.001, calculated from Wilcoxon rank-sum test with >45 cells from >3 devices for each condition).

To ensure the vinculin-GFP plasmid does not influence the distribution of vinculin within the cell, we repeated the flow experiments with MDA-MB-231 parental cells. Antibody staining demonstrated a similar staining pattern for vinculin as the constitutively expressed plasmid (Figure 45). In the presence of flow, vinculin accumulated at the upstream side of the cell as determined by antibody staining (Figure 45). Polarization was significantly different for the cells exposed to 3μm/s flow (Polarization= -0.1991 for flow, Polarization= 0.0371 for control, p=0.0014), with 80% of the cell population demonstrating a positive Polarization when exposed to flow, indicating vinculin accumulation on the upstream side of the cell.
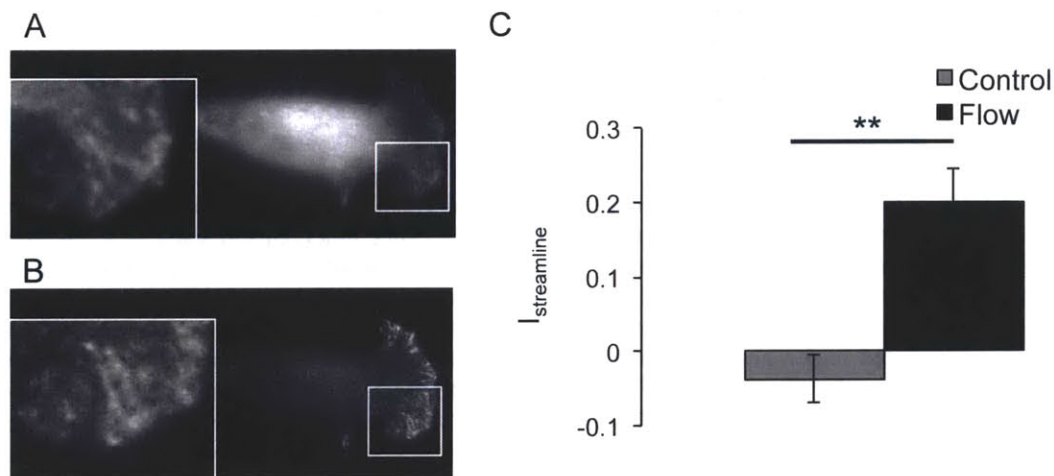
Figure 45. Anti-vinculin antibody demonstrates similar protein expression patterns to vinculin-GFP fusion protein. A) Antibody stain for vinculin in MDA-MB-231 cells expressing vinculin-GFP fusion protein

cultured on collagen coated glass. B) GFP imaging of fusion protein for the cell stained in (A). Insets show similar staining pattern for antibody and fusion protein. C) Vinculin accumulates at the upstream side of the cell for MDA-MB-231 parental cells (**p<0.01).

Each cell imaged for vinculin distribution was imaged with a confocal laser-scanning microscope to acquire full 3D distribution of fluorescence intensity. The images are acquired by defining the top and bottom of the cell and imaging 11 x-y slices between the top and bottom. Consequently, the 6th x-y slice is at the middle of the cell, and we quantified vinculin, actin, and collagen concentration at this plane. We chose to quantify the median plane rather than the sum of the 11 planes as to not confuse membrane geometry with intensity (ie/ a thicker region of a cell would appear more intense in the sum of the slices). However, we found that vinculin accumulates at the upstream side of the cell when both the median slice and the sum of the slices are quantified (Figure 46). Although vinculin accumulates at the upstream side of the cell for both methods (polarization = 0.194 for the median slice and 0.119 for the sum of slices), the sum is more variable (S.D. = 0.1761 for median slice and 0.2571 for sum of slices). Furthermore, the nucleus has a significant effect on the sum of the slices (at the median slice, we can calculate polarization just at the periphery of the cell to neglect the effect of the nucleus, but when summing slices, the location of the nucleus, which does not contain vinculin, contributes to variability in the measurement, Figure 46B).
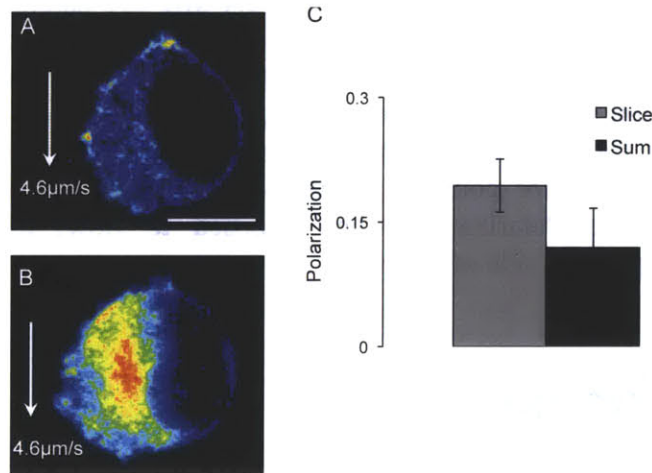
Figure 46. Median slice vs. sum of slices for confocal stacks of vinculin distribution for cells under flow conditions. A) Heat-map of vinculin-GFP intensity for the median slice in a confocal stack of a cell. Blue indicates minimum intensity while red is maximum intensity. Scale bar is 10μm. B) Heat-map for collapsed confocal stack of a cell. 11 slices, taken at 1.5μm intervals were summed to create the image. Blue is minimum, while red is maximum. Large contributions from vinculin accumulated around the nucleus can be seen by the intense red region near the center of the cell. C) Quantification of polarization for median slices and the sum of slices for 30 cells under flow. The line plot reflects the histogram of polarization data, while the bar plot demonstrates mean ± S.E.M. The stack and the median slice both demonstrate vinculin accumulation on the upstream side of the cell, but the data from the collapsed stack is more variable (S.D. of 0.2571 for sum and 0.1761 for median).

4.6 FA protein polarization occurs via β1-integrin signaling

The collagen matrix becomes anisotropically distributed under flow (Figure 43), and it is possible that the FA plaque protein polarization is a consequence of the dense matrix on the upstream side of the cell, which presents more adhesion sites than the downstream matrix. When cells were incubated with aprotinin, a broad MMP inhibitor (196), the pericellular matrix remained isotropically distributed under flow, but vinculin and actin still localized upstream, suggesting that cell polarization is not due to matrix remodeling (

Figure 47A-B). Shi and colleagues found a heparan sulfate proteoglycan (HSPG) mediated increase in smooth muscle cell motility in response to IF (46). We incubated cells with heparinase to degrade the glycocalyx and applied flow for 4hrs, and we found that actin and vinculin polarization persisted, suggesting that HSPG-sensed shear stress is not responsible for polarization (

Figure 47C.). Blocking β1 integrin ligation by treating cells with anti-β1 blocking antibodies (197) attenuated the polarization of actin and vinculin in response to flow. The cells remained nearly spherical, and vinculin and actin were distributed evenly around the cell perimeter even when exposed to flow (

Figure 47D-E), providing further evidence that β1 integrin ligation and signaling is required for actin and vinculin polarization in response to flow.

Miyamoto *et al.* determined that tyrosine kinase activity is required for the formation of mature focal adhesions and for the accumulation of most focal adhesion plaque proteins, including F-actin, to nascent focal adhesions (88). However, the authors found that vinculin still localized to β1-integrins in response to integrin ligation even when cells were treated with genistein, a tyrosine kinase inhibitor. In our experiments, genistein attenuated the upstream accumulation of actin, FAK, and FAK^{Y397} in response to flow such that no statistical difference was observed in polarization between the static and flow cases. However, the polarization value for vinculin increased with flow (from -0.066±0.031 to 0.248±0.033) and 69% of cells demonstrated a polarization value greater than the polarization mean for the static samples (

Figure 47F-G), demonstrating that vinculin polarization is maintained even in the absence of tyrosine kinase activity, but tyrosine kinase activity is required for recruitment of FAK, FAK^{Y397}, and actin.
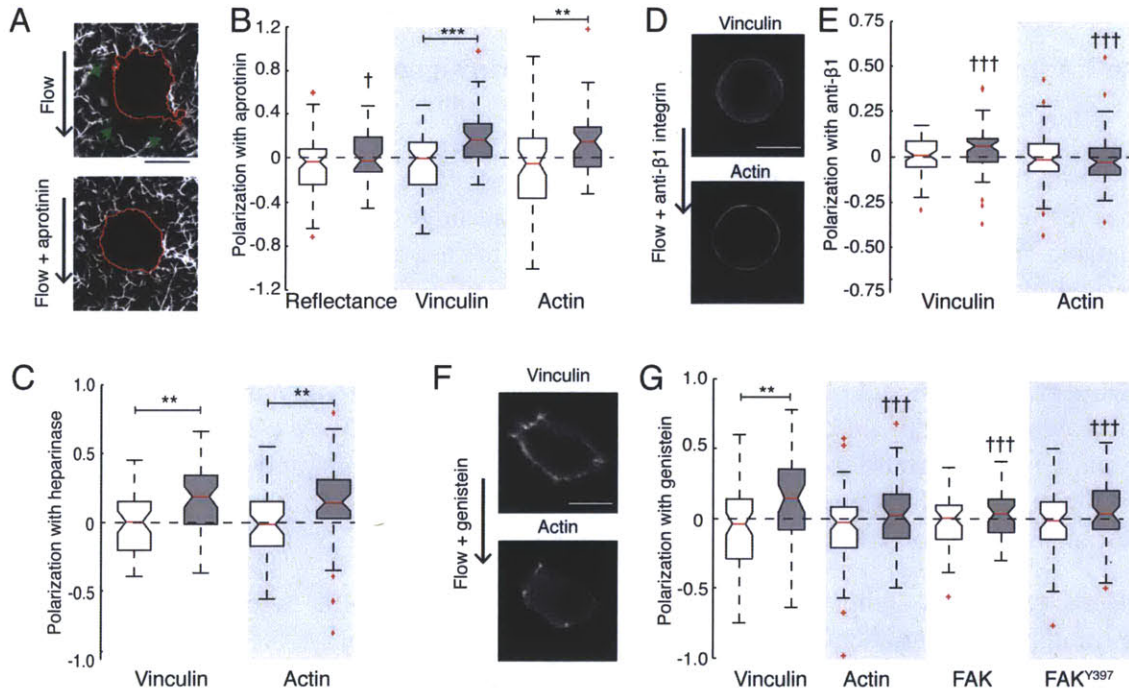
Figure 47. Focal adhesion reorganization is mediated by β1 integrins. A) The MMP inhibitor, aprotinin, blocks flow-induced ECM remodeling (downstream gaps in the matrix indicated by green arrows), resulting in isotropically distributed pericellular matrix. B) MMP inhibition by treatment with aprotinin attenuates polarization of ECM with flow, but vinculin and actin remain polarized and localize upstream (□ control, ■ flow for all graphs). C) Flow causes vinculin and actin polarization in cells treated with heparinase, which degrades HPSGs, demonstrating that the upstream focal adhesion and cytosketal polarization occur independent of the glycocalyx. D) Cells treated with anti-β1 integrin blocking antibodies displayed a spherical morphology with actin and vinculin isotropically distributed at the cell periphery. E) Anti-β1 integrin blocking antibodies attenuate actin and vinculin localization at the upstream cell edge, and there is no statistically significant difference in polarization of actin and vinculin with and without flow. F) Genistein, a broad tyrosine kinase inhibitor, reduced polarization of actin, FAK, and FAK^{Y397}. G) Inhibition of tyrosine kinase activity with genistein attenuated the polarizing effects of flow on actin, FAK, and FAK^{397}, though polarization of vinculin persisted. Scale bars 10μm, >45 cells from >3 devices for each condition, ***p<0.001, **p<0.01, *p<0.05, calculated from Wilcoxon rank-sum test. †p<0.05, †††p<0.001 measured vs. equivalent flow case with no drug applied).

4.7 Paxillin is required for upstream actin polarization and protrusion formation

Paxillin is required for stiffness mechanosensing (111), protrusion formation at regions of high stress (122), and durotaxis (104), and to evaluate the role of paxillin in upstream FA polarization and rheotaxis, we treated cells with paxillin siRNA. Treatment with specific siRNA against paxillin resulted in knockdown of paxillin expression by 80% as confirmed by immunoblotting (Figure 48A) and qRT-PCR (Figure 49), and no change in vinculin expression was observed (Figure 48A). Paxillin siRNA induced irregular cell morphology with increased protrusions and decreased polarization of vinculin and actin under flow (Figure 48B). Although modest vinculin polarization persisted, flow-induced polsarization of vinculin was attenuated with paxillin siRNA (0.089 ± 0.033 for paxillin siRNA with flow vs. 0.256 ± 0.034 for scramble siRNA with flow, Figure 48C), while paxillin siRNA blocked actin polarization (0.0035 ± 0.055 for paxillin siRNA with flow vs. 0.207 ± 0.048 for scramble siRNA with flow, Figure 48D), a similar trend to the effect of blocking tysorine phosphorylation.

Actin polymerization and protrusion formation is required for 3D cell migration, and the number of protrusions per cell in 2D is an indicator for 3D cell motility of MDA-MB 231 cells (198). Exposing cells to 4hrs of 4.6μm/s flow caused a decrease in protrusion formation, but cells extended more protrusions in the upstream direction (Figure 48E-F). The mean circularity (the ratio of the square of the cell perimeter to the cell area, circularity = 1 for a circle) decreased from 7.75 ± 0.854 to 4.21 ± 0.461 with flow (Figure 4E). To determine the relative number of protrusions upstream and downstream, we divided maximum intensity projections of an actin stain into thirds by area and compared the upstream perimeter to the downstream perimeter (Figure 4F). With flow, the relative upstream perimeter increased from -0.0353 ± 0.038 to 0.146 ± 0.046, and these actin-rich upstream protrusions colocalize with cortactin (Figure 50), a marker for cell polarity and the leading edge for 3D cell migration(199). For both control and flow conditions, paxillin siRNA significantly increased the number of protrusions (circularity of 10.552 ± 8.297 for control and 9.863 for flow), and interestingly, there was no observable upstream protrusion bias for cells treated with paxillin siRNA (relative circularity of -0.0471 ± 0.036 for flow compared to 0.007 ± 0.043 for control).
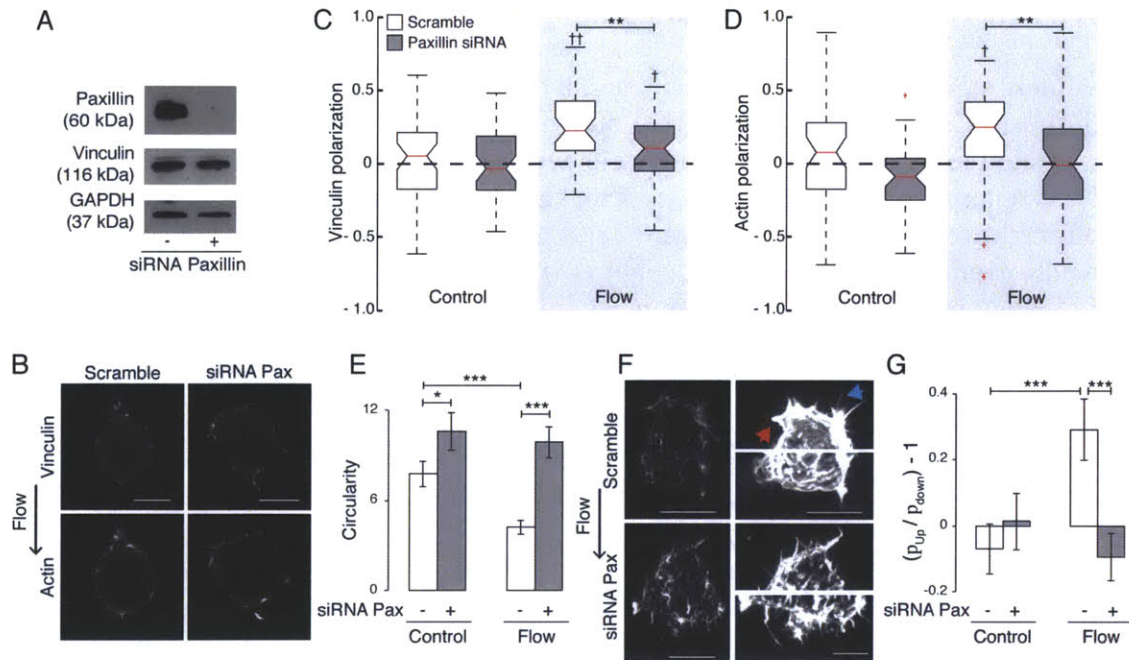
Figure 48. IF induces paxillin-dependent protrusion formation at the upstream cell membrane. A) Immunoblots showing paxillin, vinculin and GAPDH protein levels in MDA-MB-231 cells transfected with scramble control or paxillin-targeted siRNA. B) Cells treated with paxillin siRNA demonstrate isotropically distributed actin, and vinculin-containing adhesions localize both upstream and downstream. C, D) Paxillin siRNA attenuates polarization of vinculin (C) and completely blocks polarization of actin (D). E) Paxillin siRNA increases the number of protrusions for both control and flow as measured by circularity, a nondimensional measure of the square of cell perimeter normalized by cell area (=1 for a circle). F) Maximum actin intensity projections of a cell exposed to flow for 4hrs. Actin is more densely localized at the upstream membrane than on the downstream (left, scale bar 10μm). Magnified images of the upstream and downstream 1/3rd of the cell as measured by area demonstrate more protrusions at the upstream cell membrane for cells exposed to flow, including larger protrusions indicated by red arrow and slender filipodia-like protrusion indicated by blue arrow (right, scale bar 5μm). Cells treated with paxillin siRNA demonstrate more protrusions with no directional bias (left scale bar 10μm, right 5μm). G) The difference in perimeter between the upstream and downstream 1/3rd of each cell area (as depicted in (F)) demonstrates that under flow more protrusions form in the upstream direction, and paxillin siRNA attenuates the upstream protrusion bias (>45 cells from >3 devices for each condition, ***p<0.001, **p<0.01, *p<0.05, calculated from Wilcoxon rank-sum test. †p<0.05, ††p<0.01 measured vs. control).
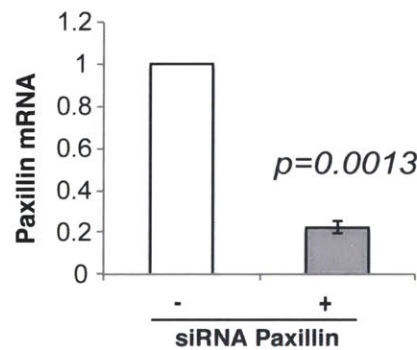
Figure 49. Graph showing mRNA level of paxillin in cells treated with control or paxillin siRNA (n=3).
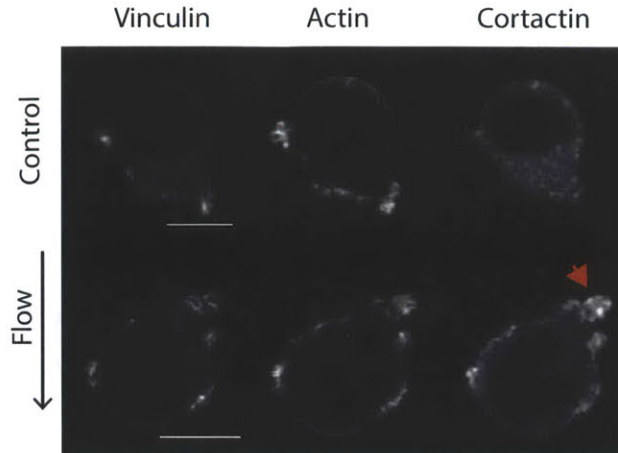
Figure 50. Cortactin localizes to protrusions in the upstream direction for cells exposed to flow (red arrow, scale bar 10µm).

4.8 IF induces paxillin-dependent rheotaxis

IF has been shown to induce rheotaxis when cells are seeded at sufficiently high density for paracrine chemokine fields to interfere with autocrine chemokine fields (Chapter 3), and cells migrating upstream have been shown to migrate with increased persistence (49). We seeded cells at a density shown to induce preferential upstream migration of MDA-MB 231 (6×10^5 cells/ml) and applied 4.6µm/s flow for 8hrs, tracking the cells by taking images every 15min. Cells preferentially migrated upstream (Figure 51A) with increased directionality (net migration distance normalized by total migration distance, Figure 52) though migration speed was unaffected by flow (Figure 52). Paxillin siRNA attenuated upstream migration (Figure 51B) and reduced flow-induced increases in directionality (Figure 52), but migration speed was unaffected by paxillin silencing (Figure 52). The use of genistein did, however, attenuate migration speed (**Figure 53**).

To further evaluate the effect of flow on the direction of cell migration, the direction of the net migration vectors for each cell in 4 separate devices (>300 tracks per condition) were plotted in polar histograms (Figure 51C). Flow induced a dramatic increase in the fraction of cells migrating upstream, while treatment of cells with paxillin siRNA reversed the directional bias, causing more cells to migrate downstream than upstream (Figure 51C). The difference between the fraction of cells migrating upstream and the fraction migrating downstream was calculated for each device, and flow caused a significant increase in the relative fraction of cells migrating upstream (from -0.088±0.079 to 0.289±0.0294 with flow, Figure 51D). Paxillin was required for the upstream migration bias, with paxillin siRNA causing a significant decrease in the relative fraction migrating upstream with flow (-0.165±0.047), and in fact, a net downstream migration bias is observed with flow and paxillin siRNA (Figure 51D).
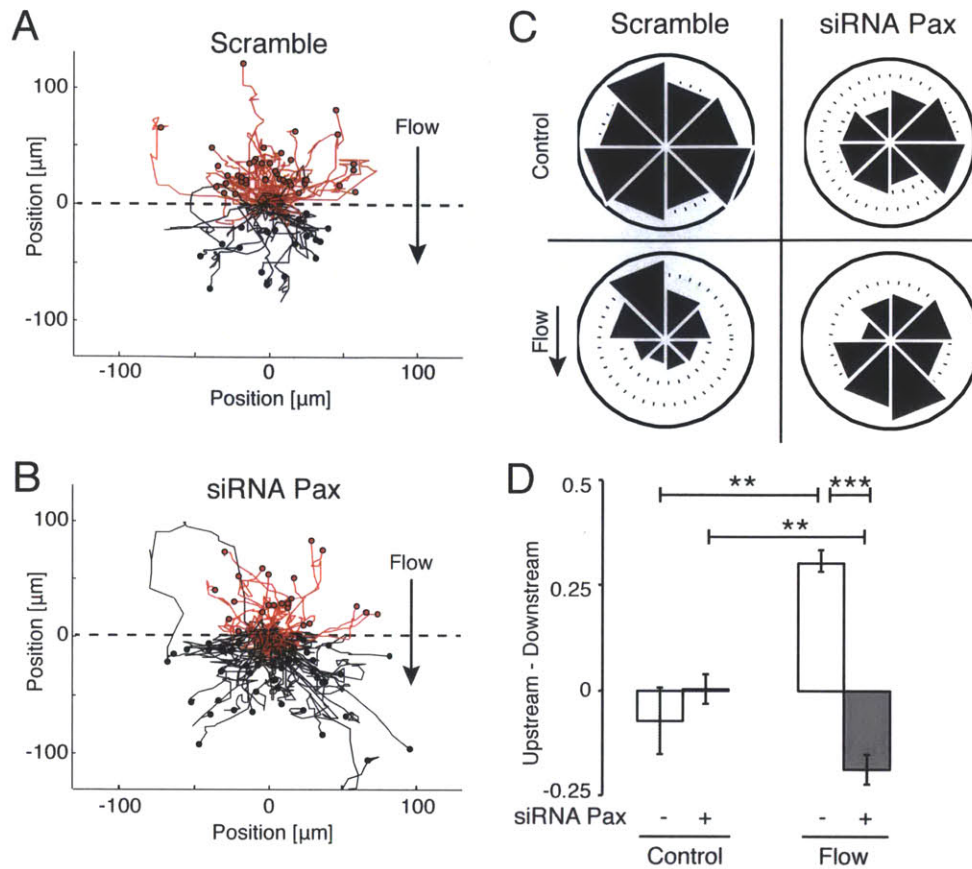
Figure 51. IF induces paxillin-dependent rheotaxis. A) Sample migration tracks demonstrate upstream migration over 8hrs when exposed to flow. Migration tracks with a net upstream displacement are colored red, and downstream tracks are black (for clarity, only tracks from cells that migrated >30μm over 8hrs are shown). B) Treatment with paxillin siRNA reduces upstream migration. C) Polar histograms of the direction of net displacement for each cell tracked over 8hrs (>300 tracks from 4 devices per condition) demonstrate flow-induced rheotaxis, which is attenuated with paxillin siRNA. D) Difference between the fraction of cells migrating upstream and downstream for each condition in C) (mean±SEM, ***p<0.001 calculated by one-way ANOVA).
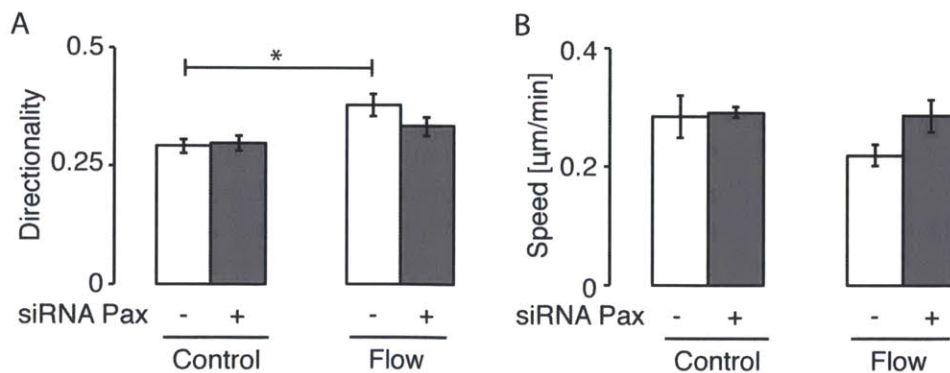
Figure 52. IF increases migration directionality but does not affect average migration speed. A) Directionality (net migration distance normalized by total migration distance) increases with flow, but when paxillin is silenced, the increase in directionality is attenuated. B) Migration speed is unaffected by flow or siRNA paxillin treatment (mean±SEM, *p<0.05 determined by one-way ANOVA for 4 devices at each condition).
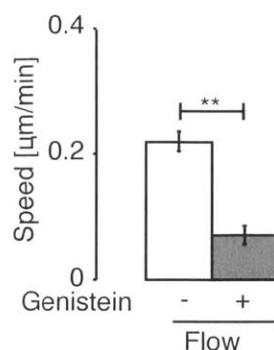
Figure 53. Genistein reduces average migration speed (mean±SEM, **p<0.01 determined by one-way ANOVA for 3 devices at each condition).

4.9 Discussion

Interstitial fluid flow induces a transcellular gradient in matrix adhesion stress inducing adhesion activation, cell polarization, and migration towards regions of maximum adhesion tension (Figure 54). This response is mediated by tension-sensitive β1 integrin complexes and results from a force balance required to maintain static equilibrium. Integrins are under maximum tension at the upstream side of the cell (Figure 6), and tension-induced FA-associated protein localization upstream leads to actin accumulation and membrane protrusion in the upstream direction, eventually leading to upstream migration. The trends for directional protrusion extension are strikingly similar to the trends for the direction of cell migration (Figure 48G & Figure 51D), consistent with the observation that protrusion formation is a marker for 3D motility of MDA-MB-231 cells(198).

Here, we provide evidence for a paxillin-dependent mechanism by which focal adhesion activation leads to protrusion formation and migration in porous media (Figure 6). Actin localization upstream requires paxillin and tyrosine kinase activity; vinculin, on the other hand, remains localized upstream, but the extent of polarization decreases when tyrosine phosphorylation is inhibited and when paxillin is silenced. These data are consistent with the observations of Pasapera *et al.*, who demonstrated that vinculin is recruited to FAs by two separate pathways (111) (Figure 54). In one, tension across β1-integrins is transmitted to talin, opening cryptic binding domains in talin and allowing vinculin to bind independent of kinase activity (88,109,110). The second pathway involves tension-mediated FAK phosphorylation at Y397. This allows for the formation of the FAK/Src signaling complex and phosphorylation of paxillin at Y31/Y118, which recruits vinculin and causes FA maturation (111).

In addition to imparting fluid stresses, IF convects released autocrine factors downstream, causing gradients of autologously secreted chemokines that have been shown to direct migration downstream in response to IF (40). Furthermore, it has been shown that these

autocrine gradients compete with IF fluid stresses, and for MDA-MB 231 cells, subpopulations that preferentially migrate upstream and downstream emerge when exposed to flow(49). It has further been shown that at high cell densities, autocrine chemokine fields overlap with fields from neighboring cells, reducing transcellular autocrine gradients and inducing preferential upstream migration. In this study, cells were seeded at a sufficiently high density (6 × 10^5 cells/ml) and flow rate to minimize contributions from autocrine gradients, leading to upstream migration. Silencing paxillin, however, caused cells preferentially to migrate downstream (Figure 51), consistent with the hypothesis that IF induces simultaneous competing upstream and downstream stimuli. The nature of the responses to these stimuli, with downstream migration arising from chemical transport and upstream migration from stress asymmetry, motivate consideration of chemo-mechanical crosstalk in studying tumor cell migration in the context of the metastatic cascade (15).

In the present experiments, 4.6 μm/s IF imparts ~1 Pa (1 pN/μm^2) average stress to the cell due to the pressure drop across the cell length. Images of collagen matrix obtained from confocal reflectance imaging, however, demonstrate that only a fraction of the cell surface is adhered to the local matrix (Figure 42). Estimating that 20% of the cell area adhered to matrix fibers (fraction of reflectance pixels at cell boundary greater than mean + S.D. reflectance intensity in Figure 42), stress at matrix adhesions is amplified to 5 pN/μm^2 stress. This level of stress falls within the range of stresses that have been shown to activate FAs on 2D surfaces (3-12 pN/μm^2 induces local actin recruitment in regions of applied stress via optical trap (200)).

The difference in normal stress across a cell of radius R scales as

$$\sigma \sim \frac{\mu \cdot U_0 \cdot R}{k}$$

where μ is the fluid viscosity, U_0 is the flow velocity, R is the cell radius and k is the permeability. Therefore, the same levels of stress asymmetry could be generated with much lower flow rates *in vivo* due to the 3 orders of magnitude lower permeability(201), suggesting that even non-pathologic IF velocities (< 1μm/s) would result in an asymmetry in matrix adhesion tension and promote directional migration.

Although these experiments were conducted on a single cell type, we expect mechanotransduction of IF stresses to be a generally relevant mechanism that influences the morphology and function of cells expressing β1 integrins embedded within tissues experiencing IF (187). For example, cells in the vicinity of an artery, vein, or lymphatic vessel are exposed to IF, and the present data suggest that the stresses imparted on these cells would influence cell morphology and migration. Indeed, basal-to-apical transendothelial flow has been shown to induce vascular sprouting angiogenesis via tension between the ECM and basal adhesions, but not when the adhesions are compressed by apical-to-basal flow (202). In these experiments, the basal cell surface adheres to collagen via β1 integrins, and basal-to-apical flow generates tension in the basal β1 integrins, in much the same way that flow generates tension at upstream matrix

adhesions in the present experiments. Furthermore, basal-to-apical flow induced phosphorylation of FAK at Y397 and localization of actin to the basal cell surface, consistent with the effect of IF on tumor cells, and sprouting was inhibited by genistein, which inhibited cell migration in the present experiments (**Figure 53**).

Cells experience asymmetric stresses *in vivo* under various conditions. For example, cell contraction induces deformation of the local matrix, and this deformation is propagated through the ECM to neighboring cells (203). For endothelial cells on 2D surfaces, traction generated by one cell can be transmitted to a neighboring cell inducing protrusion formation and migration toward the contractile cell (204). These data are consistent with our observations in 3D that local tension drives protrusion extension and migration and suggest that stress asymmetries play a role in a variety of cell processes *in vivo*. Importantly, in solid tumors, interstitial fluid flow emanates from the vasculature, and consequently, tumor cells in close proximity to blood vessels will be directed via rheotaxis toward the leaky vasculature, which is the point of maximum fluid pressure (205). Therefore, lowering IF velocity magnitude (by reducing IFP(37)) could reduce tumor cell migration toward vasculature *in vivo* and render metastatic disease more treatable.

Condition	Vinculin Localization	Actin Localization	Migration	Dir. Migration
Control	-	-	+	-
Flow	++	+	+	+
Flow+siPax	+	-	+	-
Flow+genistein	+	-	-	-
Flow+anti-beta1	-	-	-	-
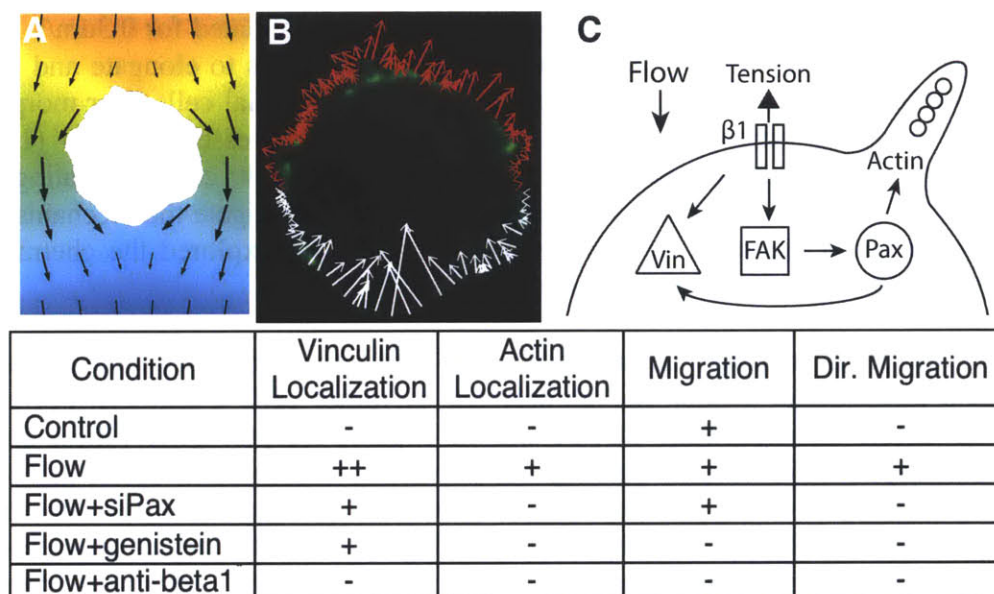
Figure 54. Mechanotransduction induces rheotaxis. A) Simulation of flow past the cell in Fig. 1C, with inlet velocity of 4.6μm/s, local fluid velocity vectors in black superimposed on heat map of pressure (red=max, blue=min). B) Local reaction forces (red=tensile, white=compressive) in cell-matrix connections required to maintain static equilibrium when exposed to flow profile in A) superimposed on an image of vinculin distribution. Vinculin localizes to regions of cell-matrix tension. C) Integrin activation by local flow-induced tension induces vinculin, FAK, paxillin, and actin localization, and subsequent protrusion extension at the upstream cell membrane. Table. Upstream localization of vinculin is maintained in the absence of paxillin or when tyrosine kinase activity is blocked, but actin localization and subsequent protrusion extension, and upstream migration require both tyrosine kinase activity and functional paxillin

Chapter 5: Conclusions and future work

5.1 Conclusions and contributions

Tumor cell migration is required for the formation of metastases, the formation of which is the leading cause of death in breast cancer patients (74). Consequently, understanding the stimuli that induce and guide cell migration and the mechanisms by which tumor cells transduce the stimuli into a migratory response is critical for developing drugs that interfere with cell migration and prevent the formation of metastases (15). As a tumor grows in mass and progresses toward a metastatic phenotype, leaky blood vessels, osmotic gradients, solid stress, and collapsed lymphatic vessels within the tumor (20) contribute to increased interstitial fluid pressure at the tumor core. The pressurized fluid is drained by lymphatic and venous vasculature in the peritumoral stroma, and thus significant pressure gradients develop at the tumor margin (21). These pressure gradients drive fluid flow that emanates from the tumor core (25). In this thesis, we explore the effects of this interstitial fluid flow on tumor cell migration.

Specifically, we take a reductionist approach to isolate the effect of IF on individual metastatic breast cancer cells (MDA-MB 231). To generate repeatable and robust IF through physiologically relevant 3D ECM, we developed a microfluidic platform, modified from previous platforms for investigating angiogenesis (162). The platform allowed for the generation of IF at physiologic velocities (validated for 0.3um/s-10um/s, and monitoring of the tumor cells in real time. IF caused cells to elongate and align to flow streamlines, consistent with the observation that endothelial cells alter morphology and align to shear stresses similar to those in capillary vessels *in vivo* (174). IF dramatically influenced the migration of tumor cells, with cells migrating along streamlines in the upstream or downstream direction. To investigate the mechanisms that lead to preferential upstream or downstream migration, we explored the chemical and mechanical stimuli imparted by flow on tumor cells.

IF alters the local transport environment, and convective transport induces Peclet-#-dependent gradients in soluble factors secreted by tumor cells (Figure 22). For isolated cells that secrete the chemokine CCL21 and the cognate receptor CCR7, these gradients can induce asymmetric receptor binding and activation, with more receptors activated on the downstream side of the cell (Figure 22), which induces chemotaxis downstream. This autologous chemotaxis, described by Shields et al. (40), drives tumor cell migration when autocrine gradients are unaffected by neighboring. However, when cell density is increased or autocrine receptors are blocked, the effect of autocrine chemokine gradients is attenuated, and cells no longer preferentially migrate downstream. In fact, the migration direction is reversed, and cells migrate upstream.

In addition to altering transport environment, IF imparts fluid stresses on cells. These stresses must be balanced by matrix adhesion tension to maintain static equilibrium, and thus flow induces asymmetric matrix adhesion stress with greater tension in adhesions on the upstream side of the cell. For MDA-MB 231 cells in collagen I, these matrix adhesions are principally comprised of tension-sensitive $\beta 1$ integrins. Therefore, FA

complexes at the upstream side of the cell are activated and this activation is propagated, through paxillin and FAK, to induce protrusion formation and eventual migration upstream (Figure 54). This upstream migration, called rheotaxis, has been observed in other cell types (184,206,207), but the data contained in this thesis are the first to suggest asymmetry in matrix adhesion stress, caused by IF drag, induces rheotaxis.

Autologous chemotaxis, mediated by chemical transport, and rheotaxis, mediated by fluid stresses, compete to direct cell migration downstream or upstream, respectively (Figure 55). At high cell density, rheotaxis dominates and cells migrate upstream, while at low cell density, autologous chemotaxis dominates and cells migrate downstream. Furthermore, these stimuli act independently: at high density, interfering with FA-signaling allows autologous chemotaxis to direct cell migration downstream, and at low density, interfering with CCR7 allows rheotaxis to direct cell migration upstream. Therefore, for each cell in a population, the two stimuli compete, and the local microenvironment (magnitude of stresses and autocrine gradients), determines which stimulus will dominate to direct cell migration (Figure 55). The premise that each stimulus competes to direct migration for each cell in a population suggests that if cells are dispersed within an ECM with some heterogeneity in the distance between each cell and the neighboring cells, some cells will migrate upstream via rheotaxis and others will migrate downstream via autologous chemotaxis, depending on the local microenvironment (see upper left cell vs. lower left cell in Figure 33A. Indeed, in recent experiments, Haessler et al. identified subpopulations of cells that migrate upstream and subpopulations that migrate downstream within a population of MDA-MB 231 cells exposed to IF.

In summary, we developed a microfluidic device to apply IF to metastatic breast cancer cells. By implementing this device, we validated CCR7 autologous chemotaxis as a mechanism that causes downstream migration in response to IF. Furthermore, we established cell density and IF speed as key parameters in determining the sensitivity of cells to autocrine gradients and their propensity to migrate via autologous chemotaxis. Finally, we identified rheotaxis as a novel mechanism for migration in response to IF. Although the mechanism underlying rheotaxis, namely FA activation and associated signaling, has been characterized previously, we are the first to demonstrate that this mechanotransduction mechanism can arise from asymmetry in matrix adhesion stress and that such stress asymmetry can be induced by IF. Interstitial flow is just one of many biochemical and biophysical stimuli in vivo that influences tumor cell migration, but its consideration is crucial for understanding and treating metastatic disease.
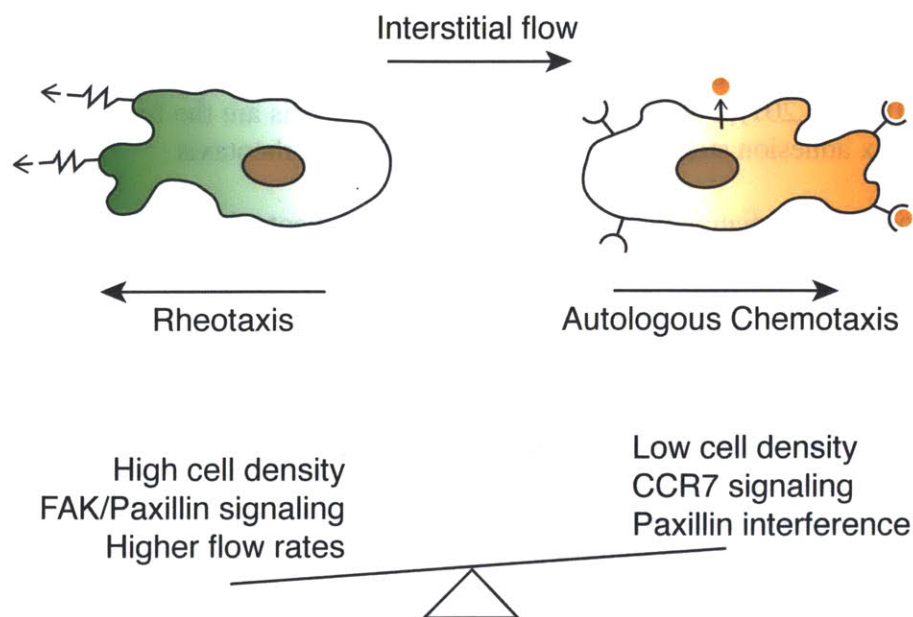
Figure 55. Rheotaxis and autologous chemotaxis compete to determine the direction of cell migration in response to IF. At high cell density, rheotaxis dominates, and cells migrate upstream, and at low cell density, autologous chemotaxis dominates and cells migrate downstream. However, at high cell density, interfering with paxillin allows autologous chemotaxis to dominate, and at low cell density, interfering with CCR7 allows rheotaxis to dominate.

5.2 Implications

The tumor microenvironment and escape radius

Interstitial flow has been studied extensively with regard to drug transport for cancer treatment (208), and *in vivo* it has been shown that interstitial fluid pressure (IFP) is correlated with cervical cancer patient survival (24) and reducing interstitial fluid pressure reduces tumor cell proliferation (37). Because interstitial fluid flows from a tumor to surrounding lymphatics or the low-pressure veins, blocking CCR7 and thus inhibiting migration in the flow direction would reduce migration from the tumor and likely reduce the probability of metastasis formation. Cell density and interstitial flow rates decrease with increasing distance from the tumor, both of which are highest at the tumor margin. Since high cell density and high flow rates both favor upstream migration, our data suggest the existence of an "escape radius" at a critical distance from the tumor surface (

Figure 56). For cells at a radial distance less than the escape radius, interstitial flow guides cells upstream, keeping cells clustered with the tumor, and inducing migration toward high-pressure tumor vasculature. These data suggest that high density cells would migrate toward high-pressure arterial vasculature rather than venous vasculature. For cells located beyond the escape radius, interstitial flow guides cells downstream, toward draining lymphatics or veins. Although further modeling and *in vivo* data are required to validate

this hypothesis, the escape radius could be a critical parameter in estimating the severity of metastatic disease and determining proper treatment.
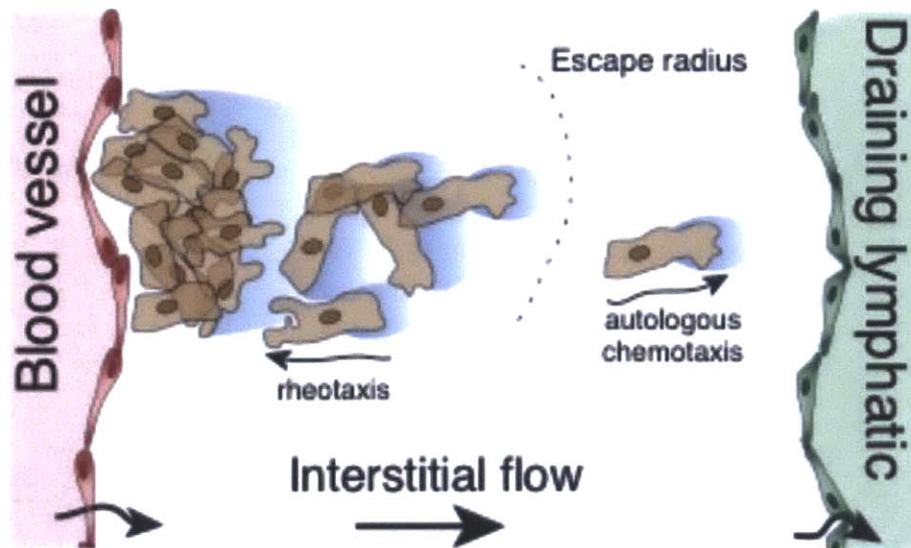
Figure 56. The competing nature of autologous chemotaxis and rheotaxis suggest the existence of an escape radius within the tumor microenvironment. High cell density and flow rates favor rheotaxis, inducing migration toward tumor-associated blood vasculature. However, low cell density and lower flow rates favor autologous chemotaxis, driving cells toward draining lymphatics.

3D durotaxis

We demonstrate that paxillin is required for directional protrusion and rheotaxis, which is consistent with the observation that paxillin is required for protrusion toward regions of maximum adhesion tension on 2D substrates (126). It is also known that phosphorylated paxillin enhances lamellipodial activity for cells on 2D substrates (209), and importantly, the FAK/paxillin/vinculin signaling axis is instrumental in durotaxis (104). Consequently, the mechanism and relevant signaling pathways responsible for rheotaxis in 3D ECM may be similar to the mechanism underlying durotaxis for cells on 2D substrates, where cells migrate in response to gradients in matrix adhesion tension that result from myosin-dependent cell contraction on substrates with a gradient in mechanical stiffness (118). Cells exert greater force against a stiff substrate than a soft one (118), so the normal stresses are higher against a stiff ECM, causing migration in the direction of the stiffer matrix. Therefore, the mechanism underlying rheotaxis and durotaxis may be the same, where stress asymmetry at matrix adhesions induces migration toward adhesions under

maximum tension (

Rheotaxis

Durotaxis

Applied Tractions   Reaction stresses

Figure 57).

Rheotaxis

Durotaxis

Applied Tractions   Reaction stresses
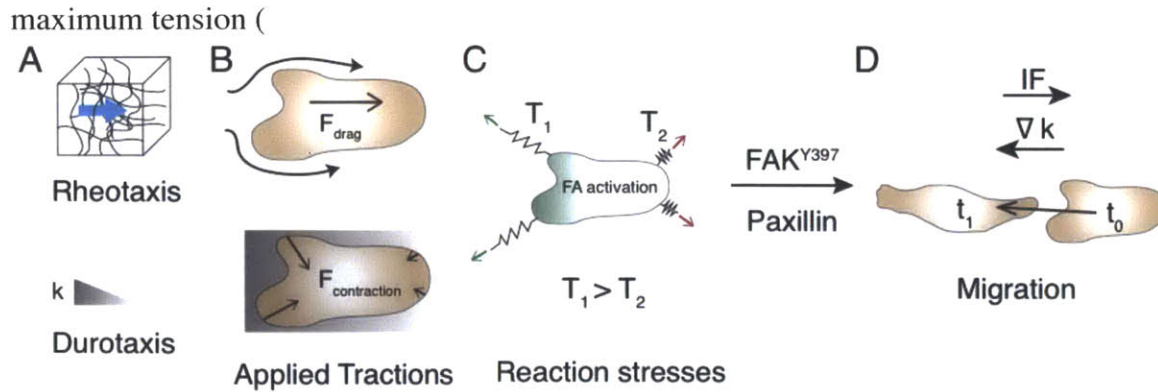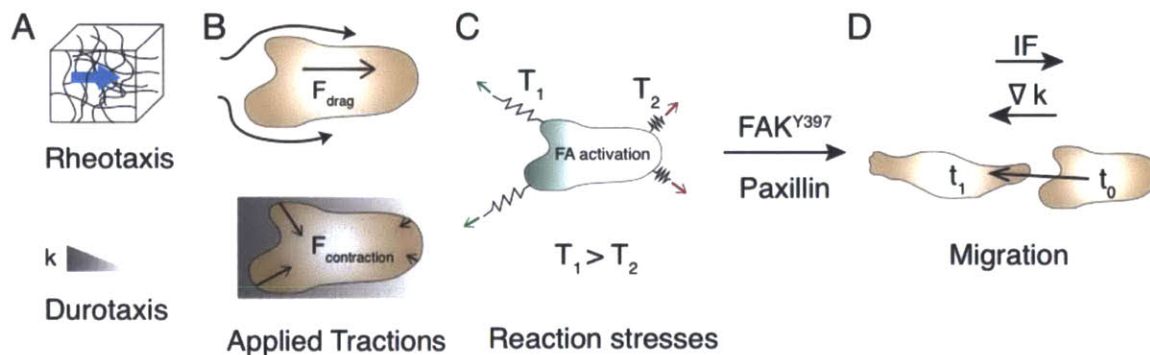
Figure 57. The role of matrix adhesion stress asymmetry suggests similar mechanisms are responsible for rheotaxis and durotaxis. A-B) IF imparts net downstream downstream drag force on cells exposed to IF, while gradients in substrate stiffness induce greater cell traction on stiffer regions of the substrate. C) The reaction stresses required to maintain static equilibrium in response to IF and the increased traction generated on stiffer substrates cause asymmetry in matrix adhesion stress. D) The gradients in matrix adhesion stress direct FAK- and paxillin-dependent rheotaxis and durotaxis.

5.3 Future research directions

EMT

Though we have discussed the effects of IF stresses in the context of tumor cell migration and rheotaxis, we expect these stresses to influence the epithelial-to-mesenchymal transition *in vivo*. The FAK/Src signaling axis is a critical regulator of EMT in solid tumors (55,210), and FAK catalytic activity was required for down regulation of E-cadherin in colon cancer cells (211). Furthermore, IF velocity magnitude (27) and interstitial fluid pressure (37) increase with solid tumor progression, and we demonstrate that these increases in pressure and fluid velocity stimulate FAK phosphorylation at Y397, which has been shown to promote Src binding to FAK and activation of the Src/FAK signaling complex (212), which subsequently drives cells toward a

mesenchymal (211), motile (213), metastatic phenotype (92), and flow has been shown to stimulate EMT in ovarian cancer (214). Therefore, IF is a critical stimulus in the metastatic cascade, and lowering IF velocity magnitude (by reducing IFP (37)) could reduce tumor cell migration *in vivo* and render metastatic disease more treatable.

Computational analysis of stress distribution

The analysis for IF stresses imparted on tumor cells is largely based from analytical solutions to Brinkman's flow past a sphere (188) and 2D simulations on geometries generated from confocal microscopy data (Figure 54). However, to better understand the full 3D stress profile, a computational simulation including a full 3D representation of the cell, matrix, and matrix adhesions must be developed. By representing the full cellular structure and associated matrix as a 3D computational domain (i.e./ finite element mesh), we could simulate fluid stresses and local chemokine gradients on a single cell. Such single-cell simulations could then be incorporated into a device-level simulation, and full experiments within microfluidic devices could be simulated to provide insight into the local mechanisms that guide cell migration and to verify that local gradients and stresses compete to determine the direction of cell migration in response to IF.

We were able to generate a full 3D mesh for cells imaged with confocal microscopy (Figure 58); however, modeling representing the matrix in a computational model presented more of a difficulty (Figure 58). Matrix fibers are of the same diameter (fractions of a micron) as the optical resolution of our confocal system, which rigorous representation of fibers in 3D. However, there are a few strategies for overcoming this limitation, including: 1) Imaging with higher magnification, high NA objective (100x). However, improved resolution comes at the cost of cytotoxicity. Live imaging, which would be required for any sort of traction force microscopy, would be very difficult due to high-power excitation. 2) Alternative strategies for reconstructing fibrous material. Rather than fitting surfaces to each collagen fiber, we assume a distribution of fiber diameters based on electron microscopy (EM) data. We then implement a fit process of 1D lines that follow collagen fibers and subsequently dilate these lines so the distribution of fiber diameters is similar to what has been measured by EM. Although method 2 is less rigorous than creating computational objects for each fiber independently, it does not require extra hardware and would vastly improve on continuum models.

Certainly much effort would be required to develop such a computational model, but there are many potential applications for such a method. For example, Representing the collagen fibers computationaly would allow videos of matrix deformation to be converted to displacement data, and by implementing the appropriate consitituive law (a nontrivial task in itself), a label-free 3D traction force microscopy method could be developed from confocal reflectance imaging. Because the *in vivo* ECM is fibrous and porous, rigorous modeling of ECM mechanics is required for fully understanding mechanotransduction and the force landscape of 3D mesenchymal migration.
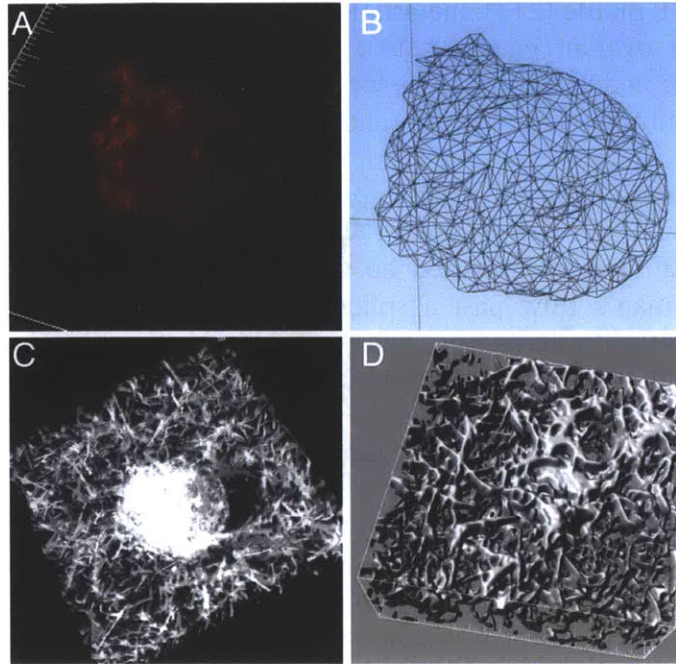
Figure 58. Approaches for representing confocal imaging data as computational FEM domains. A) 3D reconstruction of a full z-stack of images for immunofluorescence-labeled vinculin. B) Using a 3D edge detection and surface-fitting algorithm, the fluorescence images can be converted to a FEM mesh. C) Confocal reflectance image of the pericellular matrix for the cell in (A). D) Though surface-fitting algorithms recapitulate some elements of the matrix in (C), fibers are artificially dilated in z due to insufficient optical resolution, and the close proximity of fibers creates an artifact whereby the computational domain is characterized by more crosslinks among matrix fibers than the actual matrix.

References

1. Chambers AF, Groom AC, MacDonald IC. Metastasis: Dissemination and growth of cancer cells in metastatic sites. Nat Rev Cancer. 2002;2:563–72.
2. Friedl P, Hegerfeldt Y, Tusch M. Collective cell migration in morphogenesis and cancer. Int. J. Dev. Biol. 2004;48:441–9.
3. Mierke CT, Zitterbart DP, Kollmannsberger P, Raupach C, Schlötzer-Schrehardt U, Goecke TW, et al. Breakdown of the Endothelial Barrier Function in Tumor Cell Transmigration. Biophysj. Elsevier; 2008;94:2832–46.
4. Fidler IJ. The pathogenesis of cancer metastasis: the "seed and soil" hypothesis revisited. Nat. Rev. Cancer. 2003. pages 453–8.
5. Pantel K, Brakenhoff RH. Dissecting the metastatic cascade. Nat Rev Cancer. 2004;4:448–56.
6. Weigelt B, Peterse JL, van't Veer LJ. Breast cancer metastasis: markers and models. Nat Rev Cancer. 2005;5:591–602.
7. Stoecklein NH, Hosch SB, Bezler M, Stern F, Hartmann CH, Vay C, et al. Direct Genetic Analysis of Single Disseminated Cancer Cells for Prediction of Outcome and Therapy Selection in Esophageal Cancer. Cancer Cell. 2008;13:441–53.
8. Friedl P, Alexander S. Cancer Invasion and the Microenvironment: Plasticity and Reciprocity. Cell. 2011;147:992–1009.
9. Fidler IJ, Kripke ML. Metastasis Results From Preexisting Variant Cells Within a Malignant-Tumor. Science. 1977;197:893–5.
10. Weigelt B. Molecular Portraits and 70-Gene Prognosis Signature Are Preserved throughout the Metastatic Process of Breast Cancer. Cancer Research. 2005;65:9155–8.
11. Rhim AD, Mirek ET, Aiello NM, Maitra A, Bailey JM, McAllister F, et al. EMT and Dissemination Precede Pancreatic Tumor Formation. Cell. Elsevier Inc; 2012;148:349–61.
12. Paszek MJ, Zahir N, Johnson KR, Lakins JN, Rozenberg GI, Gefen A, et al. Tensional homeostasis and the malignant phenotype. Cancer Cell. 2005;8:241–54.
13. Moore SW, Roca-Cusachs P, Sheetz MP. Stretchy Proteins on Stretchy Substrates: The Important Elements of Integrin-Mediated Rigidity Sensing. Developmental Cell. 2010;19:194–206.
14. Roussos ET, Condeelis JS, Patsialou A. Chemotaxis in cancer. Nat Rev Cancer. 2011;11:573–87.
15. Polacheck WJ, Zervantonakis IK, Kamm RD. Tumor cell migration in complex microenvironments. Cell. Mol. Life Sci. 2012;70:1335–56.
16. Swartz MA, Fleury ME. Interstitial Flow and Its Effects in Soft Tissues. Annu. Rev. Biomed. Eng. 2007;9:229–56.
17. Swartz MA, Lund AW. Lymphatic and interstitial flow in the tumour microenvironment: linking mechanobiology with immunity. Nature Publishing Group; 2012;:1–10.
18. Jain RK. Transport of molecules in the tumor interstitium: a review. Cancer Metastasis Rev. [Internet]. 1987;47:3039–51. Available from: http://cancerres.aacrjournals.org/content/47/12/3039.short

19.   Boardman KC. Interstitial Flow as a Guide for Lymphangiogenesis. Circulation Research. 2003;92:801–8.

20.   Chauhan VP, Stylianopoulos T, Boucher Y, Jain RK. Delivery of Molecular and Nanoscale Medicine to Tumors: Transport Barriers and Strategies. Annu. Rev. Chem. Biomol. Eng. 2011;2:281–98.

21.   Chary SR, Jain RK. Direct Measurement of Interstitial Convection and Diffusion of Albumin in Normal and Neoplastic Tissues by Fluorescence Photobleaching. Proceedings of the National Academy of Sciences. 1989;86:5385–9.

22.   Ng CP, Swartz MA. Mechanisms of Interstitial Flow-Induced Remodeling of Fibroblast–Collagen Cultures. Ann Biomed Eng. 2006;34:446–54.

23.   Less JR, Posner MC, BOUCHER Y, Borochovitz D, Wolmark N, Jain RK. Interstitial hypertension in human breast and colorectal tumors. Cancer Research. 1992;52:6371–4.

24.   Milosevic M, Fyles A, Hedley D, Pintilie M, Levin W, Manchul L, et al. Interstitial fluid pressure predicts survival in patients with cervix cancer independent of clinical prognostic factors and tumor oxygen measurements. Cancer Research. AACR; 2001;61:6400–5.

25.   Boucher Y, Baxter LT, Jain RK. Interstitial Pressure-Gradients in Tissue-Isolated and Subcutaneous Tumors - Implications for Therapy. Cancer Research. 1990;50:4478–84.

26.   Nathanson SD, Nelson L. Interstitial fluid pressure in breast cancer, benign breast conditions, and breast parenchyma. Ann. Surg. Oncol. 1994;1:333–8.

27.   Hompland T, Ellingsen C, Ovrebo KM, Rofstad EK. Interstitial Fluid Pressure and Associated Lymph Node Metastasis Revealed in Tumors by Dynamic Contrast-Enhanced MRI. Cancer Research. 2012;72:4899–908.

28.   Curti BD, Urba WJ, Alvord WG, Janik JE, Smith JW, Madara K, et al. Interstitial Pressure of Subcutaneous Nodules in Melanoma and Lymphoma Patients - Changes During Treatment. Cancer Research. 1993;53:2204–7.

29.   Znati CA, Rosenstein M, Boucher Y, Epperly MW, Bloomer WD, Jain RK. Effect of Radiation on Interstitial Fluid Pressure and Oxygenation in a Human Tumor Xenograft. Cancer Research. 1996.

30.   Taghian AG, Abi-Raad R, Assaad SI, Casty A, Ancukiewicz M, Yeh E, et al. Paclitaxel decreases the interstitial fluid pressure and improves oxygenation in breast cancers in patients treated with neoadjuvant chemotherapy: clinical implications. J. Clin. Oncol. 2005;23:1951–61.

31.   Boucher Y, Jain RK. Microvascular pressure is the principal driving force for interstitial hypertension in solid tumors: implications for vascular collapse. Cancer Research. AACR; 1992;52:5110–4.

32.   Provenzano PP, Cuevas C, Chang AE, Goel VK, Hoff Von DD, Hingorani SR. Enzymatic Targeting of the Stroma Ablates Physical Barriers to Treatment of Pancreatic Ductal Adenocarcinoma. Cancer Cell. Elsevier Inc; 2012;21:418–29.

33.   Dafni H, Israely T, Bhujwalla ZM, Benjamin LE, Neeman M. Overexpression of vascular endothelial growth factor 165 drives peritumor interstitial convection and induces lymphatic drain: Magnetic resonance imaging, confocal microscopy, and histological tracking of triple-labeled albumin. Cancer Research. 2002;62:6731–9.

34. Baxter LT, Jain RK. Transport of fluid and macromolecules in tumors. I. Role of interstitial pressure and convection. Microvascular Research. 1989;37:77–104.

35. Jain RK, Tong RT, Munn LL. Effect of Vascular Normalization by Antiangiogenic Therapy on Interstitial Hypertension, Peritumor Edema, and Lymphatic Metastasis: Insights from a Mathematical Model. Cancer Research. 2007;67:2729–35.

36. Chang S-F, Chang CA, Lee D-Y, Leet P-L, Yeh Y-M, Yeh C-R, et al. Tumor cell cycle arrest induced by shear stress: Roles of integrins and Smad. Proceedings of the National Academy of Sciences. 2008;105:3927–32.

37. Hofmann M, Guschel M, Bernd A, Bereiter-Hahn J, Kaufmann R, Tandi C, et al. Lowering of Tumor Interstitial Fluid Pressure Reduces Tumor Cell Proliferation in a Xenograft Tumor Model. NEO. 2006;8:89–95.

38. Dadiani M, Kalchenko V, Yosepovich A, Margalit R, Hassid Y, Degani H, et al. Real-time imaging of lymphogenic metastasis in orthotopic human breast cancer. Cancer Research. 2006;66:8037–41.

39. Shieh AC, Swartz MA. Regulation of tumor invasion by interstitial fluid flow. Phys. Biol. 2011;8:015012.

40. Shields JD, Fleury ME, Yong C, Tomei AA, Randolph GJ, Swartz MA. Autologous Chemotaxis as a Mechanism of Tumor Cell Homing to Lymphatics via Interstitial Flow and Autocrine CCR7 Signaling. Cancer Cell. 2007;11:526–38.

41. Fleury ME, Boardman KC, Swartz MA. Autologous Morphogen Gradients by Subtle Interstitial Flow and Matrix Interactions. Biophysical Journal. 2006;91:113–21.

42. Shi ZD, Ji XY, Qazi H, Tarbell JM. Interstitial flow promotes vascular fibroblast, myofibroblast, and smooth muscle cell motility in 3-D collagen I via upregulation of MMP-1. AJP: Heart and Circulatory Physiology. 2009;297:H1225–34.

43. Shieh AC, Rozansky HA, Hinz B, Swartz MA. Tumor Cell Invasion Is Promoted by Interstitial Flow-Induced Matrix Priming by Stromal Fibroblasts. Cancer Research. 2011;71:790–800.

44. Pedersen JA, Lichter S, Swartz MA. Cells in 3D matrices under interstitial flow: Effects of extracellular matrix alignment on cell shear stress and drag forces. J Biomech [Internet]. Elsevier; 2010;43:900–5. Available from: http://linkinghub.elsevier.com/retrieve/pii/S0021929009006435

45. Pedersen JA, Boschetti F, Swartz MA. Effects of extracellular fiber architecture on cell membrane shear stress in a 3D fibrous matrix. J Biomech. 2007;40:1484–92.

46. Shi Z-D, Wang H, Tarbell JM. Heparan Sulfate Proteoglycans Mediate Interstitial Flow Mechanotransduction Regulating MMP-13 Expression and Cell Motility via FAK-ERK in 3D Collagen. Feghali-Bostwick C, editor. PLoS ONE. 2011;6:e15956.

47. Beauvais DM, Rapraeger AC. Syndecan-1-mediated cell spreading requires signaling by $\alpha v \beta 3$ integrins in human breast carcinoma cells. Experimental Cell Research. 2003;286:219–32.

48. Polacheck WJ, Charest JL, Kamm RD. Interstitial flow influences direction of

tumor cell migration through competing mechanisms. Proc. Natl. Acad. Sci. U.S.A. 2011;108:11115–20.

49. Haessler U, Teo JCM, Foretay D, Renaud P, Swartz MA. Migration dynamics of breast cancer cells in a tunable 3D interstitial flow chamber. Integr. Biol. 2012;4:401.

50. Qazi H, Shi Z-D, Tarbell JM. Fluid Shear Stress Regulates the Invasive Potential of Glioma Cells via Modulation of Migratory Activity and Matrix Metalloproteinase Expression. Deb S, editor. PLoS ONE. 2011;6:e20348.

51. Shieh AC. Biomechanical Forces Shape the Tumor Microenvironment. Ann Biomed Eng. 2011;39:1379–89.

52. Thompson EW, TORRI J, SABOL M, Sommers CL, BYERS S, VALVERIUS EM, et al. Oncogene-Induced Basement-Membrane Invasiveness in Human Mammary Epithelial-Cells. Clin Exp Metastasis. 1994;12:181–94.

53. Sommers CL, Heckford SE, Skerker JM, Worland P, Torri JA, Thompson EW, et al. Loss of Epithelial Markers and Acquisition of Vimentin Expression in Adriamycin-Resistant and Vinblastine-Resistant Human Breast-Cancer Cell-Lines. Cancer Research. 1992;52:5190–7.

54. Nieman MT, Prudoff RS, Johnson KR, Wheelock MJ. N-cadherin promotes motility in human breast cancer cells regardless of their E-cadherin expression. J. Cell Biol. 1999;147:631–43.

55. Thiery JP. Epithelial–mesenchymal transitions in tumour progression. Nat Rev Cancer. 2002;2:442–54.

56. Lauffenburger DA, Horwitz AF. Cell migration: A physically integrated molecular process. Cell. 1996;84:359–69.

57. Ridley AJ, Schwartz MA, Burridge K, Firtel RA, Ginsberg MH, Borisy G, et al. Cell migration: Integrating signals from front to back. Science. 2003;302:1704–9.

58. Weaver AM. Invadopodia: Specialized Cell Structures for Cancer Invasion. Clin Exp Metastasis. 2006;23:97–105.

59. Tranquillo RT, Lauffenburger DA, Zigmond SH. A Stochastic-Model for Leukocyte Random Motility and Chemotaxis Based on Receptor-Binding Fluctuations. J. Cell Biol. 1988;106:303–9.

60. Petrie RJ, Doyle AD, Yamada KM. Random versus directionally persistent cell migration. Nat Rev Mol Cell Biol [Internet]. 2009;10:538–49. Available from: http://www.nature.com/nrm/journal/vaop/ncurrent/full/nrm2729.html

61. Niggemann B, Drell TL IV, Joseph J, Weidt C, Lang K, Zaenker KS, et al. Tumor cell locomotion: differential dynamics of spontaneous and induced migration in a 3D collagen matrix. Experimental Cell Research. 2004;298:178–87.

62. Wang F, Weaver VM, Petersen OW, Larabell CA, Dedhar S, Briand P, et al. Reciprocal interactions between beta1-integrin and epidermal growth factor receptor in three-dimensional basement membrane breast cultures: a different perspective in epithelial biology. Proceedings of the National Academy of Sciences. 1998;95:14821–6.

63. Mouneimne G, DesMarais V, Sidani M, Scemes E, Wang W, Song X, et al. Spatial and Temporal Control of Cofilin Activity Is Required for Directional

Sensing during Chemotaxis. Current Biology. 2006;16:2193–205.

64. Ben-Baruch A. The multifaceted roles of chemokines in malignancy. Cancer Metastasis Rev. 2006;25:357–71.

65. Wang S-J, Saadi W, Lin F, Minh-Canh Nguyen C, Li Jeon N. Differential effects of EGF gradient profiles on MDA-MB-231 breast cancer cell chemotaxis. Experimental Cell Research. 2004;300:180–9.

66. Weiner OD. Regulation of cell polarity during eukaryotic chemotaxis: the chemotactic compass. Current Opinion in Cell Biology. 2002;14:196–202.

67. Van Haastert PJM, Devreotes PN. Chemotaxis: signalling the way forward. Nature Publishing Group. 2004;5:626–34.

68. Chan AY, Raft S, Bailly M, Wyckoff JB, Segall JE, Condeelis JS. EGF stimulates an increase in actin nucleation and filament number at the leading edge of the lamellipod in mammary adenocarcinoma cells. Journal of Cell Science. 1998;111 (Pt 2):199–211.

69. Ghosh K, Pan Z, Guan E, Ge S, Liu Y, Nakamura T, et al. Cell adaptation to a physiologically relevant ECM mimic with different viscoelastic properties. Biomaterials. 2007;28:671–9.

70. Mouneimne G. Phospholipase C and cofilin are required for carcinoma cell directionality in response to EGF stimulation. The Journal of Cell Biology. 2004;166:697–708.

71. Hill K, Welti S, Yu JH, Murray JT, Yip SC, Condeelis JS, et al. Specific requirement for the p85-p110 alpha phosphatidylinositol 3-kinase during epidermal growth factor-stimulated actin nucleation in breast cancer cells. Journal of Biological Chemistry. 2000;275:3741–4.

72. Schoeberl B, Eichler-Jonsson C, Gilles ED, Müller G. Computational modeling of the dynamics of the MAP kinase cascade activated by surface and internalized EGF receptors. Nat. Biotechnol. Nature Publishing Group; 2002;20:370–5.

73. Li H, Ung CY, Ma XH, Li BW, Low BC, Cao ZW, et al. Simulation of crosstalk between small GTPase RhoA and EGFR-ERK signaling pathway via MEKK1. Bioinformatics. 2009;25:358–64.

74. Muller A, Homey B, Soto H, Ge NF, Catron D, Buchanan ME, et al. Involvement of chemokine receptors in breast cancer metastasis. Nature. 2001;410:50–6.

75. Yoshida R, Imai T, Hieshima K, Kusuda J, Baba M, Kitaura M, et al. Molecular Cloning of a Novel Human CC Chemokine EBI1-ligand Chemokine That Is a Specific Functional Ligand for EBI1, CCR7. Journal of Biological .... 1997.

76. Riol-Blanco L, Sánchez-Sánchez N, Torres A, Tejedor A, Narumiya S, Corbí AL, et al. The chemokine receptor CCR7 activates in dendritic cells two signaling modules that independently regulate chemotaxis and migratory speed. J. Immunol. 2005;174:4070–80.

77. Cabioglu N. CCR7 and CXCR4 as Novel Biomarkers Predicting Axillary Lymph Node Metastasis in T1 Breast Cancer. Clinical Cancer Research. 2005;11:5686–93.

78. Liu Y, Ji R, Li J, Gu Q, Zhao X, Sun T, et al. Correlation effect of EGFR and CXCR4 and CCR7 chemokine receptors in predicting breast cancer metastasis and prognosis. J Exp Clin Cancer Res. 2010;29:16.

79. Shields JD, Kourtis IC, Tomei AA, Roberts JM, Swartz MA. Induction of lymphoidlike stroma and immune escape by tumors that express the chemokine CCL21. Science. 2010;328:749–52.

80. Kim S-J, Shin J-Y, Lee K-D, Bae Y-K, Sung KW, Nam SJ, et al. MicroRNA let-7a suppresses breast cancer cell migration and invasion through downregulation of C-C chemokine receptor type 7. Breast Cancer Res. 2012;14:R14.

81. Pan M-R, Hou M-F, Chang H-C, Hung W-C. Cyclooxygenase-2 up-regulates CCR7 via EP2/EP4 receptor signaling pathways to enhance lymphatic invasion of breast cancer cells. Journal of Biological Chemistry. 2008;283:11155–63.

82. Lin S-S, Sun L, Zhang Y-K, Zhao R-P, Liang W-L, Yuan S-T, et al. Topotecan inhibits cancer cell migration by down-regulation of chemokine CC motif receptor 7 and matrix metalloproteinases. Acta Pharmacol Sin. 2009;30:628–36.

83. Kochetkova M, Kumar S, McColl SR. Chemokine receptors CXCR4 and CCR7 promote metastasis by preventing anoikis in cancer cells. Nature Publishing Group; 2009;16:664–73.

84. Danen EHJ. Integrin Signaling as a Cancer Drug Target. ISRN Cell Biology. 2013;2013:1–14.

85. Hao H, Naomoto Y, Bao X, Watanabe N, Sakurama K, Noma K, et al. Focal adhesion kinase as potential target for cancer therapy (Review). Oncol. Rep. 2009;22:973–9.

86. Cox D, Brennan M, Moran N. Integrins as therapeutic targets: lessons and opportunities. Nat Rev Drug Discov. 2010;9:804–20.

87. Hynes RO. Integrins: bidirectional, allosteric signaling machines. Cell. Elsevier; 2002;110:673–87.

88. Miyamoto S, Teramoto H, Coso OA, Gutkind JS, Burbelo PD, Akiyama SK, et al. Integrin function: molecular hierarchies of cytoskeletal and signaling molecules. The Journal of Cell Biology. Rockefeller Univ Press; 1995;131:791–805.

89. Kanchanawong P, Shtengel G, Pasapera AM, Ramko EB, Davidson MW, Hess HF, et al. Nanoscale architecture of integrin-based cell adhesions. Nature. Nature Publishing Group; 2010;468:580–4.

90. Galbraith CG. The relationship between force and focal complex development. The Journal of Cell Biology. 2002;159:695–705.

91. Romer LH. Focal Adhesions: Paradigm for a Signaling Nexus. Circulation Research. 2006;98:606–16.

92. Schlaepfer DD, Mitra SK. Multiple connections link FAK to cell motility and invasion. Current Opinion in Genetics & Development. 2004;14:92–101.

93. Cary LA, Klinghoffer RA, Sachsenmaier C, Cooper JA. Src Catalytic but Not Scaffolding Function Is Needed for Integrin-Regulated Tyrosine Phosphorylation, Cell Migration, and Cell Spreading. Molecular and Cellular Biology. 2002;22:2427–40.

94. Thomas SM, Brugge JS. Cellular functions regulated by Src family kinases. Annu. Rev. Cell Dev. Biol. 1997;13:513–609.

95. Frame MC. Src in cancer: deregulation and consequences for cell behaviour. Biochim. Biophys. Acta. 2002;1602:114–30.

96. Kim LC, Song L, Haura EB. Src kinases as therapeutic targets for cancer. Nature

Reviews Clinical Oncology. Nature Publishing Group; 2009;6:587–95.

97. Chen Y, Pasapera AM, Koretsky AP, Waterman CM. Orientation-specific responses to sustained uniaxial stretching in focal adhesion growth and turnover. Proc. Natl. Acad. Sci. U.S.A. 2013.

98. Mack PJ. Force-induced focal adhesion translocation: effects of force amplitude and frequency. AJP: Cell Physiology. 2004;287:C954–62.

99. Riveline D, Zamir E, Balaban NQ, Schwarz US, Ishizaki T, Narumiya S, et al. Focal contacts as mechanosensors: Externally applied local mechanical force induces growth of focal contacts by an mDia1-dependent and ROCK-independent mechanism. The Journal of Cell Biology. 2001;153:1175–85.

100. Shi J, Wang S, Zhao E, Shi L, Xu X, Fang M. Paxillin expression levels are correlated with clinical stage and metastasis in salivary adenoid cystic carcinoma. J. Oral Pathol. Med. 2010;39:548–51.

101. Salgia R, Li JL, Ewaniuk DS, Wang YB, Sattler M, al E. Expression of the focal adhesion protein paxillin in lung cancer and its relation to cell motility. Oncogene. 1999.

102. Brock AL, Ingber DE. Control of the direction of lamellipodia extension through changes in the balance between Rac and Rho activities. MCB-TECH SCIENCE PRESS. 2005.

103. Sero JE, German AE, Mammoto A, Ingber DE. Paxillin controls directional cell motility in response to physical cues. celladhesion. 2012;6:502–8.

104. Plotnikov SV, Pasapera AM, Sabass B, Waterman CM. Force Fluctuations within Focal Adhesions Mediate ECM-Rigidity Sensing to Guide Directed Cell Migration. Cell. Elsevier Inc; 2012;151:1513–27.

105. Choquet D, Felsenfeld DP, Sheetz MP. Extracellular matrix rigidity causes strengthening of integrin-cytoskeleton linkages. Cell. 1997;88:39–48.

106. Wang N, Butler JP, Ingber DE. Mechanotransduction Across the Cell-Surface and Through the Cytoskeleton. Science. 1993;260:1124–7.

107. Goldmann WH, Auernheimer V, Thievessen I, Fabry B. Vinculin, cell mechanics and tumour cell invasion. Cell Biol. Int. Wiley Online Library; 2013.

108. Goldmann WH, Ingber DE. Intact Vinculin Protein Is Required for Control of Cell Shape, Cell Mechanics, and rac-Dependent Lamellipodia Formation. Biochemical and biophysical research .... 2002.

109. del Rio A, Perez-Jimenez R, Liu R, Roca-Cusachs P, Fernandez JM, Sheetz MP. Stretching Single Talin Rod Molecules Activates Vinculin Binding. Science. 2009;323:638–41.

110. Grashoff C, Hoffman BD, Brenner MD, Zhou R, Parsons M, Yang MT, et al. Measuring mechanical tension across vinculin reveals regulation of focal adhesion dynamics. Nature. Nature Publishing Group; 2010;466:263–6.

111. Pasapera AM, Schneider IC, Rericha E, Schlaepfer DD, Waterman CM. Myosin II activity regulates vinculin recruitment to focal adhesions through FAK-mediated paxillin phosphorylation. The Journal of Cell Biology. 2010;188:877–90.

112. Wang S, Watanabe T, Matsuzawa K, Katsumi A, Kakeno M, Matsui T, et al. Tiam1 interaction with the PAR complex promotes talin-mediated Rac1 activation during polarized cell migration. The Journal of Cell Biology.

2012;199:331–45.

113. Wang HB, Dembo M, Hanks SK, Wang YL. Focal adhesion kinase is involved in mechanosensing during fibroblast migration. Proceedings of the National Academy of Sciences. 2001;98:11295–300.

114. Delanoe-Ayari H, Kurdi Al R, Vallade M, Gulino-Debrac D, Riveline D. Membrane and acto-myosin tension promote clustering of adhesion proteins. Proceedings of the National Academy of Sciences. 2004;101:2229–34.

115. Allioux-Guérin M, Icard-Arcizet D, Durieux C, Hénon S, Gallet F, Mevel J-C, et al. Spatiotemporal Analysis of Cell Response to a Rigidity Gradient: A Quantitative Study Using Multiple Optical Tweezers. Biophysj. Biophysical Society; 2009;96:238–47.

116. Dumbauld DW, Lee TT, Singh A, Scrimgeour J, Gersbach CA, Zamir EA, et al. How vinculin regulates force transmission. Proc. Natl. Acad. Sci. U.S.A. 2013.

117. Balaban NQ, Schwarz US, Riveline D, Goichberg P, Tzur G, Sabanay I, et al. Force and focal adhesion assembly: a close relationship studied using elastic micropatterned substrates. Nat. Cell Biol. Nature Publishing Group; 2001;3:466–72.

118. Lo C-M, Wang H-B, Dembo M, Wang Y-L. Cell Movement Is Guided by the Rigidity of the Substrate. Biophysj. Elsevier; 2000;79:144–52.

119. Tzima E, del Pozo MA, Shattil SJ, Chien S, Schwartz MA. Activation of integrins in endothelial cells by fluid shear stress mediates Rho-dependent cytoskeletal alignment. EMBO J. 2001;20:4639–47.

120. Li S, Kim M, Hu YL, Jalali S, Schlaepfer DD, Hunter T, et al. Fluid shear stress activation of focal adhesion kinase - Linking to mitogen-activated protein kinases. Journal of Biological Chemistry. 1997;272:30455–62.

121. Shyy JY, Chien S. Role of integrins in cellular responses to mechanical stress and adhesion. Current Opinion in Cell Biology. Elsevier; 1997;9:707–13.

122. Parker KK, Brock AL, Brangwynne CP, Mannix RJ, Wang N, Ostuni E, et al. Directional control of lamellipodia extension by constraining cell shape and orienting cell tractional forces. FASEB J. 2002;16:–1204.

123. Xia N, Thodeti CK, Hunt TP, Xu Q, Ho M, al E. Directional control of cell motility through focal adhesion positioning and spatial control of Rac activation. The FASEB Journal. 2008.

124. Saez A, Ghibaudo M, Buguin A, Silberzan P, Ladoux B. Rigidity-driven growth and migration of epithelial cells on microstructured anisotropic substrates. Proceedings of the National Academy of Sciences. 2007;104:8281–6.

125. Mierke CT, Kollmannsberger P, Zitterbart DP, Diez G, Koch TM, Marg S, et al. Vinculin Facilitates Cell Invasion into Three-dimensional Collagen Matrices. Journal of Biological Chemistry. 2010;285:13121–30.

126. Sero JE, Thodeti CK, Mammoto A, Bakal C, Thomas S, Ingber DE. Paxillin Mediates Sensing of Physical Cues and Regulates Directional Cell Motility by Controlling Lamellipodia Positioning. Parsons M, editor. PLoS ONE. 2011;6:e28303.

127. Mitra SK, Hanson DA, Schlaepfer DD. Focal adhesion kinase: in command and control of cell motility. Nat Rev Mol Cell Biol. 2005;6:56–68.

128. Plotnikov SV, Waterman CM. Guiding cell migration by tugging. Current

Opinion in Cell Biology. 2013.

129. Discher D, Dong C, Fredberg JJ, Guilak F, Ingber D, Janmey P, et al. Biomechanics: Cell Research and Applications for the Next Decade. Ann Biomed Eng. 2009;37:847–59.

130. Discher DE. Tissue Cells Feel and Respond to the Stiffness of Their Substrate. Science. 2005;310:1139–43.

131. Butcher DT, Alliston T, Weaver VM. A tense situation: forcing tumour progression. Nat Rev Cancer. 2009;9:108–22.

132. Polacheck WJ, Li R, Uzel SGM, Kamm RD. Microfluidic platforms for mechanobiology. Lab Chip. 2013;13:2252.

133. Fraley SI, Feng Y, Krishnamurthy R, Kim D-H, Celedon A, Longmore GD, et al. A distinctive role for focal adhesion proteins in three-dimensional cell motility. Nature Publishing Group. 2010;12:598–604.

134. Harunaga JS, Yamada KM. Cell-matrix adhesions in 3D. Matrix Biology. 2011;30:363–8.

135. Cukierman E. Taking Cell-Matrix Adhesions to the Third Dimension. Science. 2001;294:1708–12.

136. Pedersen JA, Swartz MA. Mechanobiology in the Third Dimension. Ann Biomed Eng. 2005;33:1469–90.

137. Boghaert E, Gleghorn JP, Lee K, Gjorevski N, Radisky DC, Nelson CM. Host epithelial geometry regulates breast cancer cell invasiveness. Proceedings of the National Academy of Sciences. National Acad Sciences; 2012;109:19632–7.

138. Pathak A, Kumar S. Biophysical regulation of tumor cell invasion: moving beyond matrix stiffness. Integr. Biol. 2011;3:267.

139. Levental KR, Yu H, Kass L, Lakins JN, Egeblad M, Erler JT, et al. Matrix Crosslinking Forces Tumor Progression by Enhancing Integrin Signaling. Cell. 2009;139:891–906.

140. Maskarinec SA, Franck C, Tirrell DA, Ravichandran G. Quantifying cellular traction forces in three dimensions. Proc. Natl. Acad. Sci. U.S.A. 2009;106:22108–13.

141. Legant WR, Choi CK, Miller JS, Shao L, Gao L, Betzig E, et al. Multidimensional traction force microscopy reveals out-of-plane rotational moments about focal adhesions. Proceedings of the National Academy of Sciences. National Acad Sciences; 2013;110:881–6.

142. Legant WR, Miller JS, Blakely BL, Cohen DM, Genin GM, Chen CS. Measurement of mechanical tractions exerted by cells in three-dimensional matrices. Nat Meth. 2010;7:969–71.

143. Hadjipanayi E, Mudera V, Brown RA. Guiding cell migration in 3D: A collagen matrix with graded directional stiffness. Cell Motil. Cytoskeleton. 2009;66:121–8.

144. Griffith LG, Swartz MA. Capturing complex 3D tissue physiology in vitro. Nature Publishing Group. 2006;7:211–24.

145. Huh D, Hamilton GA, Ingber DE. From 3D cell culture to organs-on-chips. Trends in Cell Biology. Elsevier Ltd; 2011;21:745–54.

146. Desgrosellier JS, Cheresh DA. biological implications andtherapeutic opportunities. Nat Rev Cancer. Nature Publishing Group; 2010;10:9–22.

147. Schultze A, Fiedler W. Clinical importance and potential use of small molecule inhibitors of focal adhesion kinase. Anticancer Agents Med Chem. 2011;11:593–9.

148. Deakin NO, Turner CE. Distinct roles for paxillin and Hic-5 in regulating breast cancer cell morphology, invasion, and metastasis. Molecular Biology of the Cell. 2011;22:327–41.

149. Fernández J, Geiger B, Salomon D, al E. Overexpression of vinculin suppresses cell motility in BALB/c 3T3 cells. Cell motility and the .... 1992.

150. Fernández J, Geiger B, Salomon D, al E. Suppression of tumorigenicity in transformed cells after transfection with vinculin cDNA. The Journal of cell .... 1992.

151. Fernández J, Geiger B, Salomon D, al E. Suppression of vinculin expression by antisense transfection confers changes in cell morphology, motility, and anchorage-dependent growth of 3T3 cells. The Journal of cell .... 1993.

152. Khalili P, Arakelian A, Chen G, Plunkett ML, Beck I, al E. A non–RGD-based integrin binding peptide (ATN-161) blocks breast cancer growth and metastasis in vivo. Molecular cancer .... 2006.

153. Dhani NC, Burris HA III, Siu LL. Final report of phase I clinical, pharmacokinetic (PK), pharmacodynamic (PD) study of PF-00562271 targeting focal adhesion kinase (FAK) in patients (pts) with solid tumors. -- Dhani et al. 28 (15): 3028 -- ASCO Meeting Abstracts. J. Clin. Oncol. 2010.

154. Vickerman V, Blundo J, Chung S, Kamm R. Design, fabrication and implementation of a novel multi-parameter control microfluidic platform for three-dimensional cell culture and real-time imaging. Lab Chip. 2008;8:1468.

155. Keenan TM, Hsu C-H, Folch A. Microfluidic "jets" for generating steady-state gradients of soluble molecules on open surfaces. Appl. Phys. Lett. 2006;89:114103.

156. Shin Y, Han S, Jeon JS, Yamamoto K, Zervantonakis IK, Sudo R, et al. Microfluidic assay for simultaneous culture of multiple cell types on surfaces or within hydrogels. Nat Protoc. 2012;7:1247–59.

157. Keenan TM, Folch A. Biomolecular gradients in cell culture systems. Lab Chip. 2007;8:34.

158. Zervantonakis IK, Kothapalli CR, Chung S, Sudo R, Kamm RD. Microfluidic devices for studying heterotypic cell-cell interactions and tissue specimen cultures under controlled microenvironments. Biomicrofluidics. 2011;5:013406.

159. Zervantonakis IK, Hughes-Alford SK, Charest JL, Condeelis JS, Gertler FB, Kamm RD. Three-dimensional microfluidic model for tumor cell intravasation and endothelial barrier function. Proc. Natl. Acad. Sci. U.S.A. 2012;109:13515–20.

160. Jeon JS, Zervantonakis IK, Chung S, Kamm RD, Charest JL. In Vitro Model of Tumor Cell Extravasation. PLoS ONE. Public Library of Science; 2013;8:e56910.

161. Han S, Yan J-J, Shin Y, Jeon JJ, Won J, Eun Jeong H, et al. A versatile assay for monitoring in vivo-like transendothelial migration of neutrophils. Lab Chip. 2012;12:3861.

162. Farahat WA, Wood LB, Zervantonakis IK, Schor A, Ong S, Neal D, et al.

Ensemble Analysis of Angiogenic Growth in Three-Dimensional Microfluidic Cell Cultures. Egles C, editor. PLoS ONE. 2012;7:e37333.

163.   Shin Y, Jeon JS, Han S, Jung G-S, Shin S, Lee S-H, et al. In vitro 3D collective sprouting angiogenesis under orchestrated ANG-1 and VEGF gradients. Lab Chip. The Royal Society of Chemistry; 2011;11:2175–81.

164.   Soon L. A discourse on cancer cell chemotaxis: Where to from here? TBMB. 2007;59:60–7.

165.   Boyden S. The chemotactic effect of mixtures of antibody and antigen on polymorphonuclear leucocytes. J. Exp. Med. 1962;115:453–66.

166.   Philipsborn von AC, Lang S, Loeschinger J, Bernard A, David C, Lehnert D, et al. Growth cone navigation in substrate-bound ephrin gradients. Development. 2006;133:2487–95.

167.   Simpson KJ, Selfors LM, Bui J, Reynolds A, Leake D, Khvorova A, et al. Identification of genes that regulate epithelial cell migration using an siRNA screening approach. Nature. 2008;10:1027–38.

168.   Sabeh F, Shimizu-Hirota R, Weiss SJ. Protease-dependent versus -independent cancer cell invasion programs: three-dimensional amoeboid movement revisited. The Journal of Cell Biology. 2009.

169.   Chung S, Sudo R, Mack PJ, Wan C-R, Vickerman V, Kamm RD. Cell migration into scaffolds under co-culture conditions in a microfluidic platform. Lab Chip. 2009;9:269.

170.   Song JW, Munn LL. Fluid forces control endothelial sprouting. Proc. Natl. Acad. Sci. U.S.A. [Internet]. 2011;108:15342–7. Available from: http://eutils.ncbi.nlm.nih.gov/entrez/eutils/elink.fcgi?dbfrom=pubmed&id=21876168&retmode=ref&cmd=prlinks

171.   Xia Y, Whitesides GM. Soft lithography. Annual review of materials science. Annual Reviews 4139 El Camino Way, PO Box 10139, Palo Alto, CA 94303-0139, USA; 1998;28:153–84.

172.   Bakal C, Aach J, Church G, Perrimon N. Quantitative Morphological Signatures Define Local Signaling Networks Regulating Cell Morphology. Science. 2007.

173.   Brinkman HC. A Calculation of the Viscous Force Exerted by a Flowing Fluid on a Dense Swarm of Particles. Applied Scientific Research Section a-Mechanics Heat Chemical Engineering Mathematical Methods. 1947;1:27–34.

174.   Levesque MJ, Nerem RM. The Elongation and Orientation of Cultured Endothelial Cells in Response to Shear Stress. J Biomech Eng. 1985;107:341.

175.   Ware MF, Wells A, Lauffenburger DA. Epidermal growth factor alters fibroblast migration speed and directional persistence reciprocally and in a matrix-dependent manner. Journal of Cell Science. 1998;111:2423–32.

176.   Jalali S, del Pozo MA, Chen K-D, Miao H, Li Y-S, Schwartz MA, et al. Integrin-mediated mechanotransduction requires its dynamic interaction with specific extracellular matrix (ECM) ligands. Proceedings of the National Academy of Sciences. National Acad Sciences; 2001;98:1042–6.

177.   Li S, Huang NF, Hsu S. Mechanotransduction in endothelial cell migration. J. Cell. Biochem. 2005;96:1110–26.

178.   Thomas JW, Ellis B, Boerner RJ, Knight WB, White GC, Schaller MD. SH2- and SH3-mediated Interactions between Focal Adhesion Kinase and Src*.

Journal of Biological Chemistry. ASBMB; 2011;273:577–83.

179. Eide BL, Turck CW, Escobedo JA. Identification of Tyr-397 as the primary site of tyrosine phosphorylation and pp60src association in the focal adhesion kinase, pp125FAK. Molecular and Cellular Biology. 1995;15:2819–27.

180. Schaller MD, Hildebrand JD, Shannon JD, Fox JW, Vines RR, Parsons JT. Autophosphorylation of the focal adhesion kinase, pp125FAK, directs SH2-dependent binding of pp60src. Molecular and Cellular Biology. 1994;14:1680–8.

181. Fincham VJ, Frame MC. The catalytic activity of Src is dispensable for translocation to focal adhesions but controls the turnover of these structures during cell motility. EMBO J. 1998;17:81–92.

182. Bardi G, Niggli V, Loetscher P. Rho kinase is required for CCR7-mediated polarization and chemotaxis of T lymphocytes. FEBS Letters. 2003;542:79–83.

183. Li S, Butler P, Wang YX, Hu YL, Han DC, Usami S, et al. The role of the dynamics of focal adhesion kinase in the mechanotaxis of endothelial cells. Proceedings of the National Academy of Sciences. 2002;99:3546–51.

184. Lin X, Helmke BP. Cell Structure Controls Endothelial Cell Migration under Fluid Shear Stress. Cel. Mol. Bioeng. 2009;2:231–43.

185. Tarbell JM, Weinbaum S, Kamm RD. Cellular Fluid Mechanics and Mechanotransduction. Ann Biomed Eng. 2005;33:1719–23.

186. Galbraith CG, Skalak R, Chien S. Shear stress induces spatial reorganization of the endothelial cell cytoskeleton. Cell Motil. Cytoskeleton. 1998;40:317–30.

187. Rutkowski JM, Swartz MA. A driving force for change: interstitial flow as a morphoregulator. Trends in Cell Biology. 2007;17:44–50.

188. Ganapathy R. Creeping flow past a solid sphere in a porous medium. Zeitschrift Fur Angewandte Mathematik Und Mechanik. 1997;77:871–5.

189. Zamir E, Katz BZ, Aota S, Yamada KM, Geiger B, Kam Z. Molecular diversity of cell-matrix adhesions. Journal of Cell Science. 1999;112 (Pt 11):1655–69.

190. Otsu N. A threshold selection method from gray-level histograms. Automatica. 1975;11:23–7.

191. Brightman AO, Rajwa BP, Sturgis JE, McCallister ME, Robinson JP, Voytik-Harbin SL. Time-lapse confocal reflection microscopy of collagen fibrillogenesis and extracellular matrix assembly in vitro. Biopolymers. 2000;54:222–34.

192. Cross VL, Zheng Y, Choi NW, Verbridge SS. Dense type I collagen matrices that support cellular remodeling and microfabrication for studies of tumor angiogenesis and vasculogenesis in vitro. Biomaterials. 2010.

193. Chan KT, Cortesio CL, Huttenlocher A. FAK alters invadopodia and focal adhesion composition and dynamics to regulate breast cancer invasion. The Journal of Cell Biology. 2009;185:357–70.

194. Grisaru-Granovsky S, Salah Z, Maoz M, Pruss D, Beller U, Bar-Shavit R. Differential expression ofProtease activated receptor 1 (Par1) and pY397FAK in benign and malignant human ovarian tissue samples. Int. J. Cancer. 2004;113:372–8.

195. Choi CK, Vicente-Manzanares M, Zareno J, Whitmore LA, Mogilner A, Horowitz AR. Actin and α-actinin orchestrate the assembly and maturation of nascent adhesions in a myosin II motor-independent manner. Nature cell .... 2008.

196.   Yeon JH, Ryu HR, Chung M, Hu QP, Jeon NL. In vitro formation and characterization of a perfusable three-dimensional tubular capillary network in microfluidic devices. Lab Chip. 2012;12:2815.

197.   Ahmed N, Riley C, Rice G, Quinn M. Role of Integrin Receptors for Fibronectin, Collagen and Laminin in the Regulation of Ovarian Carcinoma Functions in Response to a Matrix Microenvironment. Clin Exp Metastasis. 2005;22:391–402.

198.   Meyer AS, Hughes-Alford SK, Kay JE, Castillo A, Wells A, Gertler FB, et al. 2D protrusion but not motility predicts growth factor-induced cancer cell migration in 3D collagen. The Journal of Cell Biology. 2012;197:721–9.

199.   Petrie RJ, Gavara N, Chadwick RS, Yamada KM. Nonpolarized signaling reveals two distinct modes of 3D cell migration. The Journal of Cell Biology. 2012;197:439–55.

200.   Icard-Arcizet D, Cardoso O, Richert A, Hénon S. Cell Stiffening in Response to External Stress is Correlated to Actin Recruitment. Biophysj. Elsevier; 2008;94:2906–13.

201.   Netti PA, Berk DA, Swartz MA, Grodzinsky AJ, Jain RK. Role of extracellular matrix assembly in interstitial transport in solid tumors. Cancer Research. 2000;60:2497–503.

202.   Vickerman V, Kamm RD. Mechanism of a flow-gated angiogenesis switch: early signaling events at cell–matrix and cell–cell junctions. Integr. Biol. 2012;4:863.

203.   Montaño I, Schiestl C, Schneider J, Pontiggia L, Luginbühl J, Biedermann T, et al. Formation of human capillaries in vitro: the engineering of prevascularized matrices. Tissue Engineering Part A. 2010;16:269–82.

204.   Reinhart-King CA, Dembo M, Hammer DA. Cell-Cell Mechanical Communication through Compliant Substrates. Biophysical Journal. 2008;95:6044–51.

205.   Y Boucher HSBWGRH4RKJ. Interstitial fluid pressure in intracranial tumours in patients and in rodents. British Journal of Cancer. Nature Publishing Group; 1997;75:829.

206.   Walton A. Flow Orientation as a Possible Explanation of 'Wave-Motion' and 'Rheotaxis' of Spermatozoa. Journal of Experimental Biology [Internet]. 1952;:1–12. Available from: http://jeb.biologists.org/content/29/4/520.full.pdf#page=1&view=FitH

207.   Lin X, Helmke BP. Micropatterned Structural Control Suppresses Mechanotaxis of Endothelial Cells. Biophysj. Elsevier; 2008;95:3066–78.

208.   Heldin C-H, Rubin K, Pietras K, Östman A. High interstitial fluid pressure — an obstacle in cancer therapy. Nat Rev Cancer [Internet]. 2004;4:806–13. Available from: http://www.nature.com/nrc/journal/v4/n10/abs/nrc1456.html

209.   Zaidel-Bar R, Milo R, Kam Z, Geiger B. A paxillin tyrosine phosphorylation switch regulates the assembly and form of cell-matrix adhesions. Journal of Cell Science. 2006;120:137–48.

210.   Avizienyte E, Frame MC. Src and FAK signalling controls adhesion fate and the epithelial-to-mesenchymal transition. Current Opinion in Cell Biology. 2005;17:542–7.

211.   Avizienyte E, Wyke AW, Jones RJ, McLean GW, Westhoff MA, Brunton VG, et al. Src-induced de-regulation of E-cadherin in colon cancer cells requires integrin

signalling. Nat. Cell Biol. 2002.

212. McLean GW, Carragher NO, Avizienyte E, Evans J, Brunton VG, Frame MC. The role of focal-adhesion kinase in cancer—a new therapeutic opportunity. Nat Rev Cancer. Nature Publishing Group; 2005;5:505–15.

213. Hsia DA. Differential regulation of cell motility and invasion by FAK. The Journal of Cell Biology. 2003;160:753–67.

214. Rizvi I, Gurkan UA, Tasoglu S, Alagic N, Celli JP, Mensah LB, et al. Flow induces epithelial-mesenchymal transition, cellular heterogeneity and biomarker modulation in 3D ovarian cancer nodules. Proceedings of the National Academy of Sciences. National Acad Sciences; 2013;110:E1974–83.

Appendix A – Cell seeding protocol*

<u>Material</u>
[Software]
1. cells in flasks
2. media (for preparing cell suspension and for filling device channels)
3. trypsin
4. 1x PBS without calcium or magnesium
5. Collagen gel solution (substitute PBS for DMEM*)

[Hardware]
1. collagen-coated flasks (if further plating is desired)
2. 15ml falcon tube
3. 1.5ml centrifuge tube

<u>Procedure</u>
1. Have 200ul of 10X DMEM Collagen gel ready^ (9>pH>7.4).
2. Prepare cell suspension at desired concentration (will be diluted 1/10 times, 20ul cell suspension in 200ul collagen gel)
3. Place cell suspension on ice for chilling for 5 minutes (required for avoiding pre-polymerization of collagen gel suspension)
4. Add 20ul of pre-chilled cell suspension (make sure that cell pellet was broken-single cell suspension required) to the collagen gel and pipette for 30sec (4-5times and gently stir, using a larger pipette tip will reduce shear stress and increase viability). When sucking up cells-in-gel suspension make sure to place the pipette tip in the middle of the 1.5ml eppendorf tube in order to collect a well-mixed cells-in-gel suspension (avoid sucking up solution from the bottom of the eppendorf tube as it will result in a lower cell seeding density, and mix until cells are distributed uniformly).
5. Cells in Collagen gel solution is ready to be microinjected or filled in gel filling ports. Inject/Fill in the devices and place in the humidified chamber to allow polymerization at 37C. (Don't have the humidified chamber sit in the hood for more than 5minutes)
6. Add media to device channels after polymerization. Add media carefully (use long 200ul pipette tips) to avoid bubbles in the channels. Aspirating bubbles from channels can result in separation of coverslip from device.

<u>Notes.</u>
1. Use DMEM preferentially for obtaining cell viability in gel suspension. 10X PBS solutions may also work.
2. MDA231Cells are not viable in pH 7.0, Have tested pH>7.4-9
3. Make sure to aspirate all supernatant, as trypsin may result in a sparser, weak gel
4. Return filled devices to incubator quickly. Leaving filled devices in the hood (even if they're in humidity boxes) while filling others can result in lower cell viability.

5. Don't leave devices in the incubator to polymerize for longer than necessary. The gel will dry out if the channels aren't filled with media, and this will increase cell death.

If only passing cells, after step 7, simply transfer 1ml (for T25) and 3ml (for T75) to a new collagen-coated flask. Add 4ml (for T25) and 12ml (for T75) of fresh media. Place new flask in the incubator. Change media every other day.

- If cells do not detach after waiting for 2-5 minutes, then wash with PBS and add trypsin again. This may occur when the cells have become overconfluent (YZ, 11/12/07)

Potential problems

1. Fibrils bundle up resulting in a nonhomogeneous gel

Microinjection device   3 Channel gel filling (DMEM-based gels)

Possible reasons:
- o Prepolymerization of collagen gel:
  - while adding cell suspension (if using warm medium)
  - while preparing collagen gel and mixing (due to local pH variation)

Precautions:
- o Be sure to add cell/gel solution quickly. If the solution is added slowly, it can prepolymerize in the pipette tip. This can cause bundles of fibers like those in Figure 2 above.
- o This is a particular problem for microinjection as the large surface area of the metal needle can cause the gel solution to reach room temperature rapidly. One solution is to use 2 needles when microinjecting. Keep one needle on ice while using the other to microinject, and switch neeldles for the next device. Also, be sure to rinse the needles with COLD water between injections.

2. Low cell viability and black speckles appear in the collagen gel
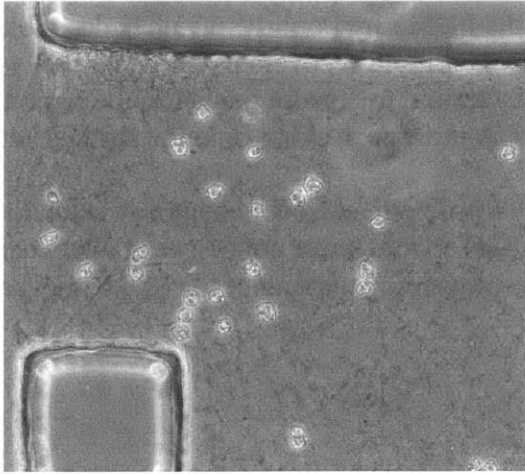
Resuidual salt from PDL coating can lead to cell death

Possible Causes:
  o After PDL coating devices, they must be rinsed with water (NOT PBS) and dried in the oven for ~36hrs. If the devices are not well rinsed, residual salts from the PDL coating will result in very low viability, and black speckles in the collagen gel

3. Inhomogeneous distribution of cells in devices (# of cells in each device varies)

Possible causes:
  o Collagen gel and cell suspension mixed poorly
    ▪ When adding cells to gel be sure to mix until cells are homogenous
  o Cells settled during device filling
    ▪ Be sure to periodically mix the collagen gel and cell suspension so cells do not accumulate at the bottom of the eppendorf tube

4. Leaking of media between PDMS and coverslip
Possible causes:
  o The PDMS was incorrectly plasma treated, or recovered hydrophobicity after plasma treatment.
  o The devices were not handled carefully during seeding.
  o The coverslip or PDMS surface were not properly cleaned (even tiny dust particles can lead to separation of the coverslip)
  o Gel solution was not carefully added and wetted the surface between the PDMS and coverslip
Comments:
  o There is an optimal time to wait after plasma treatment, and this time is characteristic to each device. For example, the thin channel microinjection

device should be seeded 1hr after plasma treatment. However, the biopsy device should be seeded 1.5-2hrs after plasma treatment.

- o Plasma treatment renders the PDMS hydrophilic which is desirable for coverslip fusion. However, the PDMS recovers its hydrophobicity with time, and hydrophobicity is desired to contain the gel in the region of interest during seeding which prevents leaking onto the surface between the PDMS and coverslip.
- o Consequently, if leaking is a problem, consider changing incubation time after plasma treatment in order to maximize bond-strength between the PDMS and coverslip while preventing wetting of the PDMS-coverslip interface.

Appendix B – Tracking microparticles for verifying IF field

Governing equations:
Brinkman's equation provides a fluid momentum balance for flow through a porous medium of hydraulic conductivity K:

$$\mu\nabla^2\underline{v} - \frac{1}{K}\underline{v} - \nabla P = 0 \qquad [1]$$

In the limit of small pore size or large length scale, where $L >> \sqrt{\mu K}$, [1] reduces to Darcy's law:

$$\underline{v} = -K\nabla P \qquad [2]$$

Method:

1) Determine appropriate microsphere size and concentration. Iteration is often required for both size and concentration of the microspheres. The nominal diameter of the microspheres must be smaller than the pore size of the gel to allow the beads to flow through the gel, and the concentration must be small enough to allow tracking of individual beads. For 2mg/ml collagen gel polymerized at pH 8.9, 200nm diameter beads at 1×10^4 beads/ml is optimal.

2) Attach fluid reservoirs to media ports of device. To assume steady pressure gradient, ensure that the cross-sectional area of the reservoirs is much larger than the cross-sectional area of the gel-region of the device.

3) Dilute the microspheres to the appropriate concentration and add the suspension to the upstream and downstream reservoirs. Measure the relative difference in fluid head height between the upstream and downstream reservoirs to determine the pressure gradient across the gel.

4) Acquire time-lapse images of the microspheres traveling through the gel at a known pressure gradient.

5) Use particle-tracking software (ie/ Imaris), to track the microspheres in the acquired timelapse image sequence.

6) Compare individual particle tracks and measure the velocity variance to determine gel heterogeneity.

7) If the variance of individual tracks is small and the length scales are large compared to the pore size of the gel, average the velocity vectors and use [2] to determine the hydraulic conductivity.

8) If the length scales are small, use FEM software to solve [1] for the geometry of the hydrogel being measured, and compare individual measured microsphere velocity vectors to those predicted by the FEM model.

Appendix C – MDA-MB 231 Passage Protocol

<u>Purpose:</u>

Transfer subpopulation of cells from a confluent flask (parent culture) to a new culture flask (daughter culture) to maintain healthy cell phenotype. Note that each passage artificially selects subpopulations of cells, and certain cell types (such as endothelial cells) will lose their characteristic phenotype at high passage numbers; therefore, it is important to keep track of the passage number.

<u>Materials:</u>

1. New culture flask (typically T25 flasks are used)
      1 flask per daughter culture
2. 15mL falcon tube
      1 tube per parent culture
3. Cold cell culture media
      10mL per parent culture
4. Warm PBS
      5mL per parent culture
5. Warm trypsin
      1mL per parent culture
6. Warm media
      5mL per daughter culture (if using T25 flasks for daughter culture)

<u>Procedure:</u>

1. Incubate PBS, trypsin, and media to 37°C
2. Aspirate media from parent culture using Pasteur pipette and vacuum tube
3. Wash parent culture with warm PBS
4. Aspirate PBS with Pasteur pipette
5. Add 1mL of warm trypsin to parent culture
6. Transfer parent culture flask with trypsin to incubator
7. Incubate trypsin and cells for 2min
8. Check that cells have been successfully lifted from flask surface
      If cells are still adhered, gently tap the flask to dislodge cells
9. Add 1mL of cold media to trypsinized cells
10.   Transfer 2mL (trypsin + cells + cold media) to falcon tube
      If counting cells: transfer 20μL to 20μL trypan blue
11.   Add 8mL cold media to falcon tube to bring total volume to 10mL
12.   Centrifuge for 5min at 1.2e3 RPM
13.   Aspirate supernatant with Pasteur pipette
14.   Re-suspend cell pellet in 1mL of warm media

15.   Transfer 200µL of cell/media suspension to daughter flask

16.   Add 5mL of warm media to each daughter flask

17.   Aspirate remaining cell/media suspension from falcon tube before disposal

Appendix D - MMP Inhibition with Aprotinin

Sources:

1. (Davis et al. JCS 2000) - Endothelial cells
2. (Ntayi et al. Exp. Cell. Res. 2001) - Melanoma invasion in 3D collagen I
3. (O'Cearbhaill et al. Ann. Biomed. Eng. 2010) - Source for concentration ranges in medium
4. (Yeon et al. Lab Chip 20012) - Source for mixing aprotinin in collagen gel

Reagents

1. Aprotinin - Sigma: A11532.
2. Standard collagen I gel reagents:
   a. NaOH
   b. DI water
   c. 10x DMEM
   d. Rat tail collagen in acetic acid

Protocol

1. Dilute aprotinin to 2 U/ml directly in 10x DMEM2. Prepare gel by standard protocol with aprotinin DMEM ie/
   a. 20μL 10x DMEM w/ 2 U/mL aprotinin
   b. 10.5μL 0.5 N NaOH
   c. 58μL DI-water
   d. 111μL 3.60 mg/ml collagen I
2. After collagen gel polymerization, add medium with 10 U/ml aprotinin
3. Continue to culture with 10 U/ml aprotinin

Appendix E – Blocking Integrins

Product: anti-integrin beta 1 antibody [P5D2] ab24693 - Abcam

Sources:
Ahmed et al. Clinical & Experimental Metastasis 2005

Preliminary titration experiment:

24-well plate with 5 concentrations (0,1,2,5,10ug/ml). 5ug/ml interfered with cell adhesion to glass coated with type 1 collagen (Fig. 1), and 10ug/ml results were similar to 5ug/ml.
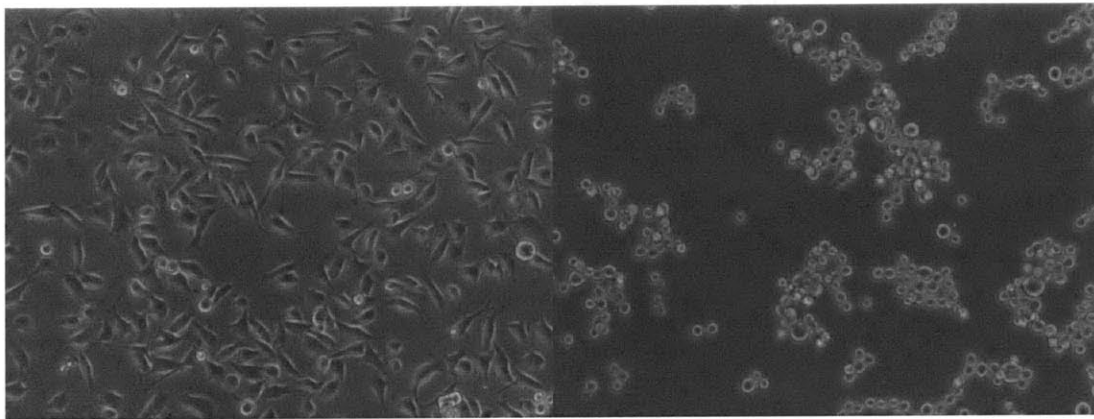

Fig. 1 MDA-231 plated on collagen type 1 coated glass for titrating beta1-integrin blocking antibody. A) Cells 90min after plating with 0ug/ml ab2693. B) Cells 90min after plating with 5mg/ml ab2693. Note: 10ug/ml shows no improvement over 5ug/ml & cells adhere and spread with 5mg/ml over 24hrs if media is not replenished every 6hrs.

Protocol 1:
- Advantage: requires less reagent, many experiments per stock antibody
- Disadvantage: does not completely block cell-matrix interactions. although cells spread much less than control, there is some matrix interaction as evidenced by vinculin, beta-1 colocalization at matrix connections

1. Resuspend stock ab2693 and aliquot into 100µl at 100µg/ml
2. For experiment, dilute aliquot in growth medium to final concentration of 5µg/ml
3. Prepare cell-gel solution following standard protocol (see 2WJP16A)

4. After collagen gel polymerization, add culture medium with 5μg/ml blocking antibody

Notes:
- To verify anti-beta1 blocking, fix cells with 4% PFA, and incubate 2hrs with goat anti-mouse secondary antibody (ab2693 is ms mAb).
- Because blocking medium is added after polymerization, cells have a chance to form matrix adhesions initially
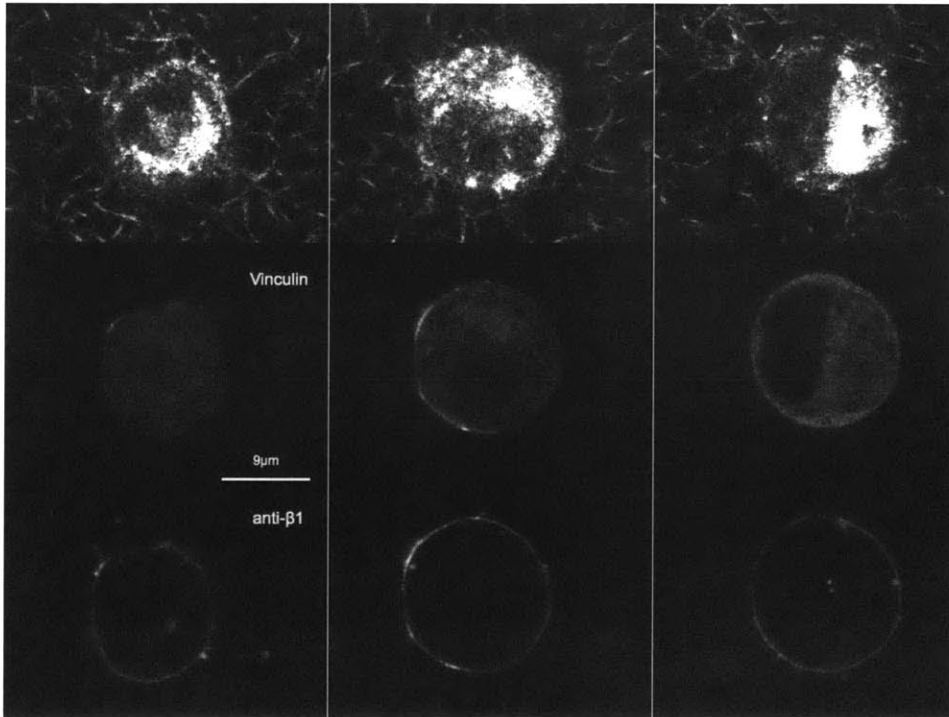

Figure 2. Reflectance, vinculin, and anti-beta1 after 24hrs following protocol 1. Note colocalization of beta1 and vinculin in fig 1A & 1B. Also note small protrusions visible in the anti-beta1 channel.

Protocol 2:
- Advantages: Totally blocks matrix adhesions. Cells remain perfectly spherical. Effects
- Disadvantages: Intense reagent use. Only 3-4 expts (defined as sessions of cell seeding) per vial

1. Resuspend stock ab2693 at 50μg/ml
   a. Note: This solution will be used to resuspend cells after centrifugation prior to mixing with collagen during cell seeding. Therefore aliquot the 50μg/ml as appropriate (on 6WJP14, 500μl aliquots were prepared so that

3e6 cells could be resuspended at 6e6 cells/ml to be diluted 10x in collagen gel yielding 6e5 cells/ml in 5µg/ml containing gel).

2. Aliquot and freeze in appropriate volumes, leaving at least 50µg for creating blocking medium
3. Remaining 50µg or more should be aliquoted according to protocol 1 for making 5µg/ml blocking antibody in growth medium.
4. Lift, count, and centrifuge cells following standard protocol (2WJP16A)
5. Resuspend cell pellet at 6e6 cells/ml in 50µg/ml anti-beta1 blocking antibody medium (from step 1)
6. Prepare 200µl collagen gel solution
7. Dilute 20µl of cell/medium solution from step 3 (6e6 cells/ml in 50µg/ml) in 200µl collagen gel solution for a cell/gell suspension containing 5µg/ml blocking antibody
8. Inject gel and allow to polymerize for 20min
9. Hydrate gel with 5µg/ml blocking antibody growth medium solution

Notes:
- Effects compared v. protocol 1 are marginal. Sample vinculin image provided in Fig. 3. Vinculin remains totally isotropic